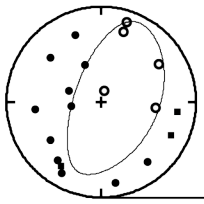

Foulger Consulting

1025 Paradise Way
Palo Alto, CA 94306-2637, USA
Tel: 650/493-2553
g.r.foulger@durham.ac.uk
http://www.dur.ac.uk/g.r.foulger/

March 31st, 2008

FINAL REPORT

AWARD NO. DE-FG36-06GO16058

RECIPIENT: FOULGER CONSULTING

CHARACTERIZATION OF EGS FRACTURE NETWORK LIFECYCLES

PI: GILLIAN R. FOULGER

CONSORTIUM/TEAM MEMBERS: BRUCE R. JULIAN, FRANCIS C. MONASTERO, KEITH RICHARDS-DINGER, PETER ROSE

Authorized distribution limitation notices: None

1 Executive summary

Geothermal energy is relatively clean, and is an important non-hydrocarbon source of energy. It can potentially reduce our dependence on fossil fuels and contribute to reduction in carbon emissions. High-temperature geothermal areas can be used for electricity generation if they contain permeable reservoirs of hot water or steam that can be extracted. The biggest challenge to achieving the full potential of the nation's resources of this kind is maintaining and creating the fracture networks required for the circulation, heating, and extraction of hot fluids. The fundamental objective of the present research was to understand how fracture networks are created in hydraulic borehole injection experiments, and how they subsequently evolve.

When high-pressure fluids are injected into boreholes in geothermal areas, they flow into hot rock at depth inducing thermal cracking and activating critically stressed pre-existing faults. This causes earthquake activity which, if monitored, can provide information on the locations of the cracks formed, their time-development and the type of cracking underway, *e.g.*, whether shear movement on faults occurred or whether cracks opened up. Ultimately it may be possible to monitor the critical earthquake parameters in near-real-time so the information can be used to guide the hydraulic injection while it is in progress, *e.g.*, how to adjust factors such as injectate pressure, volume and temperature.

In order to achieve this, it is necessary to mature analysis techniques and software that were, at the start of this project, in an embryonic developmental state. Task 1 of the present project was to develop state-of-the-art techniques and software for calculating highly accurate earthquake locations, earthquake source mechanisms (moment tensors) and temporal changes in reservoir structure. Task 2 was to apply the new techniques to hydrofracturing (Enhanced Geothermal Systems, or "EGS") experiments performed at the Coso geothermal field, in order to enhance productivity there. Task 3 was to interpret the results jointly with other geological information in order to provide a consistent physical model.

All of the original goals of the project have been achieved. An existing program for calculating accurate relative earthquake locations has been enhanced by a technique to improve the accuracy of earthquake arrival-time measurements using waveform cross-correlation. Error analysis has been added to pre-existing moment tensor software. New seismic tomography software has been written to calculate changes in structure that could be due, for example, to reservoir depletion. Data processing procedures have been streamlined and web tools developed for rapid dissemination of the results, *e.g.*, to on-site operations staff.

Application of the new analysis tools to the Coso geothermal field has demonstrated the effective use of the techniques and provided important case histories to guide the style of future applications. Changes in reservoir structure with time are imaged throughout the upper 3 km, identifying the areas where large volumes of fluid are being extracted. EGS hydrofracturing experiments in two wells stimulated a nearby fault to the south that ruptured from south to north. The position of this fault could be precisely mapped and its existence was confirmed by surface mapping and data from a borehole televiewer log. No earthquakes occurred far north of the

injection wells, suggesting that the wells lie near the northern boundary of the region of critically stressed faults. Minor en-echelon faults were also activated. Significant across-strike fluid flow occurred. The faults activated had significant crack-opening components, indicating that the hydraulic fracturing created open cavities at depth. The fluid injection changed the local stress field orientation and thus the mode of failure was different from the normal background. Initial indications are that the injections modulated stress release, seismicity and natural fracture system evolution for periods of up to months.

The research demonstrated full technical effectiveness and economic feasability of seismic monitoring of EGS injections using earthquakes as the sources. It is critical that high-quality data are available for the most useful results to be obtainable. The biggest challenge to the subject at present is to install earthquake monitoring networks of sufficient quality to deliver data that can take full advantage of the new techniques developed by this project. An industrial standard operating approach is proposed in this report. When adopted, it will potentially contribute significantly to developing fully the nations geothermal energy potential by assisting in creating the fracture networks necessary for geothermal resources to be extracted from the ground.

2 Comparison of actual accomplishments with goals and objectives of the project

The goals and objectives of the proposal were to:

a) develop state-of-the-art seismological techniques to study EGS-related fracture-network formation and evolution with extreme accuracy;
b) characterize earthquakes accompanying fracture formation before, during and after EGS stimulation experiments at the Coso geothermal area, CA, and;
c) develop a seismic characterization of the life-cycle of EGS-stimulated fracture networks.

It was planned to accomplish these objectives using the following methods:

a) Enhance currently existing state-of-the-art seismic techniques, including software to determine:

    i. relative earthquake locations with sufficiently high resolution to image individual fracture planes;
    ii. accurate three-dimensional reservoir structure, and changes in structure associated with reservoir evolution, and;
    iii. full moment tensor errors. Moment tensors provide information on opening and closure of fracture planes and cast light on fluid flow into and out of fractures.

b) Apply the new software to EGS-related earthquakes from the Coso geothermal area, where several experiments had been conducted and were planned.

c) Integrate the results with other geophysical and operational data to provide a holistic interpretation and final model of seismic characterization of EGS-fracture-network evolution.

All these goals have been achieved as planned via the following work modules:

Task 1: Software development

- *Subtask 1.1 High-resolution Earthquake Hypocenters*: The program **hypocc** was enhanced by the addition of waveform cross-correlation via the new program **toonpics**, for improved relative arrival-time measurement accuracy.
- *Subtask 1.2 Three- and Four-Dimensional Crustal Structure*: A new seismic tomography technique was developed to invert multiple epochs of earthquake arrival-time data to be inverted simultaneously to calculate changes in structure over time. The new program, **dtomo**, enables rigorous accounting of the error budget so statistically supported confidences can be assigned to the results.

- *Subtask 1.3 Earthquake Mechanisms*: Error assessment was added to existing moment tensor software.

Task 2: Application of the new techniques to the Coso geothermal area

- *Subtask 2.1 High-resolution Earthquake Hypocenters*: The enhanced high-resolution location program suite, **toonpics** + **hypocc**, was applied to seismic data collected prior to, during, and following the EGS stimulation experiments in wells 34A-9 in August 2004 and 34-9RD2 in March 2005, and to data collected in January 2007, prior to an experiment planned in well 46A-19RD. That EGS stimulation experiment was postponed and is currently planned for 2009.
- *Subtask 2.2 Three- and Four-Dimensional Crustal Structure*: Three-dimensional seismic models for 1996 – 2004 were improved, new structures were calculated for 2005 and 2006, and the new four-dimensional tomography program **dtomo** was applied to the whole period.
- *Subtask 2.3 Earthquake Mechanisms*: The enhanced moment tensor software was applied to seismic data associated with the EGS stimulation experiment in well 34A-9.

Task 3: Integration of results with other knowledge

The results were interpreted together with other geophysical, operational and EGS-related data. The most useful supporting data for the seismic results are:

- geological maps;
- hydraulic fracturing results;
- borehole logs;
- injection data including pressure and injection flow rate, and;
- tracer test results for monitoring the fate of injected fluids.

Full interpretation of the seismic results in the light of these data has been conducted. The results have revealed how effort should be focused in order to produce rapidly the most useful results in future experiments.

2.1 Significant departures from the work planned in the original proposal

1. Stimulation of well 46A-19RD was originally expected to occur in 2007 and considerable work was done at the wellhead by the Caithness Operating Company in February 2007. Unfortunately the well liner could not be removed on schedule, and the experiment is currently postponed to 2009 (Frank Monastero, personal communication).

2. The U.S. Navy upgraded security surrounding their computer network in 2006, so no access is now possible between their computers and off-base non-military computers. Some of the tasks that are now not possible to perform remotely are transfer of programs and files to the

Geothermal Program Office network, and retrieval of seismic data from U.S. Navy computers to *Foulger Consulting* or U.S. Geological Survey computers. As a result, considerably more time than planned had to be spent at the Geothermal Program Office at the U.S. Navy base, doing work directly on U.S. Navy computers. Many tasks were much more time-consuming than they were in the past. This significantly increased the project workload and prevented some planned project milestones from being completed on time. Nevertheless, with the 3-month no-cost extension granted to the project by DOE, all the original objectives have now been achieved.

3. Following initial exploratory work, it became clear that the benefit of using accurate relative hypocenter relocations in tomography at the Coso geothermal area, as originally intended, would be insignificant. The programming effort earmarked for Subtask 1.2 was thus redeployed to improve the tomography program in a more effective way. It was decided to adapt existing software to invert two epochs simultaneously for wave-speed structural changes, instead of using the old method of inverting each separately and differencing the results.

   Following this change of tack, it proved more complex than anticipated to upgrade the pre-existing Fortran tomography program (**simul2000A**). A second change of tack was thus made and an entirely new program, **dtomo**, was written in the C programming language. Despite two false starts on this subtask, the present outcome is very pleasing as an excellent new program is now available that does not suffer from any of the known bugs in the pre-existing program. It is also fully integrated with all other programs in our EGS-tailored software suite, it can read multiple formats, and will be readily adaptable by us for other EGS and geothermal targets.

3 Summary of project activities during the entire period of funding

3.1 Subtask 1.1: Relative relocation software development

The most accurate methods available for computing earthquake hypocenter locations use the differences in arrival times at seismometers for closely clustered earthquakes [*Waldhauser and Ellsworth*, 2000]. Because of the proximity of the earthquakes, the ray paths to each seismometer are nearly coincident and travel-time anomalies caused by unknown structure along the rays cancel out almost completely, leaving only effects related to the earthquake locations.

Most applications of these methods to date have used differential times obtained by simple subtraction of manually measured onset times. For typical earthquake data from geothermal areas, these are accurate to the order of 0.01 s. At least a factor of ten improvement may be achieved, however, by fine-tuning the manual measurements using a computer and digital seismograms, for example by cross-correlating the waveforms.

We completed a suite of computer programs, written in the C programming language, for enhancing time-difference data sets. The software starts with manually measured onset times (in this case, from the U.S. Navy catalog) that are simply subtracted from one another (program

cat2dt). It then improves them using digital seismograms and a cross-correlation (program **toonpics**). High-resolution hypocenter locations are finally computed from the resulting data sets (program **hypocc**).

As a preliminary step, adaptions were made of the optimized high-resolution hypocenter-location program as follows:

- Correction of geometrical distortions in the local coordinate system, most important at high latitudes.
- Use of true station elevations. **hypoDD**, the older-generation Fortran program (and most other hypocenter-location programs) assume all stations have the same elevation, biasing computed results and making utilization of data from borehole instruments impossible.
- Correct weight computation. The "weights" in **hypoDD** were the square roots of the correct values, and moreover weights for time differences were computed incorrectly from the weights of individual times.
- Use of modern algorithms, including hash tables and "kD trees" for rapidly searching station tables and earthquake catalogs.
- Representing event graphs with adjacency lists instead of adjacency matrices, effecting large memory savings because these graphs are sparse (typically only about 0.2% of possible links exist).
- Searching event graphs using depth-first-search (DFS) algorithms, which are thousands of times faster than sequential searching.
- Much more efficient storage of the (very sparse) condition-equation matrices, making feasible the analysis of much larger data sets.
- Efficient distance-azimuth calculations using geocentric direction cosines, avoiding most evaluations of trigonometric functions.
- Optimized seismic ray travel-time algorithms.
- Flexible choice of physical units and execution options, making easier application to, for example, oil-industry data (which commonly measure distance in feet).

We also corrected many small bugs. The new version, **hypocc** is a major improvement on the earlier version. **hypocc** uses the same formats as **hypoDD**, a feature designed to facilitate migration of data sets assembled for **hypoDD** to the new program suite.

Detailed manual pages for **cat2dt**, **toonpics** and **hypocc** that explain their usage and data formats are provided in Appendices 1, 2 and 3. All three programs also have built-in help options that provide on-screen usage assistance. Table 1 gives statistics about the sizes and complexities of these three programs.

Table 1. Source-Code Statistics

Program	Source files	Header files	Lines	Statements	Subroutines
cat2dt	22	22	3985	932	89
toonpics	35	16	5919	1926	142
hypocc	53	22	7765	2419	187

The new program suite is publicly available at the website ftp://ehzftp.wr.usgs.gov/julian . Under Subtask 2.1, it was applied to data associated with the EGU injections in wells 34A-9 and 34-9RD2, and prior to planned injection in well 46A-19RD.

3.2 Subtask 1.2: Time-dependent tomography software development

Studies at several geothermal areas have detected temporal changes in the seismic wave speeds, weak ones that are apparently of natural origin and stronger ones that probably result from economic exploitation [*Foulger et al.*, 1997; *Foulger et al.*, 2003]. Study of such changes and mapping them in detail holds promise for monitoring physical reservoir conditions and optimizing operational decisions.

Measurements of temporal changes have until now been determined using computer programs that assume temporal constancy, applying them to multiple data sets and assuming that any differences found result from structural variations with time within the Earth. Such an assumption is dangerous, however. The results of repeated tomography experiments would differ even if the structure did not change because of variation in the seismic ray distribution caused by the natural variation in earthquake locations. Even if the source locations did not change (if only explosion data were used, for example), derived structures would inevitably differ because of observational errors. These contaminating effects can be partially overcome by following complicated processing strategies, *e.g.,* using models derived for one epoch as starting models for another epoch, but these strategies are not optimal.

A much better approach is to invert multiple data sets simultaneously, which makes it possible to determine what changes are truly required by the data. This problem is similar to that of seeking models consistent with initial assumptions, and methods similar to the damped least squares method can solve it.

We initially set out to modify the widely used Fortran-language computer program **simul2000A** to produce a new program, **dsimul**, to invert multiple data sets simultaneously. **simul2000A** is a large and complicated program, consisting of 68 subroutines and 9000 lines of code, and it uses many obsolete and denigrated programming practices. For example, virtually all variables are stored in common blocks, and none are passed to subroutines directly. This practice severely hampers the ability of the optimization phase of a compiler by preventing it from using hardware

registers. Eliminating the common blocks and passing variables as arguments when needed sped the program up by nearly a factor of two.

We made the following improvements to **simul2000A**:

- It was re-structured in a major way as necessary for modification to treat multiple data sets and models.
- In the original program, most communication between subroutines takes place through Fortran common blocks, making it difficult to determine how information is initialized, transmitted, and modified. We restructured the code according to modern practice, so that all variables are passed explicitly to subroutines as arguments.
- Restructuring revealed many bugs which were corrected.
- Many variables and subroutines were identified as superfluous and excised.
- The revised program is functionally equivalent to earlier parent programs, but internally self-documenting and more standardized, understandable, maintainable, and modifiable.

We also found that many of the algorithms used, for example for computing distances and azimuths and for tracing rays, were much less efficient than alternatives now available, while several others, for example those used for making Earth-flattening approximations and for weighting data, were simply incorrect. Lastly, we found a bug that causes the program to produce different results when compiled with different compiler options. We spent a month compiling the program with a wide variety of compilers on a wide variety of machines, but were unable to find the source of this problem.

We therefore decided to change tack and write a completely new program, **dtomo**, from scratch, in the much more modern C programming language and using efficient algorithms already programmed and available. This proved to be a well-advised action. Not only was it a far superior approach, that provided a modern basis on which future work can be founded, but many of the necessary components existed already and so the work progressed rapidly.

We completed the program **dtomo**, a new "four-dimensional" (time-dependent three-dimensional) seismic tomography program [*Foulger et al.*, 2007]. **dtomo** simultaneously inverts multiple data sets from different epochs, calculating the temporal variations that are truly required by the observations.

Temporal differences in the structures calculated by traditional, individual inversions of seismic data from different periods may occur for a number of reasons. These include not only true changes in structure caused, for example, by geothermal production activities, but also differences from epoch to epoch in ray-path distributions, locations of the earthquakes, station locations, and statistical errors in the input data. The advantage of **dtomo** over traditional tomography inversion procedures is that it is immune to differences in the data sets and reports only the changes in Earth structure required by the data. Spurious temporal variations that are merely the artifacts of differences in the effective experimental setup from epoch to epoch are taken into account in the error budget and not reported as true changes in structure.

Some of the most noteworthy features of **dtomo** are as follows.

- The program features portable, object-oriented coding. It consists of 55 ANSI C-language source files and 22 header files, with 7343 lines of code. It is publicly available at the website ftp://ehzftp.wr.usgs.gov/julian
- It has a user-friendly interface. Run-time options can be controlled from either the command line, startup files, or both. Reasonable default values are adequate in most cases. There is an interactive help facility and an on-line reference manual (reproduced in Appendix 4).
- **dtomo** is capable of reading multiple input formats via the separate program **qpack**, which can parse seven different formats. Adding additional input formats is straightforward and it is anticipated that **qpack** will expand in future. An on-line reference manual is also available for **qpack**.
- Output formats have been made compatible with the existing "simul" family of tomographic inversion programs (*e.g.*, **simulps12**) in order to facilitate graphic display, and to encourage existing users of the "simul" program family to use **dtomo**.
- Computer memory is dynamically allocated. This avoids wastage of hardware resources. **dtomo** never requires re-compilation to handle larger input sets of earthquakes and grids with larger numbers of nodes.
- True three-dimensional seismic ray tracing us used. **dtomo** uses the "bending" method [Figure 1; *Julian and Gubbins*, 1977]. This is an improvement over the "approximate ray tracing" or "pseudo bending" used by the "simul" program family.
- Wave-speed interpolation within models is flexible and smooth. **dtomo** uses general tri-cubic functions, which include splines as a special case. This is an improvement over the trilinear interpolation used by the "simul" program family, since tri-cubic interpolation probably approximates Earth structure better.
- **dtomo** uses efficient computational algorithms for computing distances, azimuths, travel times, matrix inverses, etc. This makes for a faster-running program.
- **dtomo** is fast. It takes about 30 s per iteration for two epochs of data on a Macintosh G4 Powerbook Pro laptop computer. This may be compared with several minutes per iteration for a single epoch of data using programs of the "simul" family.

3.3 Subtask 1.3: Moment tensor software development

An essential component of any geophysical inverse method is the quantitative assessment of uniqueness. To draw scientific conclusions from observations it is necessary not only to determine the model parameters that best fit them, but also to know what other parameters would fit them acceptably well.

Subtask 1.3 required extending and improving existing user interfaces for applying complete moment-tensor mechanism software to earthquake data [*Julian*, 1986; *Julian and Foulger*, 1996]. Earlier methodologies were awkward to use, requiring many repetitive manual tasks.

Each earthquake took ~ 1 hr ± 30 min to process, depending on the number of stations and the compliancy of the data. Only a single result was generated, with no indication of uniqueness or error. In addition to permitting error assessment, the new interactive user interface has greatly speeded up the work such that ~ 30 min is now the average time taken to process an earthquake.

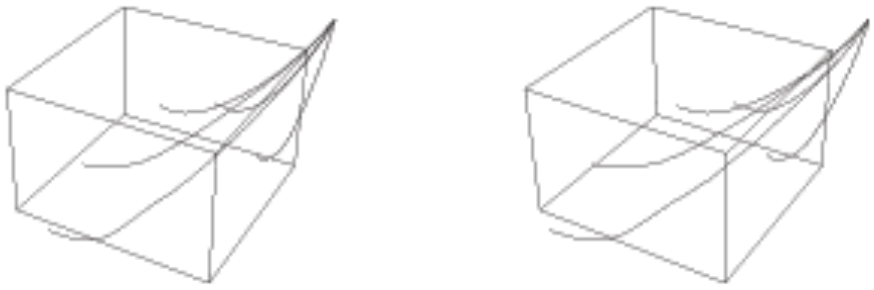

Figure 1: Stereo pair of images showing trajectories of rays calculated using the bending method of *Julian and Gubbins* [1977], which has been implemented in **dtomo**.

The following work was done:

- We extended the linear-programming code to find mechanisms that are extreme (maximizing user-specified functions such as volume change or horizontal extension) but still fit the observed data within their errors.
- We developed an interactive graphical user interface (GUI) that makes it easy to visualize the effects of using different subsets of the data and changing the weights given to them. This program runs at a level that is useful, it greatly speeds up the inversion process and enables visual assessment of stability of the result. An example of the visual display of the current version is shown in Figure 2:
- We upgraded the underlying programs **focmec** and **eqmec** to generate estimates of the uniqueness of derived earthquake mechanisms and thereby quantify errors as follows:
  - **focmec** was adapted to "push" mechanisms in specified directions as far as possible whilst still fitting the data satisfactorily.
  - The mathematical theory for analyzing data expressed in the form of ratios was developed. The use of ratios is helpful in analyzing seismic-wave amplitudes; if the ratios are chosen appropriately, wave-propagation effects, which are major sources of error, can be made to cancel out. The numerical values of ratios are unsuitable for use, however, because of their behavior when denominators become small. Our theory avoids such difficulties, providing a representation that is independent of which variable is taken as the denominator and gives correct statistical weights to ratios.

After completing this work, we added error assessment to the linear-programming focal-mechanism inversion method [*Julian*, 1986; *Julian and Foulger*, 1996] embodied in **focmec**. The linear-programming method finds the moment tensor that best fits a set of observed seismic-wave polarities, amplitudes, and amplitude ratios, in the sense of minimizing the L1 norm (sum of absolute values) of the misfits to the observations ("data residuals"). Our extension of the method determines what changes to this best-fit solution can be made while keeping the goodness of fit within a specified range. We formulate this task itself as a linear-programming problem, and solve it efficiently by standard methods.

To use the new method, the user must specify a number of "objective functions", linear combinations of the moment-tensor components that are to be maximized or minimized subject to keeping the L1 norm of the residuals within certain bounds that the user also specifies. Examples of such objective functions include the volume change, the amount of extension or compression in specified directions, and the similarity to particular chosen mechanisms.

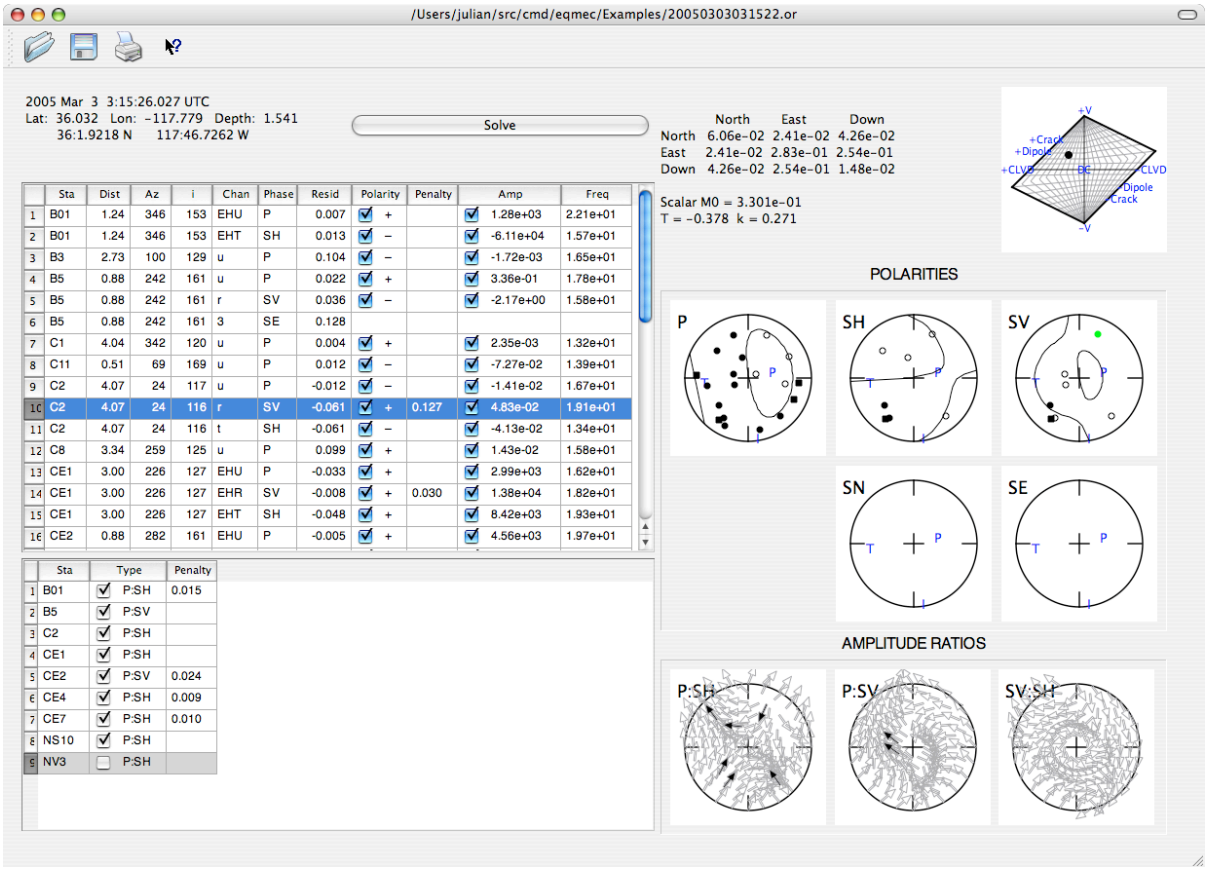

Figure 2: Example of the graphical user interface (GUI) developed to streamline moment-tensor analysis.

3.4 Subtask 2.2: Tomographic inversion for time-dependent changes in crustal structure

3.4.1 Strategy for independent tomographic inversions

In order to compare the final results from the new program **dtomo** with "standard" results, the data from Coso were first inverted for three-dimensional structure and structural change using the traditional approach. Tomographic inversions of data from years 2005 and 2006 were conducted, to add to the results already available from 1996 - 2004 under previous projects. Those results, including the inversion methodology, are described in detail by *Foulger* [2009]. The area studied is shown in the grid in Figure 3.

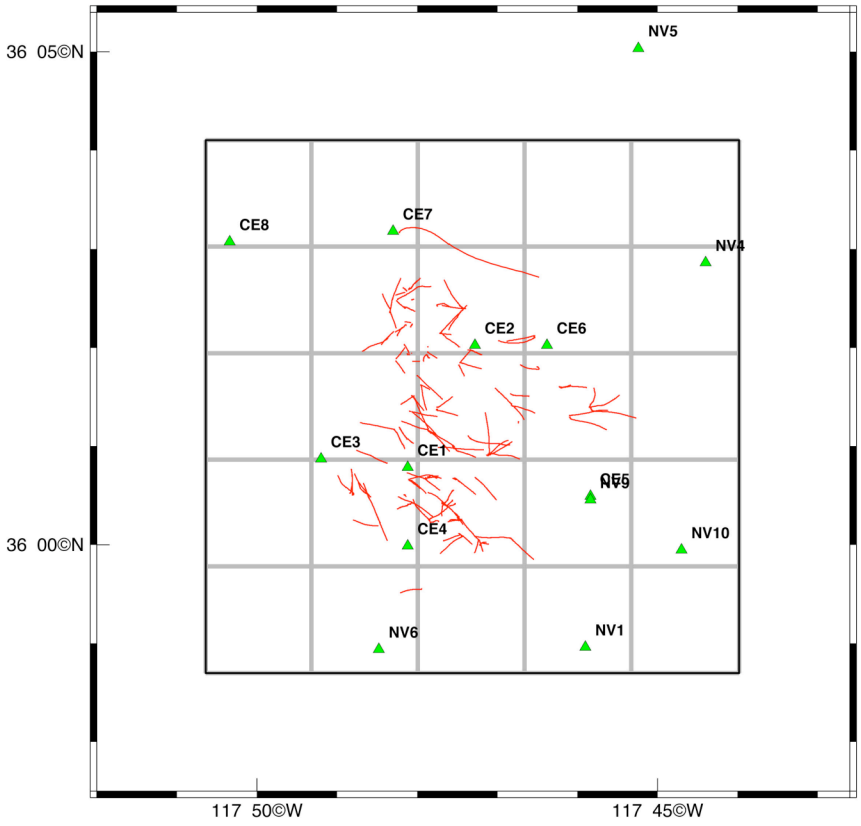

Figure 3: Map showing the square grid that encloses the area selected for the three-dimensional tomographic inversion. Red lines indicate the surface traces of geothermal boreholes, and green triangles indicate seismic stations.

The highest quality earthquakes recorded by the U.S. Navy seismic network are shown in Figure 4: Subsets were selected from the large number available in order to make inversions computationally practical. 791 and 821 earthquakes, evenly distributed throughout the volume of interest, were selected for 2005 and 2006 respectively.

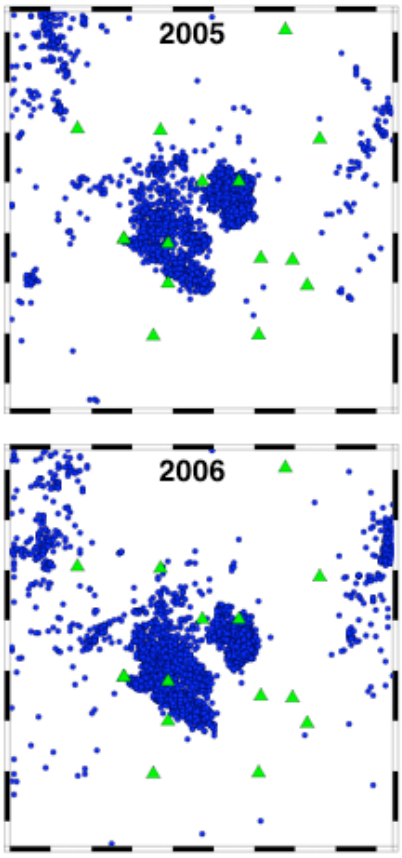

Figure 4: Map of the Coso geothermal area showing locations of all earthquakes from the U.S. Navy catalog files that occurred in the years 2005 – 2006, and that have high quality locations. Seismic stations (green triangles) are also shown.

Several inversion strategies were tried, as had been done earlier for data from years 1996 – 2004 [*Foulger*, 2008]. These included:

1. independent graded inversion of each year, on a grid with nodes separated by 2-km intervals,
2. same as 1. except for nodes separated at 1-km intervals,
3. "one-step" inversions using a common, average 3D starting model derived from a large inversion of all the data from 1997 – 2004. Six different inversions were performed, using six different starting models that varied according to nodal spacings and damping parameters used. Details of all the results are documented in *Foulger* [2009].

The best results were obtained for the inversion with nodal spacings of 2 km, using the independent, graded inversion approach (strategy 1. above). These results are shown in Figure 5.

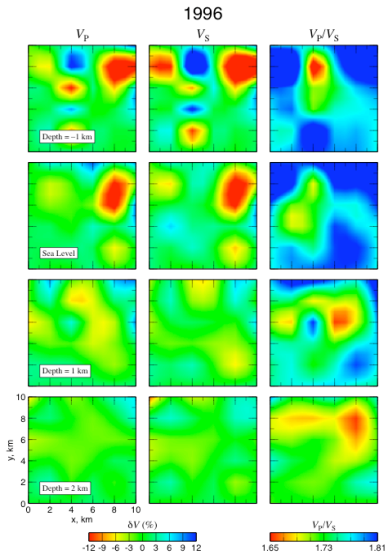
1996
V_P
V_S
V_P/V_S
Depth = −1 km
Sea Level
Depth = 1 km
Depth = 2 km
y, km
x, km
δV (%)
-12 -9 -6 -3 0 3 6 9 12
V_P/V_S
1.65 1.73 1.81

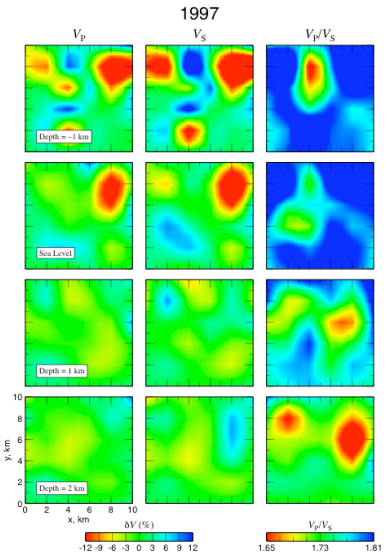
1997
V_P
V_S
V_P/V_S
Depth = −1 km
Sea Level
Depth = 1 km
Depth = 2 km
y, km
x, km
δV (%)
-12 -9 -6 -3 0 3 6 9 12
V_P/V_S
1.65 1.73 1.81

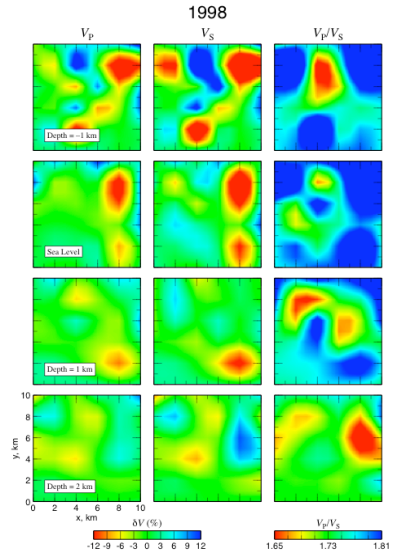
1998
V_P
V_S
V_P/V_S
Depth = −1 km
Sea Level
Depth = 1 km
Depth = 2 km
y, km
x, km
δV (%)
-12 -9 -6 -3 0 3 6 9 12
V_P/V_S
1.65 1.73 1.81

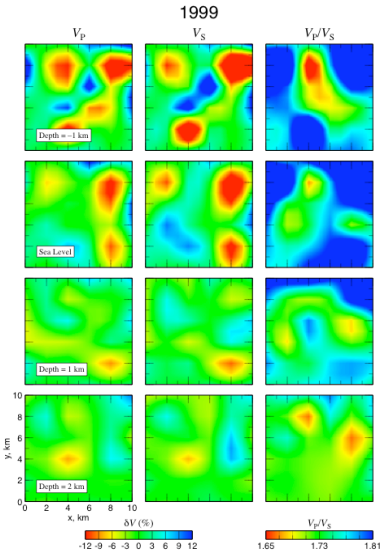
1999
V_P
V_S
V_P/V_S
Depth = −1 km
Sea Level
Depth = 1 km
Depth = 2 km
y, km
x, km
δV (%)
-12 -9 -6 -3 0 3 6 9 12
V_P/V_S
1.65 1.73 1.81

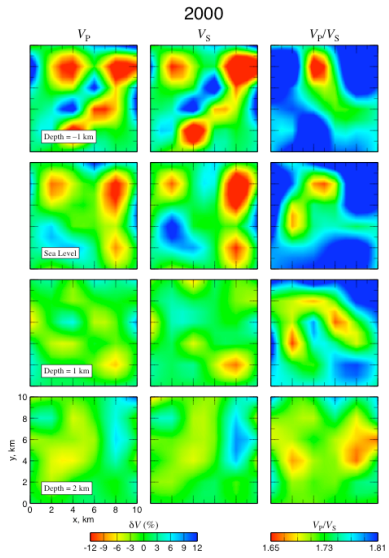
2000
V_P
V_S
V_P/V_S
Depth = −1 km
Sea Level
Depth = 1 km
Depth = 2 km
y, km
x, km
δV (%)
-12 -9 -6 -3 0 3 6 9 12
V_P/V_S
1.65 1.73 1.81

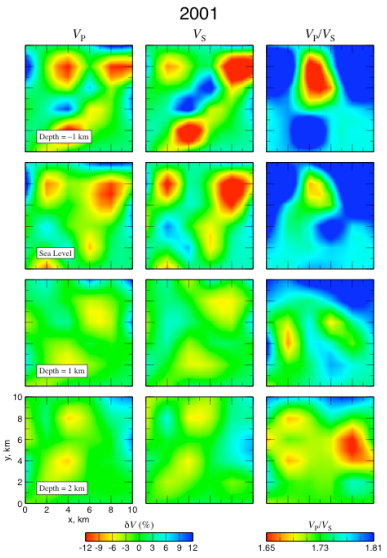
2001
V_P
V_S
V_P/V_S
Depth = −1 km
Sea Level
Depth = 1 km
Depth = 2 km
y, km
x, km
δV (%)
-12 -9 -6 -3 0 3 6 9 12
V_P/V_S
1.65 1.73 1.81

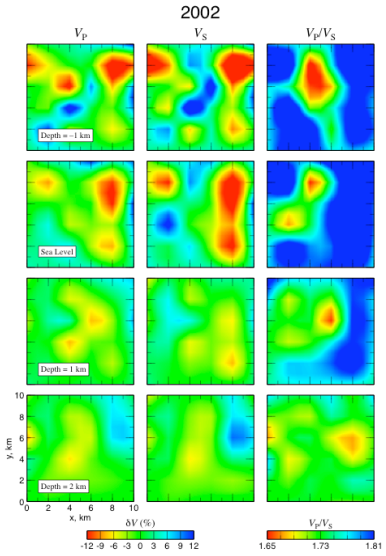
2002
V_P
V_S
V_P/V_S
Depth = −1 km
Sea Level
Depth = 1 km
Depth = 2 km
y, km
x, km
δV (%)
-12 -9 -6 -3 0 3 6 9 12
V_P/V_S
1.65 1.73 1.81

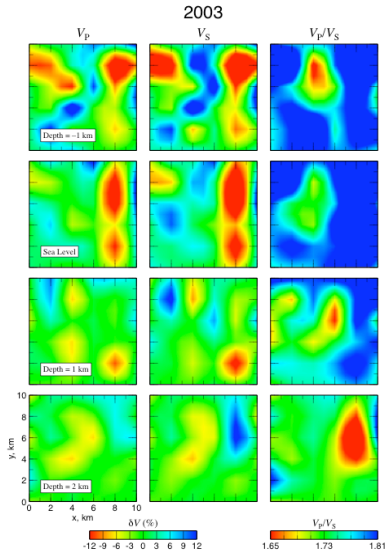
2003
V_P
V_S
V_P/V_S
Depth = −1 km
Sea Level
Depth = 1 km
Depth = 2 km
y, km
x, km
δV (%)
-12 -9 -6 -3 0 3 6 9 12
V_P/V_S
1.65 1.73 1.81

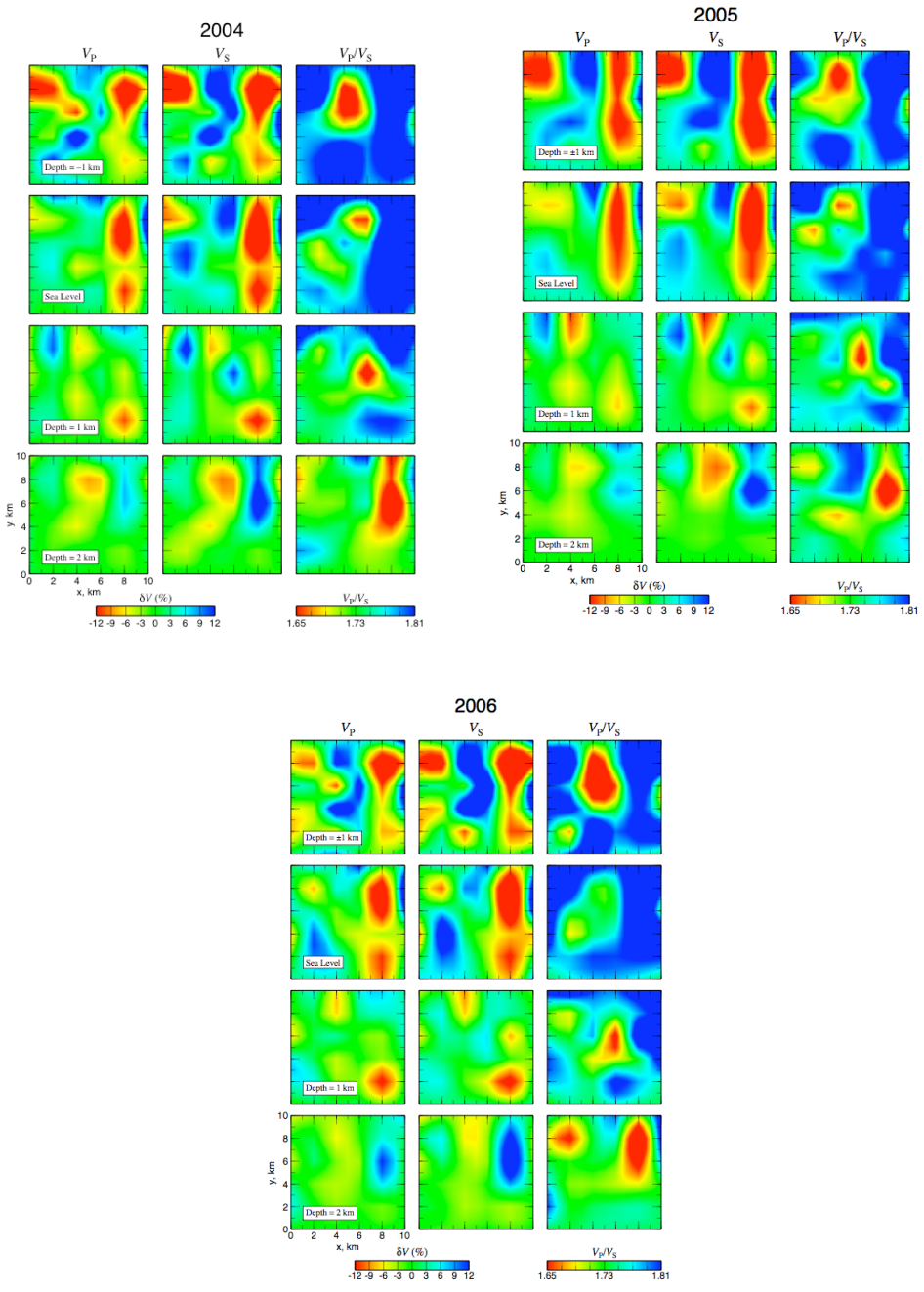

Figure 5: Results of inversion of individual years independently, with 2-km nodal spacings.

3.4.2 Results of independent tomographic inversions

In the following discussion, co-ordinates are given as (x,y) using the axis labeling system shown in the bottom left-hand panels for each year, in Figure 5. The major anomalies, *e.g.,* as imaged

using the data from 2006, and that correlate with geological, morphological and geothermal features, are as follows.

A major low-*Vp* and low-*Vs* structure with a bipartite, hourglass shape extends from ~ (8,8) to (8,2) throughout the depth slices –1 and 0 km b.s.l. The southern part appears to extend into the 1 km b.s.l. depth slice. This anomaly correlates closely with the Coso Wash in the eastern part of the Coso geothermal area, and probably represents sedimentary valley fill. The results thus suggest that this valley extends from the surface to at least sea level in its northern part (the upper Coso Wash area) and to at least 1 km b.s.l, in its southern part (Coso Basin). Its vertical extent is thus 2-3 km beneath the upper Coso Wash area and 3-4 km beneath Coso Basin. The central part of the area has relatively high wave speeds in the upper 2 km.

The *Vp/Vs* field shows a major low-*Vp/Vs* anomaly at –1 km b.s.l. that correlates closely with the northern part of the geothermal wellfield. The wellfield south of this is characterized by high-*Vp/Vs* values. The low *Vp/Vs* anomaly is strongest in the uppermost 1 km, but may extend as deep at 1 km b.s.l. It is chararacterized by high *Vp* but even higher *Vs*. Thus it results from anomalously high *Vs* rather than anomalously low *Vp*.

The objective of inverting each year separately was to investigate possible changes in structure with time that might be related to geothermal operations. In particular, previous work at The Geysers geothermal area and Mammoth Mtn., both in California, revealed temporal structural changes that were related to geothermal fluid withdrawal at The Geysers [*Gunasekera et al.*, 2003] and CO_2 degassing at Mammoth Mtn. [*Foulger et al.*, 2003]. In particular the *Vp/Vs* ratio is powerful to reveal changes.

Of particular interest is the low-*Vp/Vs* anomaly that correlates with the geothermal field. This anomaly is strongest in the shallowest depth section (–1 km b.s.l.), and weakens at sea level.

In the independent inversions, the anomaly in the shallowest two depth sections strengthened overall throughout the period 1996 – 2006. The strengthening was irregular from year to year. This result may be compared with The Geysers geothermal field. There, a clear strengthening of a low-*Vp/Vs* anomaly associated with steam extraction was detectable in inversions conducted for data collected at 2-year intervals 1991 – 1998 [*Gunasekera et al.*, 2003]. During this period steam production was 7 – 9 x 10^{10} kg/yr [*Barker et al.*, 1992]. In comparison, fluid extraction from the Coso geothermal field for the period 1996 – 2006 has been fairly steady and approximately 4 x 10^{10} kg/yr, along with injection at a steady rate of approximately 2 x 10^{10} kg/yr (Keith Richards-Dinger, personal communication). The net fluid loss rate is thus approximately 2 x 10^{10} kg/yr, which is approximately 25% of that at The Geysers during the period of strong structural change there. It thus might be expected that detectable structural changes at Coso might be expected to occur on a time scale of ~ 10 years.

Figure 5 shows that the low-*Vp/Vs* anomaly is stronger in the last few years of the 11-year time period studied, compared with the first few years. This suggests qualitatively that the Coso geothermal field is behaving in a similar way to The Geysers field, but at a lower rate as a result

of the much lower net fluid loss rate achieved by more modest production and significant reinjection. At sea level and 1 km b.s.l. systematic temporal variations are less clear.

The low-*Vp/Vs* anomaly is associated with high and increasing *Vp* and *Vs*, but *Vs* increases at a greater rate than *Vp*. Processes expected to be associated with geothermal operations that can increase the value of *Vs* compared with *Vp* include:

1. steam flooding which lowers *Vp* more than *Vs* by increasing the compressibility of the pore fluid,
2. decrease in fluid pressure, which raises *Vs* more than *Vp*, and;
3. drying of certain argillaceous minerals such as illite.

These processes are illustrated schematically in Figure 6. All of these factors are expected when reservoir fluids are depleted, but only the latter two involve increases in the wave speeds. The temporal changes observed are thus consistent with pressure decrease and mineral drying in the reservoir, but not the replacement of liquid pore fluid with steam, unless this effect is camouflaged by stronger wave-speed increases caused by the other two processes.

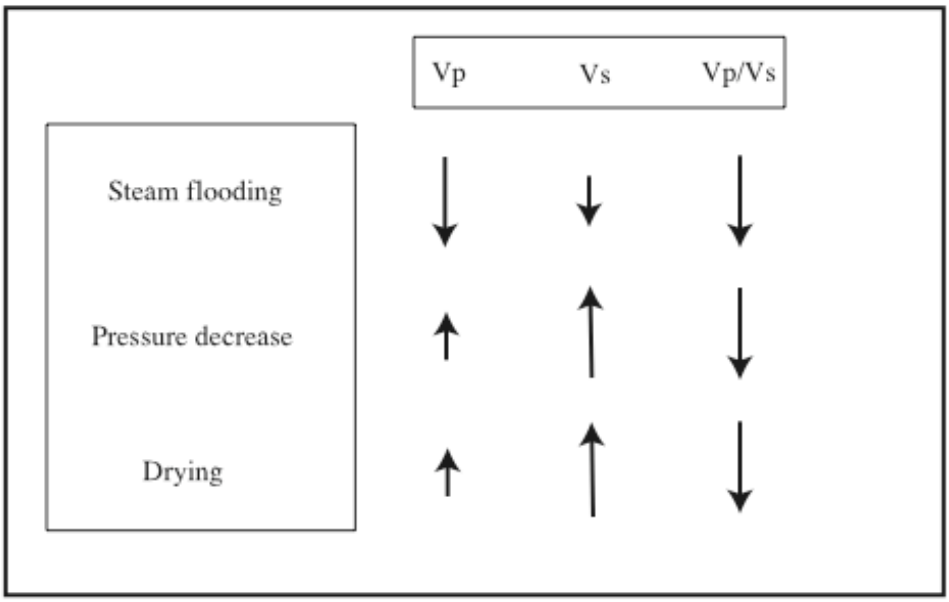

Figure 6: Schematic figure illustrating the effects of processes caused by exploitation on *Vp*, *Vs* and *Vp/Vs*. Long arrows indicate qualitatively the strengths of the effects, for each of the three processes illustrated. They have different effects on *Vp* and *Vs* but all cause *Vp/Vs* to decrease.

3.4.3 Tomographic inversion of all epochs using **dtomo**

The P- and S-wave arrival time measurements from the U.S. Navy catalog for 1996 and 2006 were inverted using the new program **dtomo**. The results are shown in Figures 7 and 8. The two data sets were inverted simultaneously with constraints imposed to minimize temporal changes. The differences in structure between Figures 7 and 8 thus represent a conservative estimate of structural change in the intervening 10-year period.

The major changes in structure over the 10-year study period are:

- at 1 km above sea level the high-wave speed anomaly in the centre of the imaged area became stronger. The increase in strength of the *Vs* anomaly was larger than that of the P-wave anomaly;
- at sea level the low wave anomalies associated with Coso Wash weakened;
- at 1 km below sea level, a high-*Vs* anomaly developed in the centre of the imaged area;
- at 2 km below sea level, significant changes in structure were not detected.

These results may be compared with those inferred from the traditional inversions. Concerning the general tomographic structure, the results are similar, validating the new program. Concerning change in structure, the reduction in *Vp/Vs* in the center of the field at 1 km above s.l. is confirmed, since *Vs* is found to increase faster than *Vp* (compare top right panels of Figures 7 and 8). The new results suggest that this may also extend beneath the Coso Wash area.

A new result is that this increase may extend weakly down into the depth slice at 1 km b.s.l. This suggests that structural change resulting from production may extend throughout the upper 3 km of the geothermal field. This is an intuitive result as production wells are typically 2 - 3 km deep, and seismicity, much of which doubtless represents reservoir response to production, occurs at these depths.

3.5 Subtasks 2.1, 2.3 & Task 3: Earthquake results for EGS experiments, and integration with other data

3.5.1 Overview

The work of subtasks 2.1, 2.3 and Task 3 involved applying the methods improved and extended under Task 1 to data from the Coso geothermal area and integrating the results with other data. Relative hypocenter relocations and moment tensors were calculated for earthquakes induced by two EGS experiments, in well 34A-9 (August 2004) and well 34-9RD2 (March 2005). The new methods were also applied to the background seismicity in the vicinity of well 46A-19RD for the month of January 2007, in anticipation of an injection experiment scheduled for February 2007. In the event, this experiment did not go ahead and is currently planned for 2009.

3.5.2 Background to the EGS experiments

The Coso geothermal area, in the southern Owens Valley in SE California, lies in a right

releasing step between the right-lateral Little Lake fault zone to the SW and the Wild Horse Mesa fault to the NE. The whole zone exhibits 6.5 ± 0.7 mm/year of dextral shearing [*Monastero et al.*, 2005]. The area exhibits two families of faults (Figure 9):

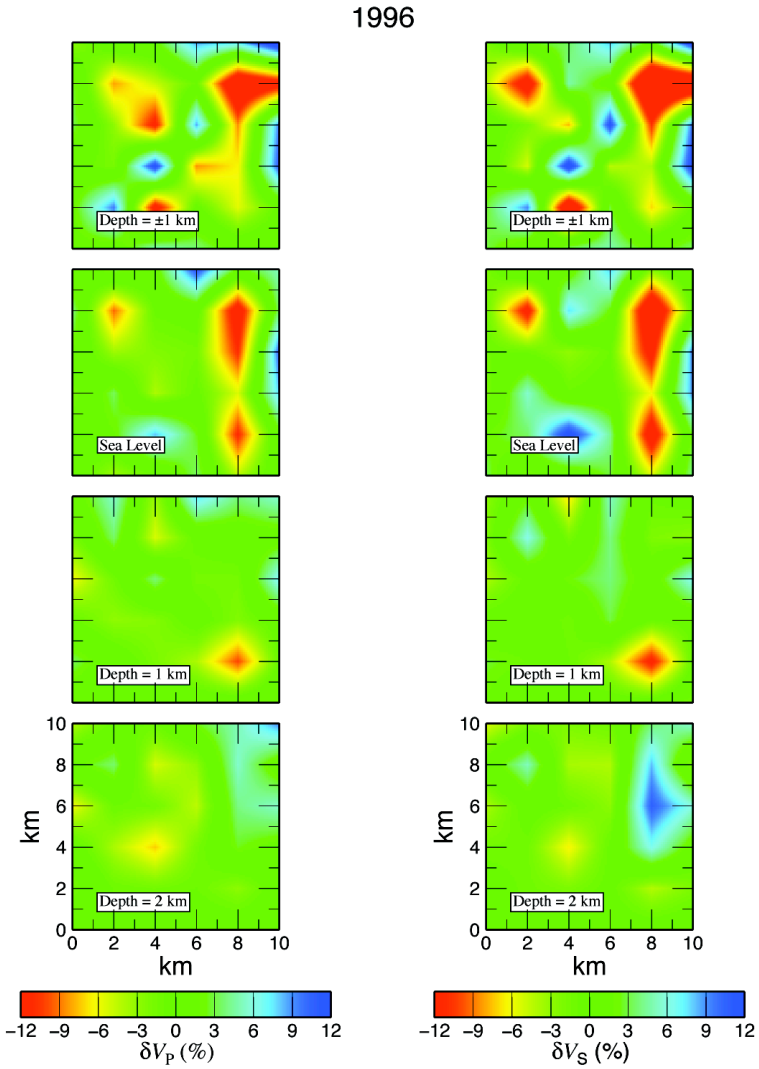

Figure 7: Maps of the seismic-wave speeds at different depths in the Coso geothermal area for 1996, as determined by inverting P- and S-wave arrival times from local microearthquakes observed on the U.S. Navy's permanent seismometer network. Data for both 1996 and 2006 were inverted simultaneously and constraints were imposed to minimize temporal changes.

1. WNW-trending and minor NE-trending faults, which are probably dextral and sinistral strike-slip faults respectively [*Duffield et al.*, 1980]. These faults may currently be inactive as they are not observed to offset Quaternary sediments.

2. N to NNE-trending faults, dipping to the W and E. The most prominent of these is the Coso Wash normal fault which essentially demarcates the eastern margin of the geothermal field. It comprises several en-echelon NNE-SSW-trending segments connected by NW-trending faults. This fault family is currently active since it has Quaternary geomorphological expression and offsets hydrothermal features and lava flows.

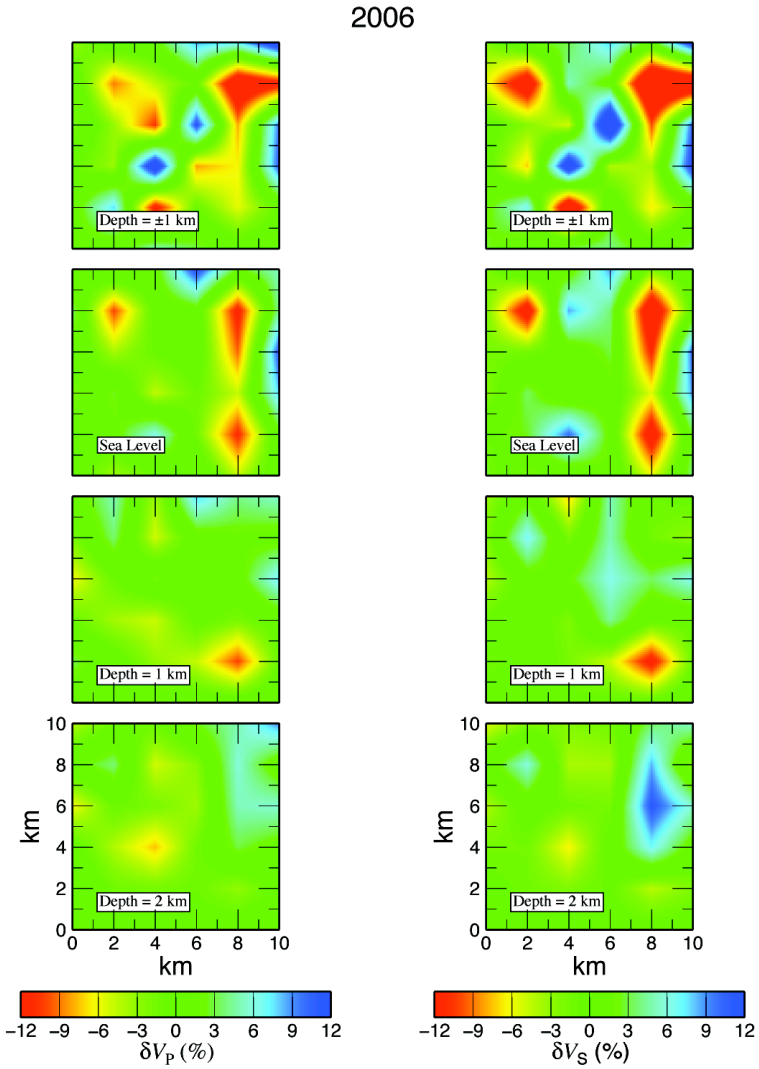

Figure 8: Same as Figure 7 but showing the results for 2006.

The Coso area is divided up by the main faults into three main sub-regions (Figure 10), the Main Field, a central spine of exposed bedrock which includes the East Flank of the geothermal area, and Coso Wash to the east [see *Rose et al.*, 2006 for summary]. The Main Field is highly active seismically, and has temperatures up to ~ 340˚C in the top ~ 3 km (640ºF and 10,000 ft depth).

The intensely normal-faulted eastern margin of the central spine contains the East Flank reservoir, which is also seismically active and associated with high temperatures. The East Flank lies on the footwall side of a step between two Coso Wash normal fault segments. Coso Wash is a series of sub-basins associated with segments of the Coso Wash fault and has low seismicity and temperatures. The intersection of the N to NNE normal faults with the WNW faults dissects all three regions of the geothermal field into rhombohedral fault-bounded blocks. Geological mapping and study of earthquake activity there indicates that the area is actively extending. The geothermal manifestations of the area are typically associated with the intersections of these two families of faults.

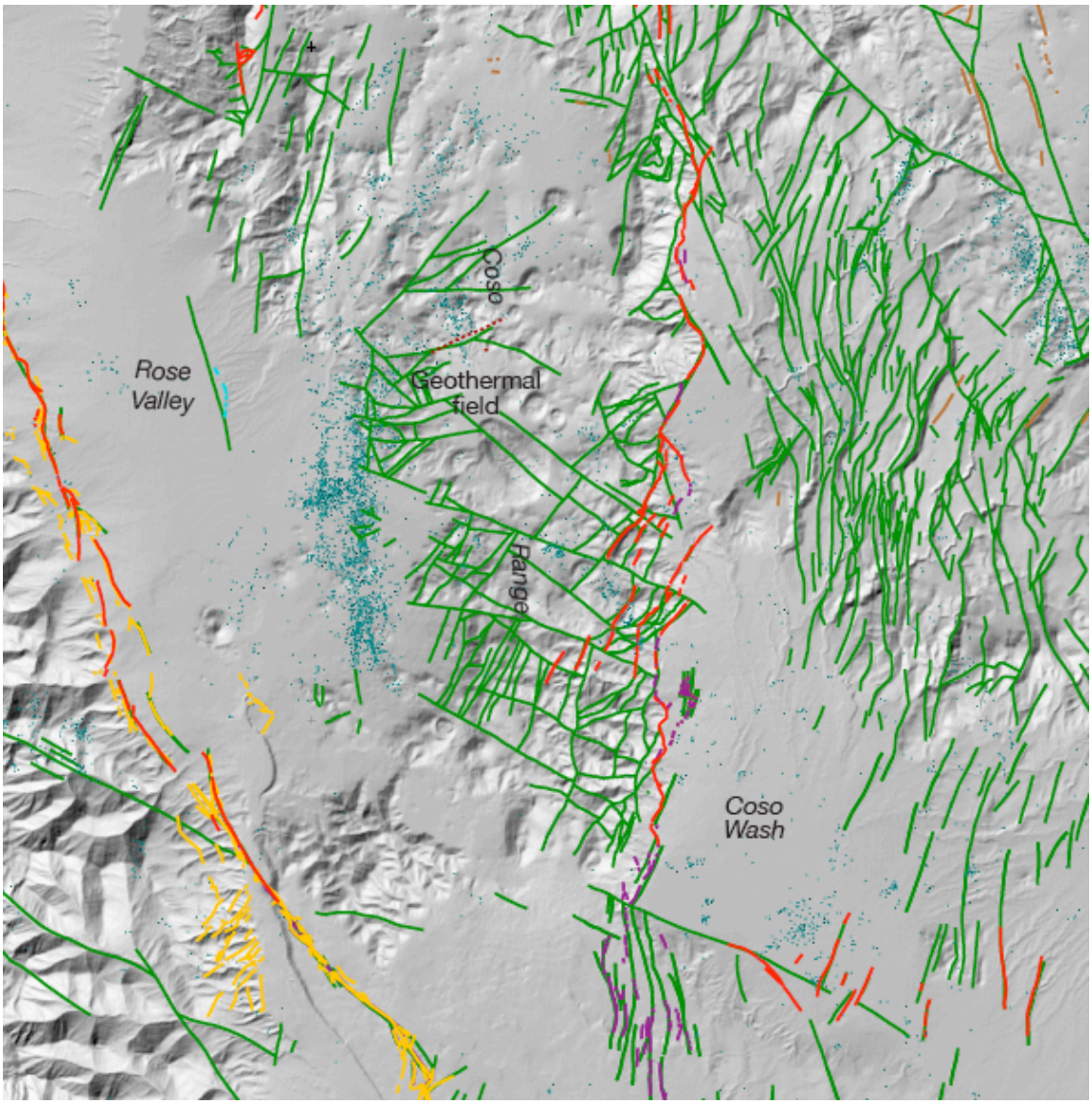

Figure 9: Compilation of faults in and around the Coso geothermal area. Green: [*William Lettis & Associates*, 2004]

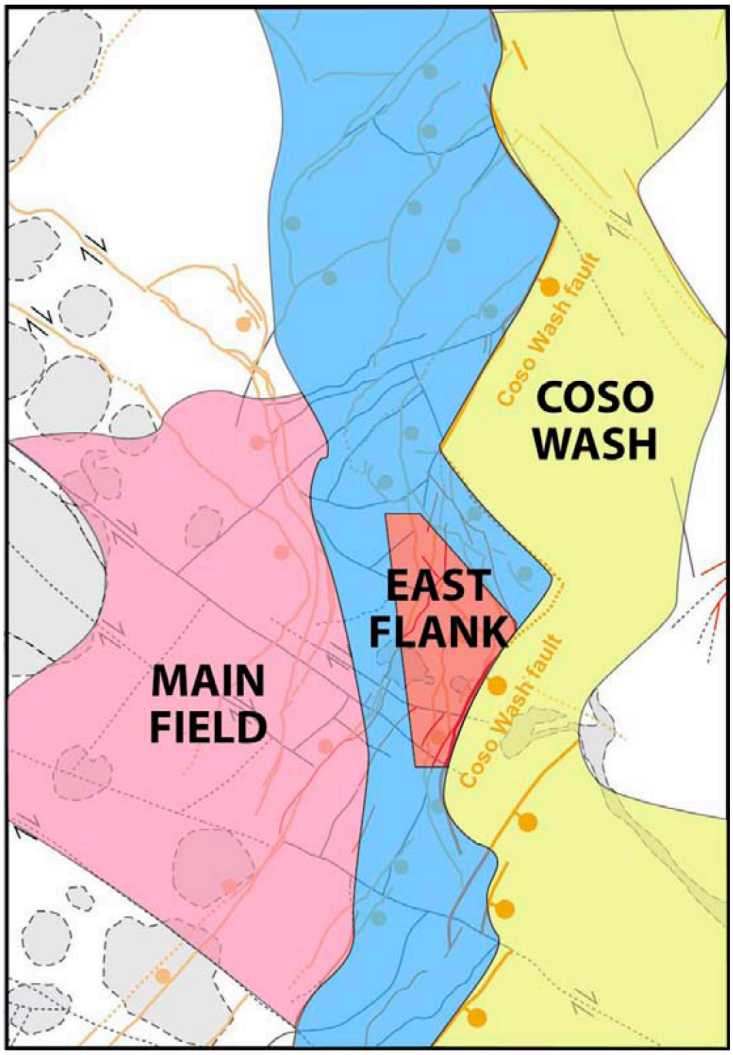

Figure 10: Fault-controlled sub-divisions of the Coso geothermal area. These sub-divisions are distinct as regards temperature and seismicity. The Main Field and the East Flank are the primary producing and seismically active regions.

Several hydraulic fracturing stress tests have been conducted in boreholes in the East Flank area and in Coso Wash. These tests have confirmed that the faulting regime of the East Flank is transitional from normal to strike-slip. The relative magnitudes of ambient stresses are such that normal faulting can be induced by increases in reservoir pressure of > 3.5 MPa (~500 psi), and strike-slip faulting by lesser pressure increases. The mean azimuth of S_{Hmin} throughout both areas is ~ 108˚ ± 24˚ (Figure 11), which is consistent with the presumed-active N to NNE-striking normal faults. In East Flank wells, some rotation of the stress orientations occurs near large-aperture faults visible in image logs. The upper bounds on S_{Hmax} in East Flank wells are such that strike-slip failure on optimally oriented faults is indicated, though if S_{Hmax} is in fact smaller than these upper bounds, the region could be near to the transition between strike-slip and normal failure [*Davatzes and Hickman*, 2007].

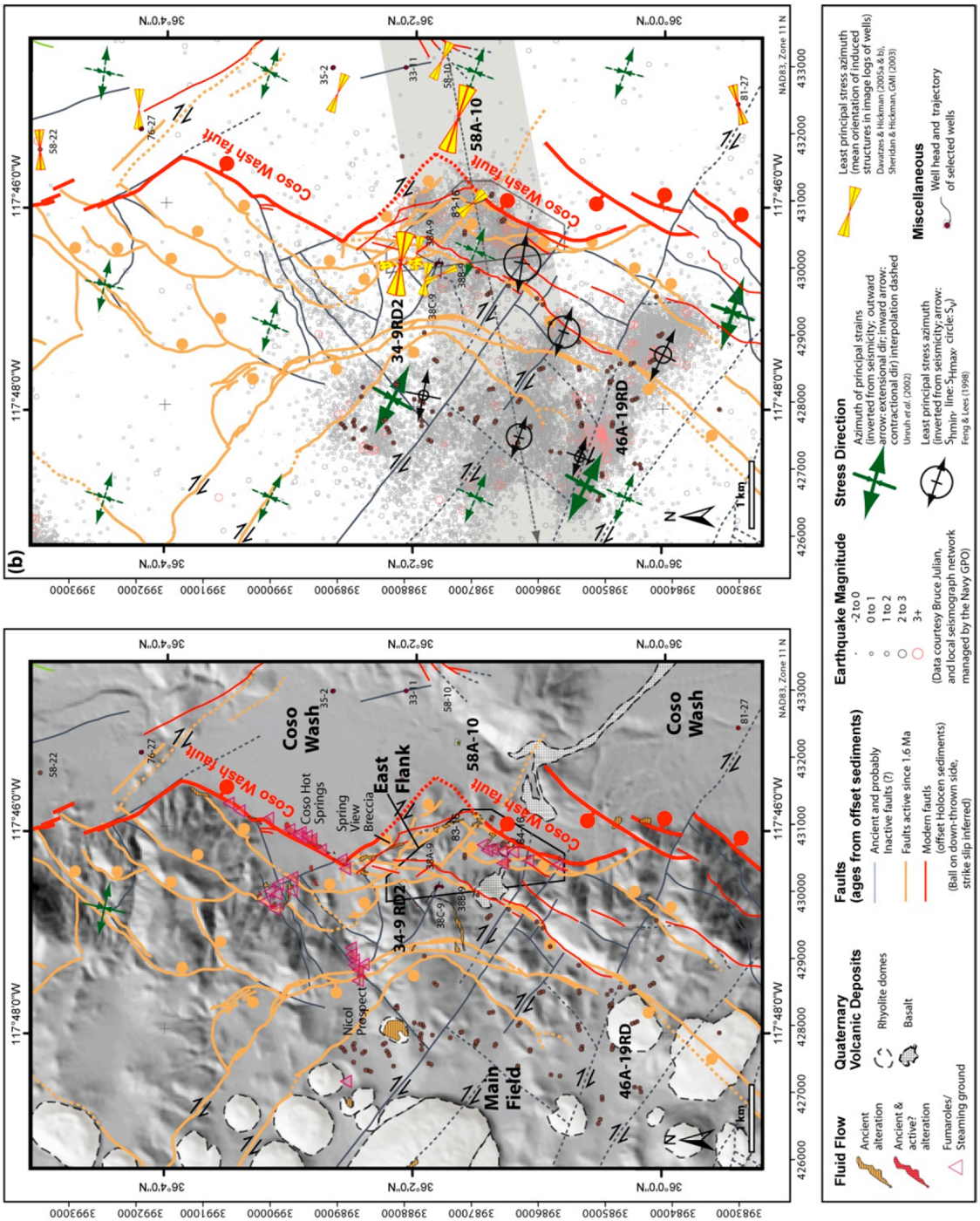

Figure 11: (a) Tectonic map of the East Flank of the Coso geothermal field over shaded relief image of topography, (b) Minimum horizontal stress orientations inferred from borehole image logs [from *Davatzes and Hickman*, 2007].

Normal faulting is commonly observed on surface faults in the East Flank, suggesting that a transition from normal to strike-slip faulting may occur with depth. Hydraulic fracture tests in wells in Coso Wash indicate that there a nearly pure strike-slip faulting stress regime exists on well-oriented faults.

The geological best case stress scenario that has been modeled using the hydraulic fracturing stress test results predicts near-failure stress on a variety of fault orientations. These include both active normal faults along the eastern fault boundary of the East Flank, and normal and strike-slip faults further west within the Main Field. This is broadly consistent with earthquake focal mechanisms throughout the field, which indicate both normal and strike-slip seismogenic motion.

Attempts have also been made to map spatial variations in stress using earthquake focal mechanisms [*Feng and Lees*, 1998; *Unruh et al.*, 2002]. The results show generally uniform directions throughout the field. However, if applied under the assumption of shear failure only, may not have sufficient resolution to detect relatively subtle variations in stress orientation throughout the field, and with depth.

The East Flank part of the Coso geothermal area is the main focus of the EGS experiments studied in the present project. A map of producing and injecting wells operating in this area is shown in Figure 12, and a schematic north-south cross section is shown in Figure 13. The wells are shown as vertical lines in Figure 13, although they are actually deviated, as shown in Figure 12. The mineralogy of rock chippings retrieved from both wells on pad 34 suggests that present temperatures are up to ~ 100˚C higher than temperatures that pertained earlier, when the minerals were deposited.

Two EGS experiments were studied as part of this project:

1. Well 34A-9, stimulated 6th - 18th August, 2004,
2. Well 34-9RD2, stimulated 2nd - 4th March, 2005.

These two wells comprise a pair of injectors on the northern edge of the East Flank area. This locality has relatively poor permeability and is thus unsuited to production. However, injection into these wells can potentially enhance production in wells to the south where permeability is higher, in particular the producing wells on pad 38 which lies ~ 500 m south of pad 34 (Figure 14).

3.5.3 Seismic data used

The Coso geothermal area is potentially ideal for testing state-of-the-art seismological techniques for geothermal operations monitoring, in particular EGS experiments. It is excellently instrumented with a network of 22 three-component seismometers installed at depths of ~ 100 m in shallow, custom-drilled boreholes.

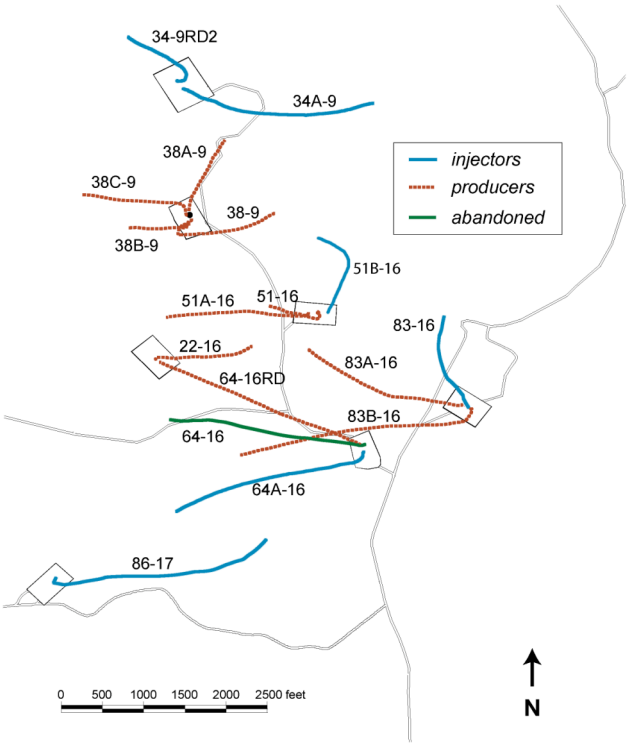

Figure 12: Locations and trajectories of wells in the East Flank of the Coso geothermal area [from *Rose et al.*, 2005].

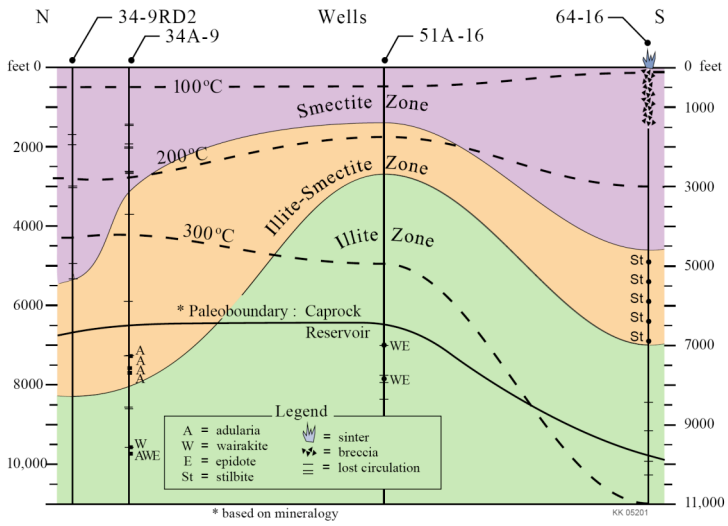

Figure 13: Simplified north-south cross-section of the East Flank. Present-day isotherms are dashed, and mineralogical zones indicating palaeotemperatuers are colored. The inferred paleosystem boundary between the caprock and the reservoir based on the mineralogy is shown as a solid line [from *Rose et al.*, 2006]. The maximum temperature at which smectite is stable is ~ 180˚C, and illite-smectite becomes unstable at ~ 225˚C.

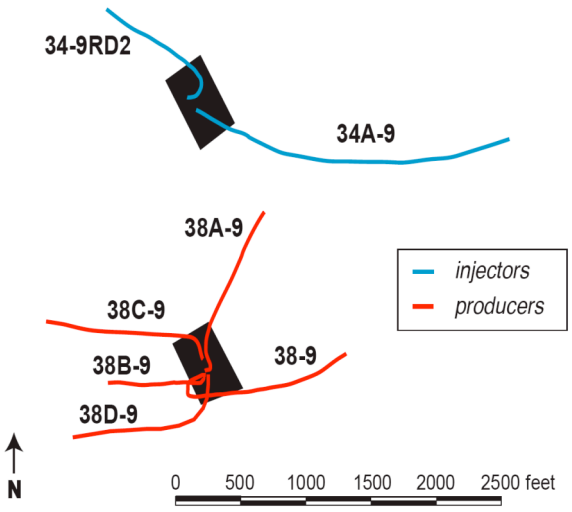

Figure 14: Wells from pads 34 and 38 in the northern part of the East Flank of the Coso geothermal area.

In order to enhance still further the excellence of the network geometry, specifically for the EGS experiments, the U.S. Navy supplemented the permanent network with a network of 16 surface three-component seismic stations. This network was first installed in the fall of 2003 around the EGS targets on the East Flank (wells 34A-9 and 34-9RD2) and later moved to surround well 46A-19RD. The locations of the stations for these two temporary deployments were optimised by performing ray tracing through the 3D Coso crustal velocity model. This technique comprises mapping how the focal sphere around a hypothetical earthquake would project onto the Earth's surface (Figure 15). The optimal station configuration for calculating earthquake moment tensors will involve stations evenly distributed in azimuth (radial lines in Figure 15) and take-off angle (quasi-circular lines in Figure 15) on the focal sphere. Where there is significant three-dimensionality in the crustal structure, this will correspond to a non-uniform distribution on the Earth's surface, as shown by the "spider's web" in Figure 15.

The network in place that monitored the injection tests in wells 34A-9 and 34-9RD2 is illustrated in Figure 16. Combination of the permanent and temporary networks provided what is probably the best EGS earthquake monitoring network ever deployed.

Following the injection in well 34-9RD2, and in preparation for an injection test in well 46A-19RD in the south of the Main Field, the temporary network was redesigned using the same technique (Figure 17). Some of the original sites in the southern part of the first temporary deployment were retained and served well as northernmost temporary stations to monitor activity around 46A-19RD. The northernmost stations of the original temporary network were redeployed close to, and to the NW, W, SW and S of well 46A-19RD. They provide vital coverage of parts of the focal sphere that would otherwise have been unmonitored. A large gap

in the total network greatly hampers moment tensor calculation, which is dependent on good azimuthal and focal sphere coverage.

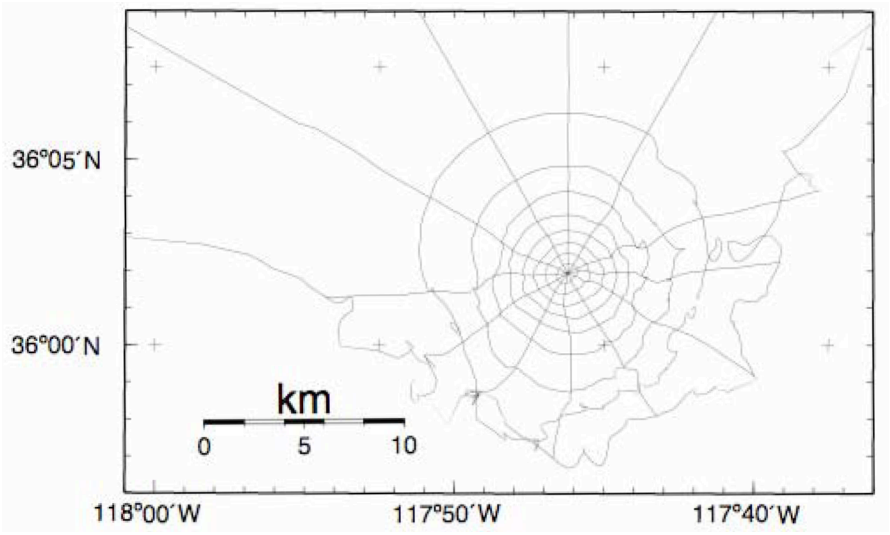

Figure 15: Map showing the parallels and meridians of the upper focal sphere of an earthquake, as projected onto the Earth's surface, obtained by tracing seismic rays through a three-dimensional crustal model for Coso. The earthquake in this example lies 3 km below the surface at well 34-9RD2. Seismic rays traced from locations on or near the Earth's surface will project onto an imaginary sphere around the hypocenter. For even coverage of this focal sphere, required for the best possible moment tensors, seismic stations should be distributed evenly with respect to these parallels and meridians. This will yield a better result than simply spacing them evenly on the surface.

Considerable work was also done prior to the work reported here, to determine the polarities and orientations of all the seismometer components. In the case of the sensors mounted in boreholes, nothing was known about the orientation of the horizontal components, since borehole instruments rotate by an unknown amount during installation. This was not a problem with the surface instruments as they could be orientated accurately with respect to magnetic north at the time of installation. However, all three components of both the borehole and the surface instruments had also to be checked for reverse polarization, a manufacturing problem that in practice typically occurs in 10% or so of all seismometer components.

The required calibrations were obtained by combining a suite of data. This included assembling earlier information from the permanent network, dropping weights vertically onto the surface sensors, and studying suites of fault-plane solutions to determine if individual stations appeared to have consistent normal or reversed responses. The response of horizontal sensor components to earthquake waves arriving from known azimuths was also studied, along with the directions and amplitudes of first arrivals recorded from a blast fired on the weapons test site April 6th 2005.

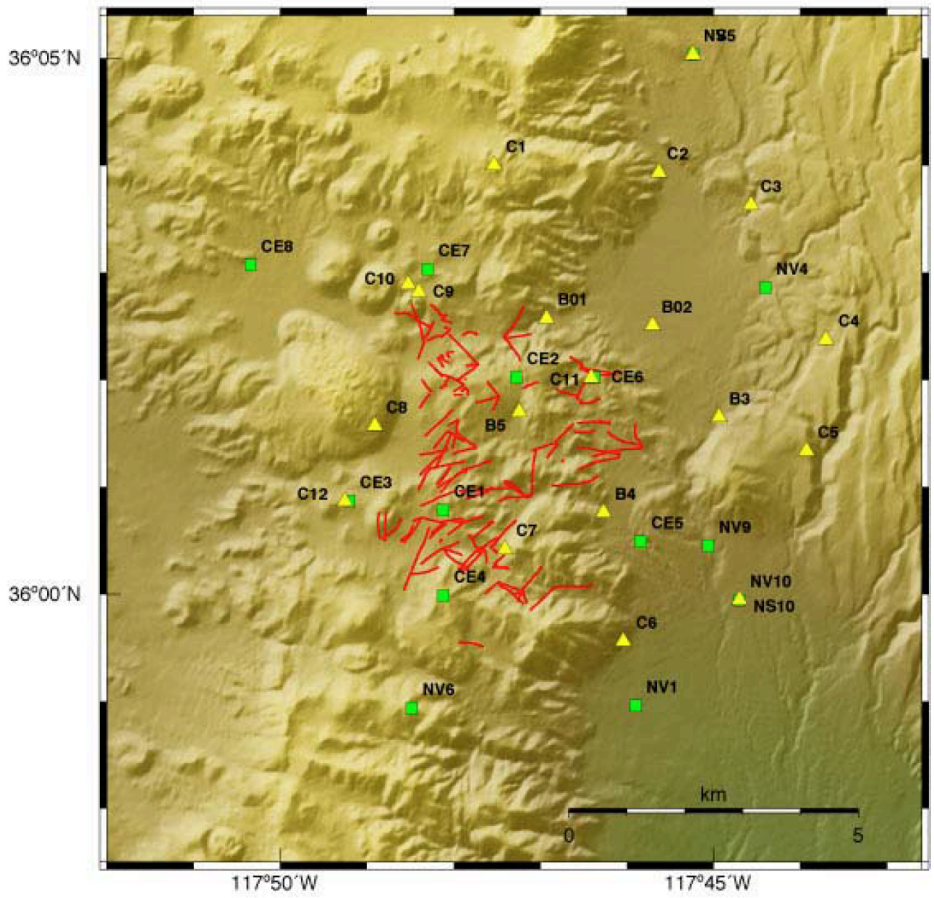

Figure 16: Seismometers at the Coso geothermal area at the end of 2005. Red lines: surface borehole traces; green squares: permanent telemetered stations; yellow triangles (B01, B02, B3-B5 and C1-C10): temporary stations installed to improve focal-sphere coverage for earthquakes near wells 34A-9 and 34-9RD2. At most 16 temporary sites were occupied at any one time. Data at most of the temporary stations were recorded on computer disks deployed in the field and periodically downloaded manually.

The success of the work reported here was also underpinned by extensive work performed over several of the preceding years to assemble, archive and translate incoming data into formats compatible with existing software and the software developed for this project. Much of this work was performed by the U.S. Geological Survey under DOE Award DE-FC07-011D14186, and funding from the Geothermal Program Office of the U.S. Navy.

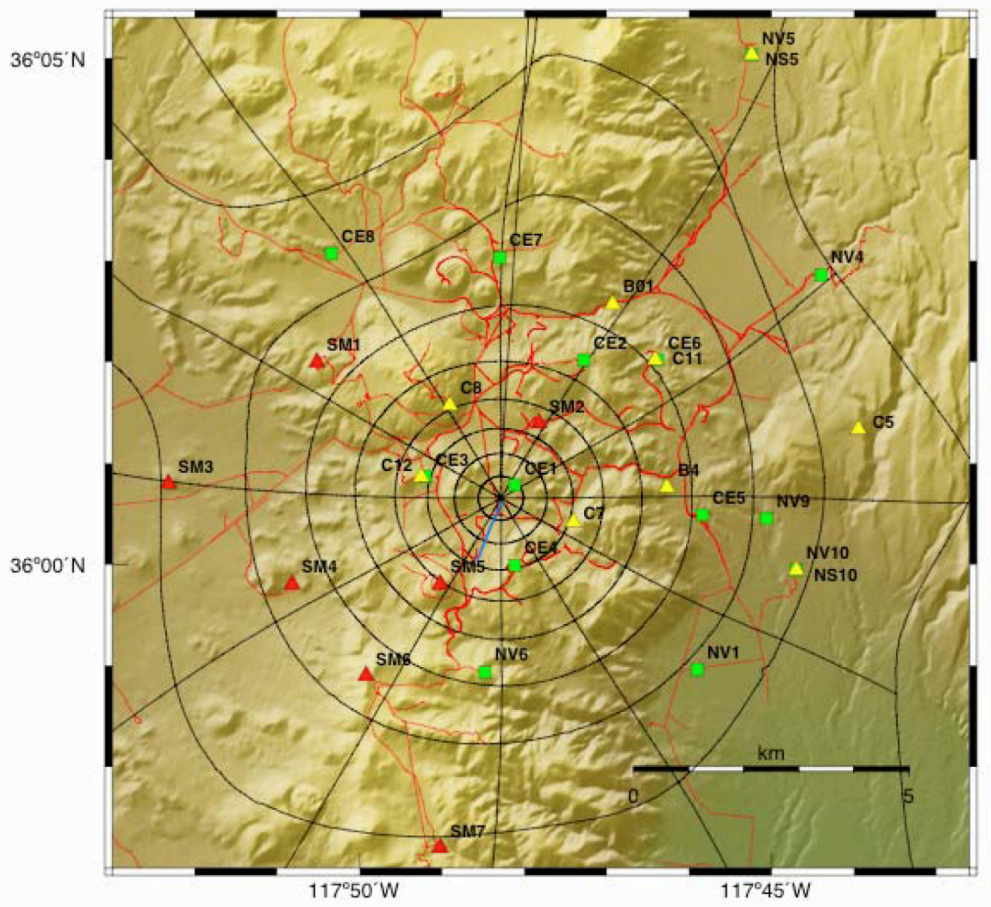

Figure 17: Layout for additional temporary seismometers to monitor earthquakes near well 46A-19RD (blue), expected to be stimulated by injection in 2009. The plan was guided by ray tracing through a three-dimensional crustal model. Red lines: roads. Green squares: permanent seismometers. Yellow triangles: temporary seismometers retained from the earlier deployment centered on the East Flank. Red triangles: re-deployed portable seismometers. Black lines: Projection of upper focal hemisphere onto the Earth's surface for earthquakes near the bottom of well 46A-19RD. Quasi-circular lines are spaced at 10° in "take-off angle", measured from nadir, and radial lines are spaced at 30° in azimuth.

3.5.4 The EGS experiment in well 34A-9, August 2004

3.5.4.1 Details of the well and the stimulation

Well 34A-9 was originally drilled to a depth of 2,956 m (9,700') in 1993, and temperatures exceeding 300˚C were encountered – amongst the highest ever recorded in the Coso area. The permeability of the formations drilled was poor, however. Steam condensate was injected into the well, which improved permeability.

Initially, the well could only accept 2.5 l/s (40 gpm) at a well-head pressure of 0.62 MPa (90 psi), but after a two-week injection period it accepted 50 l/s (800 gpm) under "vacuum" (i.e., atmospheric pressure). Seismicity accompanied this injection [*Rose et al.*, 2005] but in 1993 the seismic network was in an embryonic state and details of the seismicity are not readily extractable. The well was subsequently used successfully as an injector until 2004, when a leak developed at the top of the shallow casing, causing most of the injectate to flow into the shallow reservoir instead of deeper levels. As a result the well was shut in 12th January 2004.

The shallow casing was repaired 10th June - 24th July 2004, and stimulation was conducted in August 2004 to bring 34A-9 back into service as an injector. The objective was to achieve 45 l/s (~ 750 gpm) under a wellhead pressure of no more than 0.7 MPa (100 psi). In August 2004, the groundwater level in the well stood at 923 m (3000'), so filling the wellbore with water corresponded to increasing downhole pressure by 9.1 MPa (1300 psi).

After ~240 m^3 (1500 bbl) of steam condensate had been injected at a rate of 2.5 l/s (taking ~ 1 day), the wellhead pressure had dropped to atmospheric. The injection rate was then increased to 28 l/s (450 g/m) and maintained at that rate for one day. The wellhead pressure remained at atmospheric. Finally, the injection rate was raised to 50 l/s (800 gpm) and maintained at this level for eight days, during which time the wellhead pressure remained at atmospheric. The total volume injected for the entire stimulation was 12,700 m^3 (80,000 bbl).

Details of the injection and associated monitoring are shown in Figure 18. The objective of achieving an injection rate of 45 l/s (~ 750 gpm) under a wellhead pressure no more than 0.7 MPa (100 psi) was achieved by a large margin. At the end of the stimulation, 34A-9 would accept 126 l/s of hot, separated brine under a wellhead pressure of 0.41 MPa (60 psi).

3.5.4.2 The tracer test in well 34A-9

In order to determine the destination of fluids injected into the newly stimulated 34A-9, a tracer test was performed 1st September, 2004. A pulse comprising 100 kg of 1,3,6-naphthalene trisulfonate was injected. The wells on pad 38, immediately to the south, were then sampled and analyzed for the tracer. The return curves (Figure 19) show a strong return from well 38-9 and a slower, building return from 38A-9. Analysis of the shape of the tracer return curve [*Shook and Forsman*, 2005] suggested that the fraction of tracer returned to 38A-9 and the tracer-swept pore volume were 35% and 41,000 m^3, respectively [*Rose et al.*, 2006].

3.5.4.3 Analysis of the induced seismicity

3.5.4.3.1 Earthquake time series and magnitudes

Histograms showing the numbers of earthquakes that occurred day by day for the 5 months surrounding the injection in 34A-9 are shown in Figures 20a-e. Only earthquakes whose epicenters lie within a horizontal distance of 1 km from the base of well 34A-9 are included. This spatial restriction eliminated earthquakes from a cluster to the SSW that was associated with injection in well 64A-16 (David Meade, U.S. Navy, personal communication).

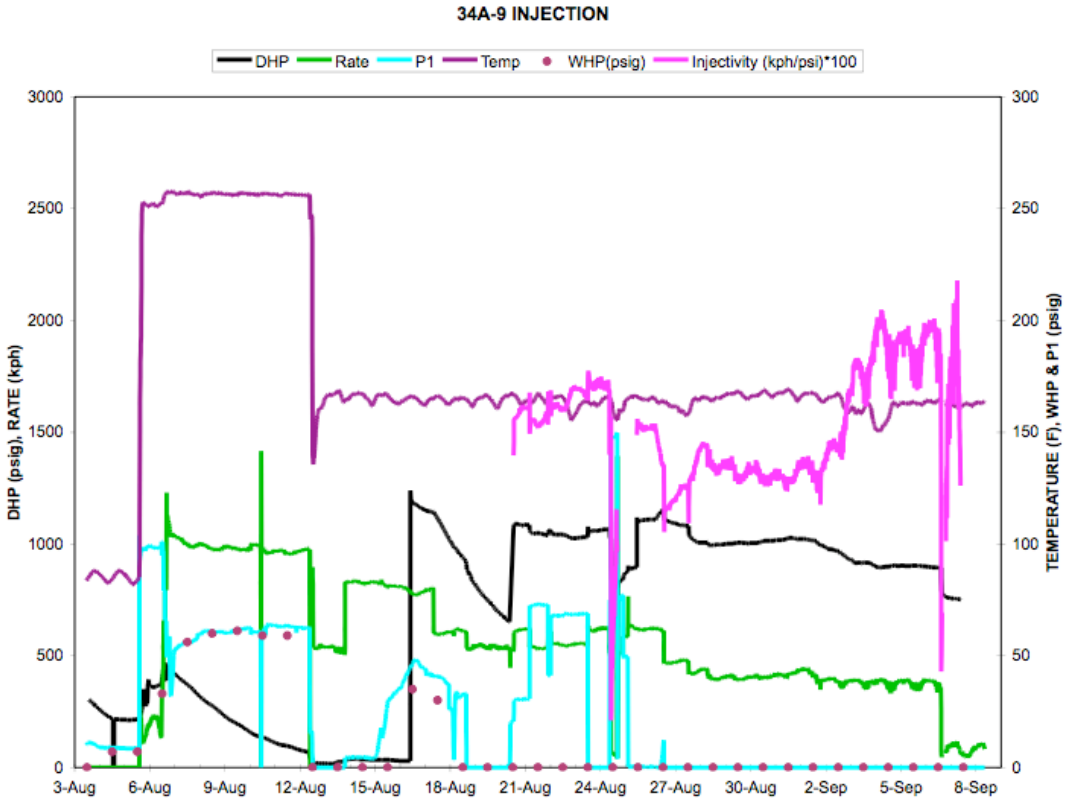

Figure 18: Injection data for August – September 2004, well 34A-9. DHP = downhole pressure, Rate = injection flow rate, P1 = pressure in feed line, Temp = temperature of injectate, WHP = wellhead pressure. (Figure courtesy of Peter Rose)

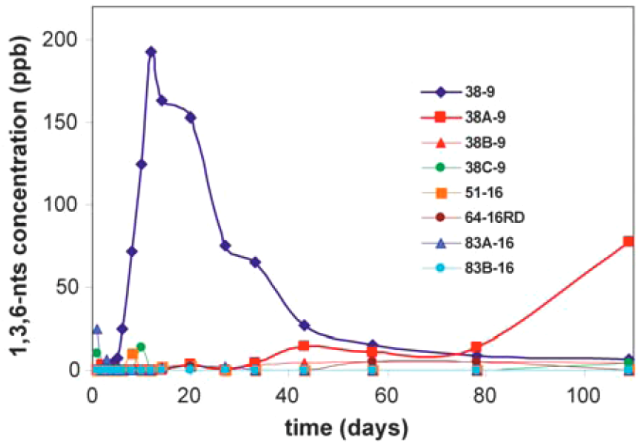

Figure 19: Returns of tracer injected into well 34A-9 from production wells on the Coso East Flank [from *Rose et al.*, 2006].

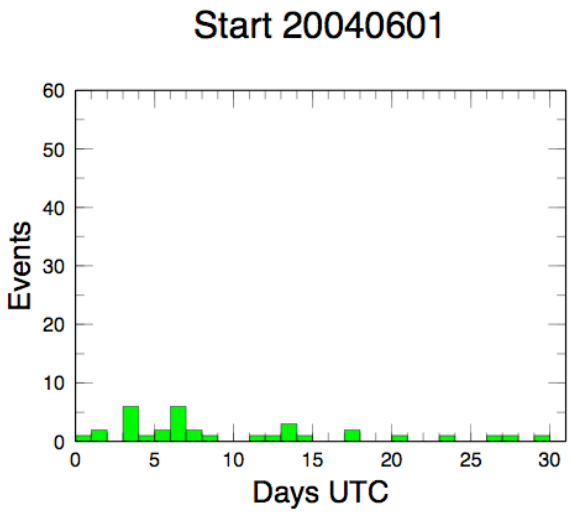

Figure 20a. Histogram showing number of earthquakes per day, for June 2004. Only earthquakes whose epicenters lie within a horizontal distance of 1 km from the surface projection of the base of well 34A-9 are included.

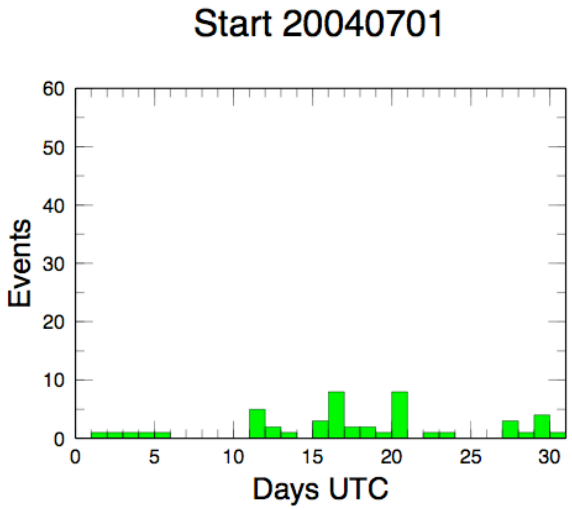

Figure 20b. Same as Figure 20a except for July 2004.

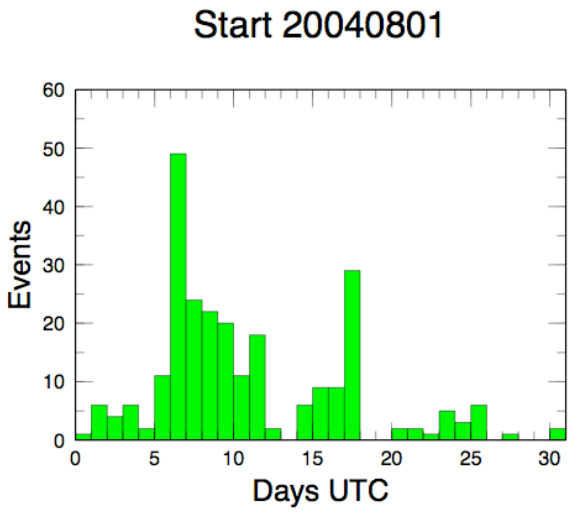

Figure 20c. Same as Figure 20a except for August 2004.

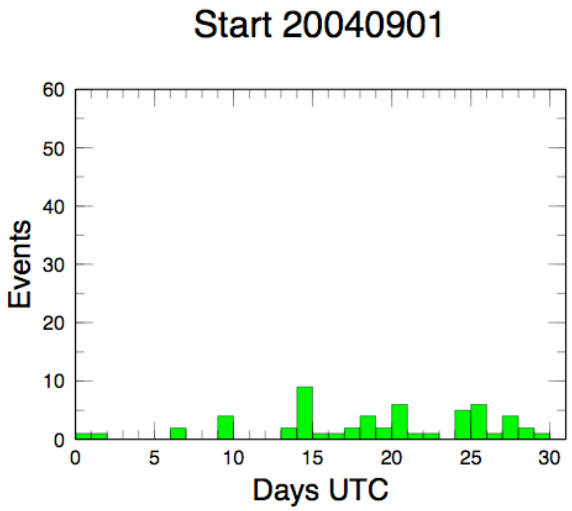

Figure 20d. Same as Figure 20a except for September 2004.

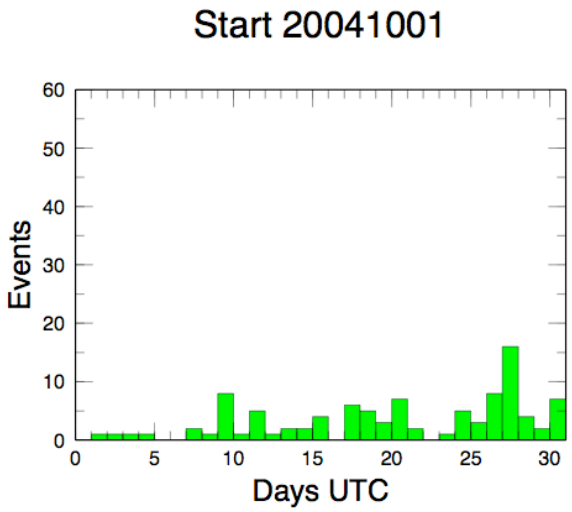

Figure 20e. Same as Figure 20a except for October 2004.

It is clear from Figures 20a-e that the level of activity was low in the two months preceding and the two following the August injection. During these months, only occasionally did the number of earthquakes/day exceed 5. During August, however, seismic activity is dominated by an intense burst associated with the 6th - 13th injection.

The earthquake activity of interest was thus divided into the following periods for analysis:

1. 20040601 0000 00 - 20040806 2112 00 – the pre-injection period
2. 20040806 2112 00 - 20040813 2210 00 – the co-injection period
3. 20040813 2210 00 – 20041101 0000 00 – the post-injection period

A second, subsidiary burst of activity occurred in association with the 15th – 18th resurgence of injection. These earthquakes have been included in the post-injection set.

Magnitudes of earthquakes for the entire period are shown in Figure 21, and for August only in Figure 22. Clearly the most intense activity was associated with the period 6th - 18th August, during the injection when the injection rate and wellhead pressures were highest (Figure 18). For the period 6th - 13th the seismic rate is high but magnitudes are not particularly unusually large. For the 2nd period of increased injection rate and wellhead pressure, 14th - 18th August, the high seismic rate is accompanied by larger magnitude, with the largest event having a U.S. Navy catalog magnitude of M 2.5.

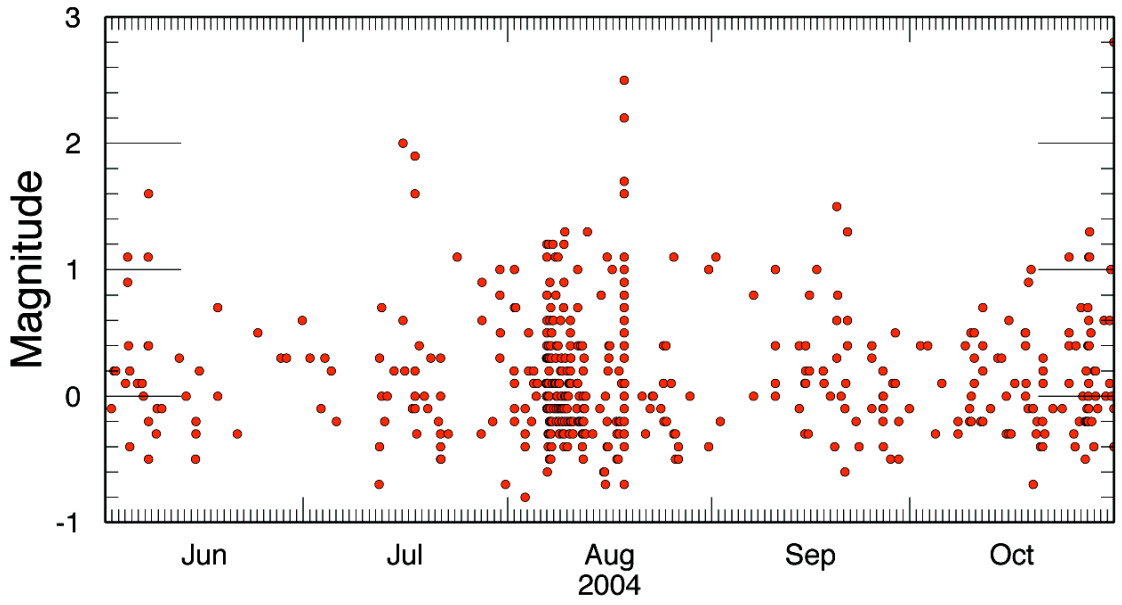

Figure 21: Magnitudes of earthquakes within 1 km of the bottom of well 34A-9 for the period June - October, 2004.

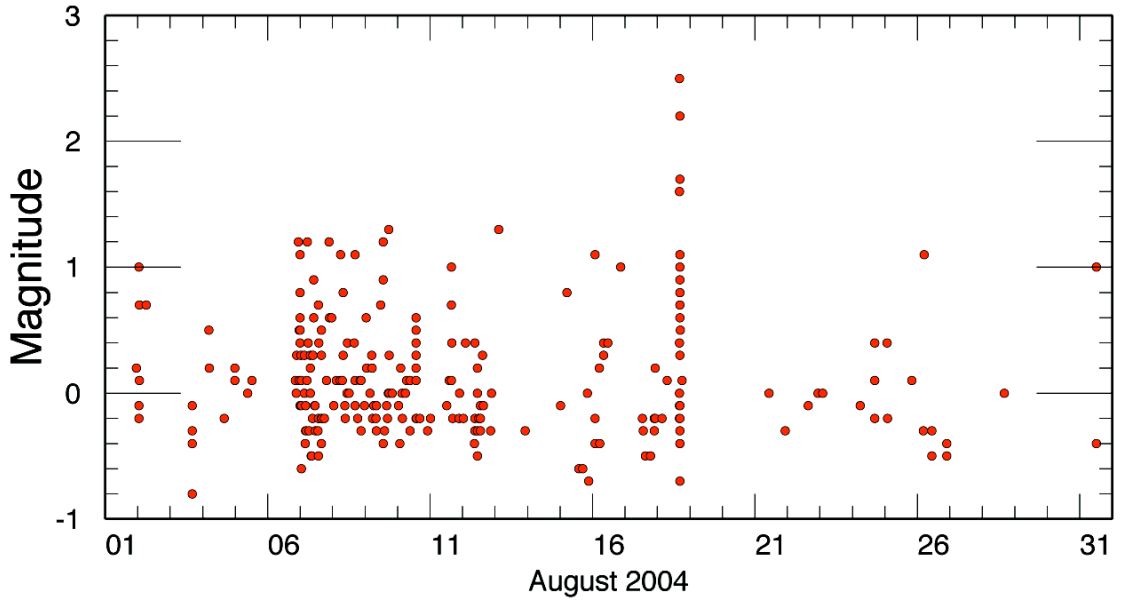

Figure 22: Same as Figure 21 but for August 2004 only.

Data from the 14-station portable network were only available for the latter part of July and most of August, namely, the time period 20040716 1607 – 20040824 2150. The quality of the results for this period is thus enhanced compared with other times, though the data quality is excellent, both for locations and moment tensors, for the entire 5-month period studied.

3.5.4.3.2 Earthquake locations

Three families of earthquake locations were assembled for study:

1. hypocenters calculated by the U.S. Navy, using hand-picked P- and S-wave arrival times, available from the U.S. Navy earthquake catalog, and a 1-D crustal model;
2. enhanced hypocenters calculated using the arrival time picks from the U.S. Navy catalog, located using the relative-relocation program **hypocc**, and;
3. still further enhanced hypocenters calculated by re-picking the P- and S-wave arrival times using the waveform cross-correlation program **toonpics** (developed as part of this project) and locating using **hypocc**.

Epicentral maps of the U.S. Navy catalog locations for the entire field for the months June – October 2004 are shown in Figures 23a-e. Selected wells are shown as blue lines. A dense cluster of seismicity may be observed near well 34A-9 for the month of August. Activity was much lower during June/July and September/October. A second region where activity is typically intense lies ~ 1 km SSW of well 34A-9. This activity is though to have been induced by injection in well 64A-16 (David Meade, U.S. Navy, personal communication). Details of the U.S. Navy epicenters, and those calculated using **hypocc**, for the co-injection period only, are shown on a larger scale in Figure 24.

Program **hypocc** had been little used before application to these injection data, and significant effort was expended in exploring its behavior using various input parameters and inversion choices. A suite of program scripts was developed in order to automate inversions. This work will be useful for future application to injection experiments in near-real time.

The best results for the pre-, co- and post-injection periods are displayed in Figures 25a-c. For all three time periods, the U.S. Navy catalog locations form diffuse, quasi-circular clouds and there is little indication of clustering or alignment in the NNE-orientated local tectonic trend (left panels). Substantial improvement in clustering was achieved using **hypocc** and the U.S. Navy arrival time picks (middle panels). This is most clearly seen in the pre- and co-injection datasets, which show clear NNE-trending elongation. The cross section for the co-injection dataset (lower middle panel, Figure 25b) shows clearly that the earthquakes occurred on a fault dipping steeply to the E.

The results from refining the arrival time picks using **toonpics** prior to application of **hypocc** produced further substantial improvement. The pre-injection earthquakes are mostly clustered densely in a region beneath the producing well 38-9, suggesting that they were related to production from that well (top right panel, Figure 25a). The earthquakes are widely distributed in depth (bottom right panel, Figure 25a). This diffuse distribution is likely real since the earthquakes were located in the same way as the co-injection events, that were found to be much more clustered.

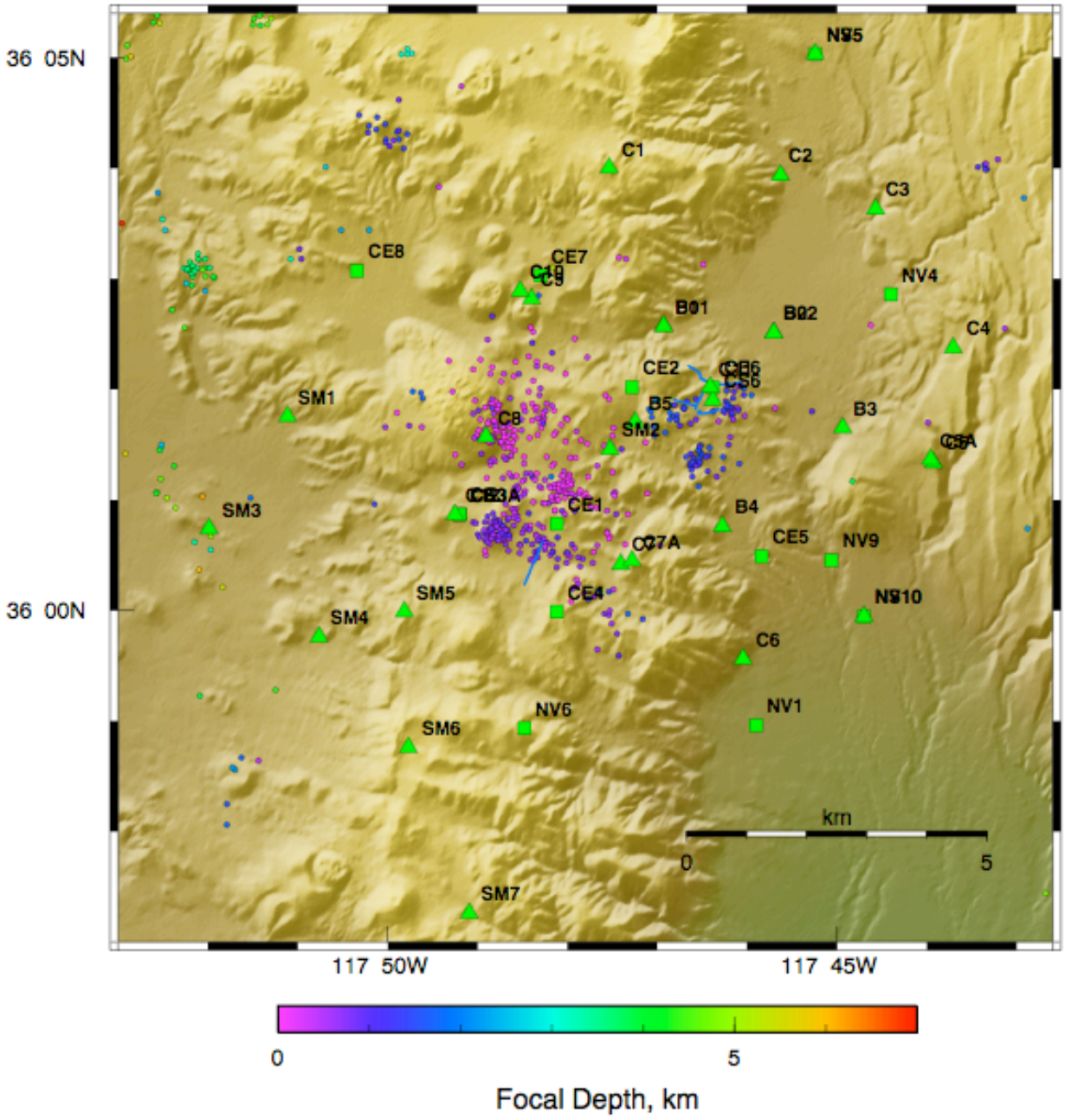

Figure 23a. Epicentral map of U.S. Navy earthquake locations for the Coso field for June 2004. Wells 34A-9, 34-9RD2, 38-9, 38A-9, 38C-9 and 46A-19RD (near station CE1) are shown as blue lines.

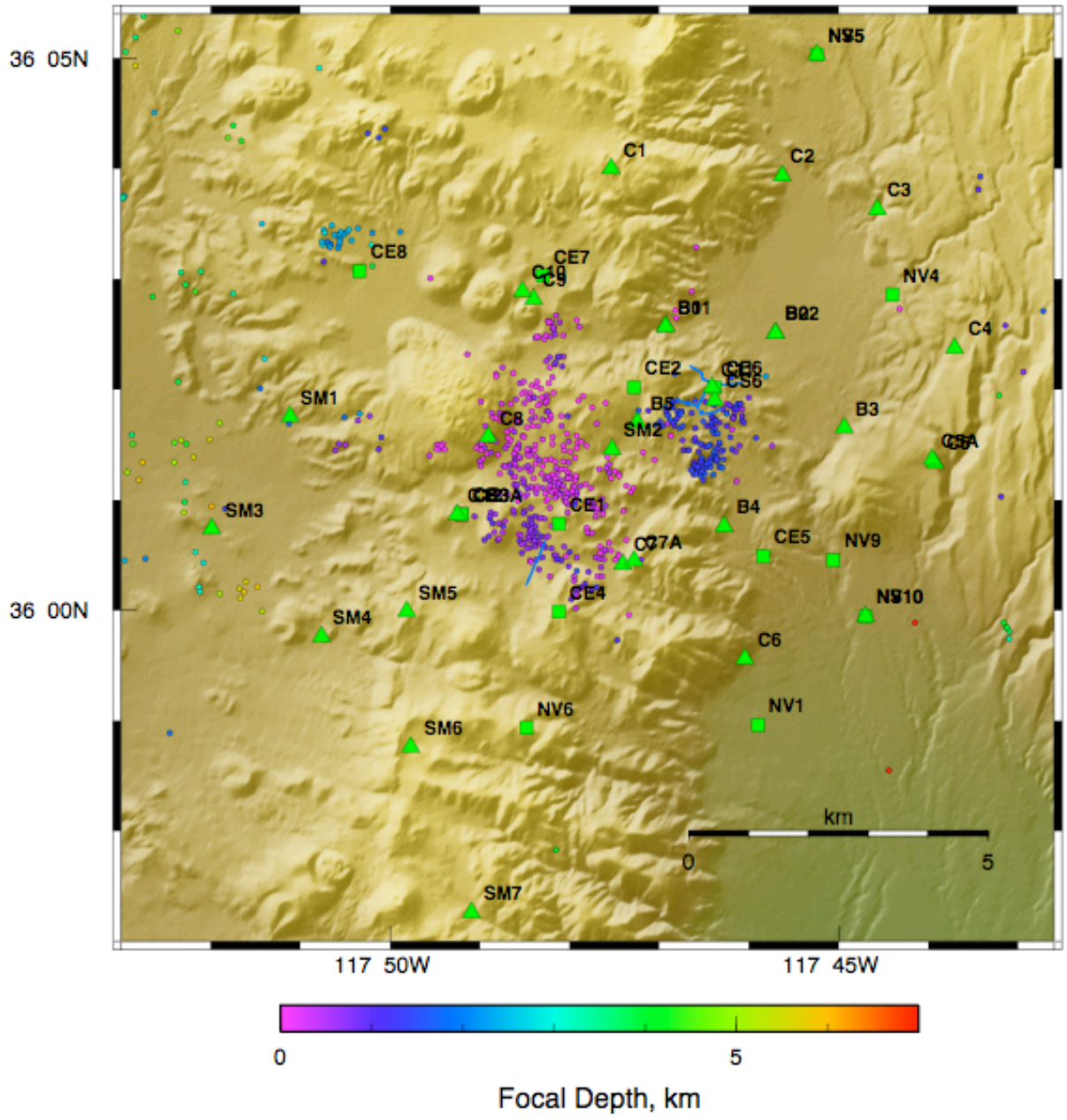

Figure 23b. As for Figure 23a except for July 2004.

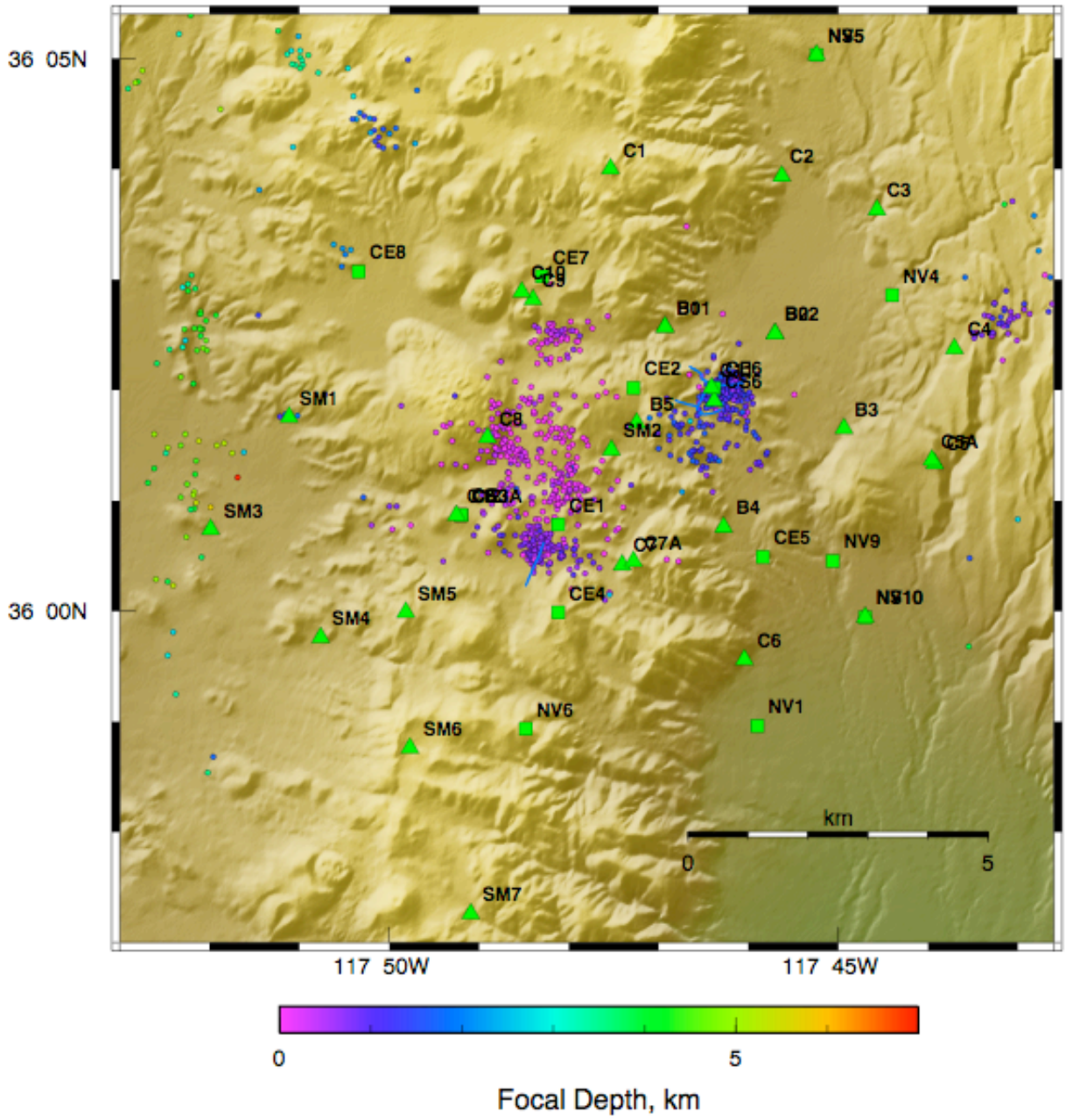

Figure 23c. As for Figure 23a except for August 2004.

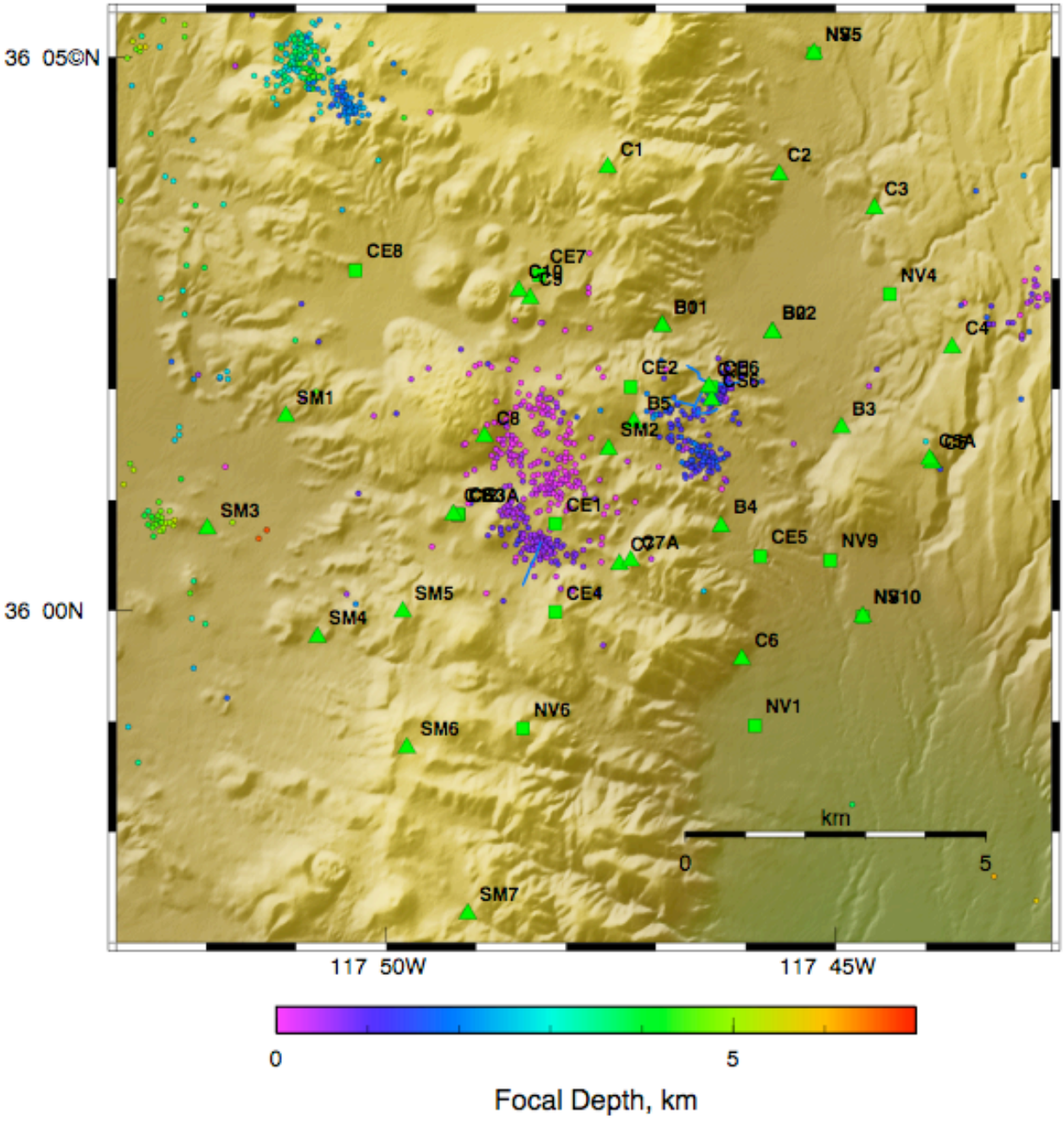

Figure 23d. As for Figure 23a except for September 2004.

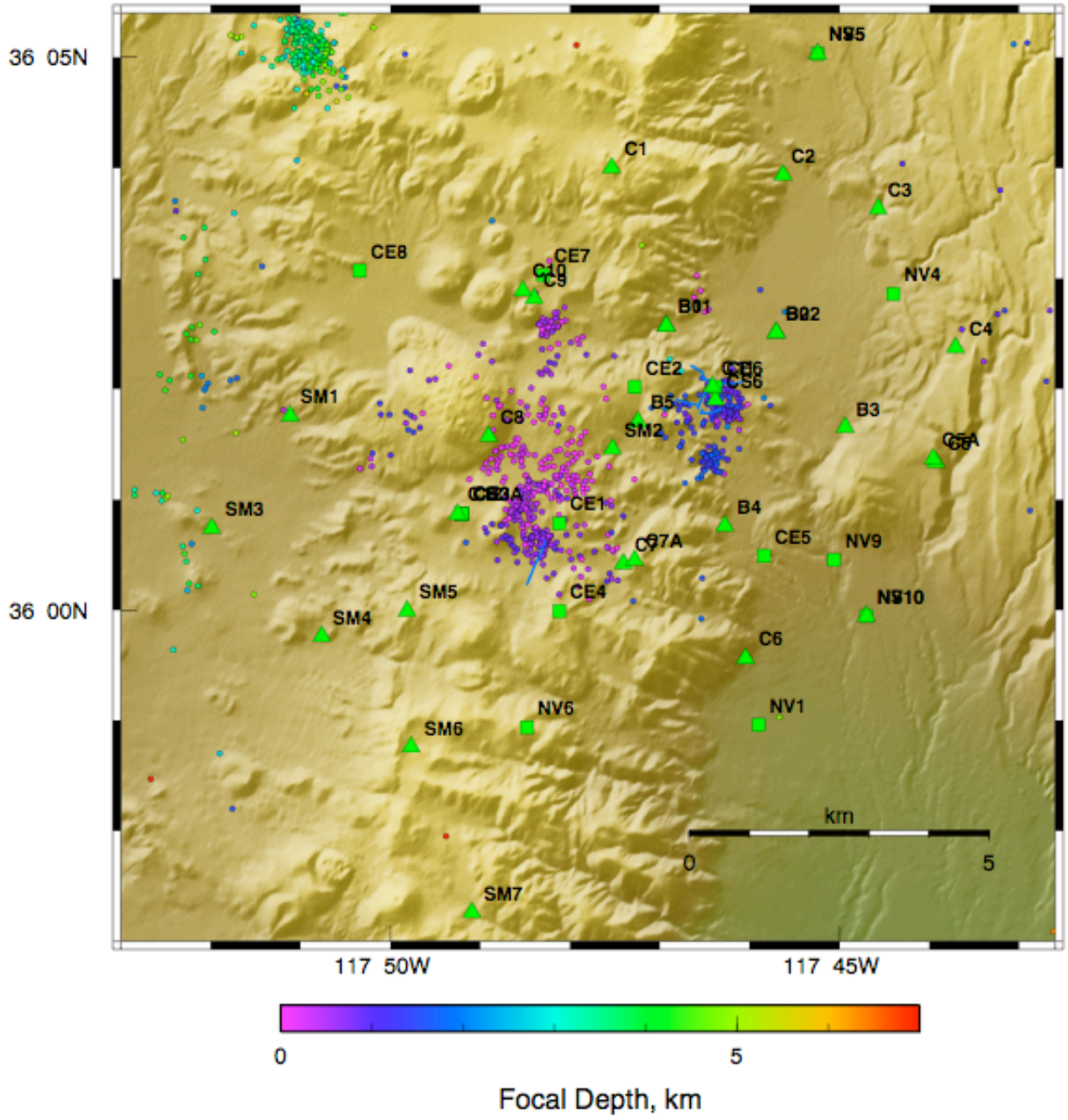

Figure 23e. As for Figure 23a except for October 2004.

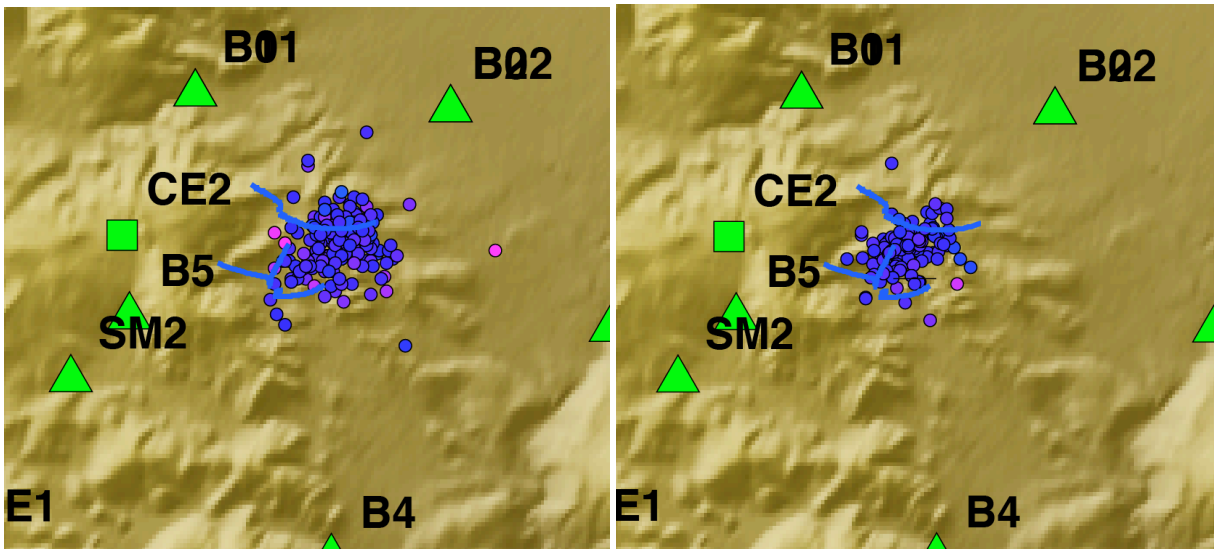

Navy **hypocc**

Figure 24: Maps of co-injection epicenters only, left: from the U.S. Navy catalog, right: from **hypocc**.

The co-injection earthquakes located using **toonpics** combined with **hypocc** are shown in the right panels of Figure 25b. The planar structure revealed by applying **hypocc** to the U.S. Navy picks is imaged in enhanced focus. It suggests that the earthquakes occurred on a planar fault which may be accurately measured to strike at ~ N 35˚ E and dip at ~ 83˚ to the E.

The post-injection earthquakes, shown in Figure 25c, contrast strikingly with the co-injection earthquakes in showing a much more diffuse distribution. The scatter seen in the U.S. Navy catalog locations (left panels, Figure 25c) is reduced by application of **hypocc** (middle panels, Figure 25c), but this is little reduced further through application of **toonpics** prior to **hypocc** (right panels, Figure 25c). That result reveals an elongated distribution that is nevertheless much more diffuse than that associated with the co-injection earthquakes. They likely occurred as stress built up in the volume surrounding the fault activated by injection was progressively released during the subsequent weeks.

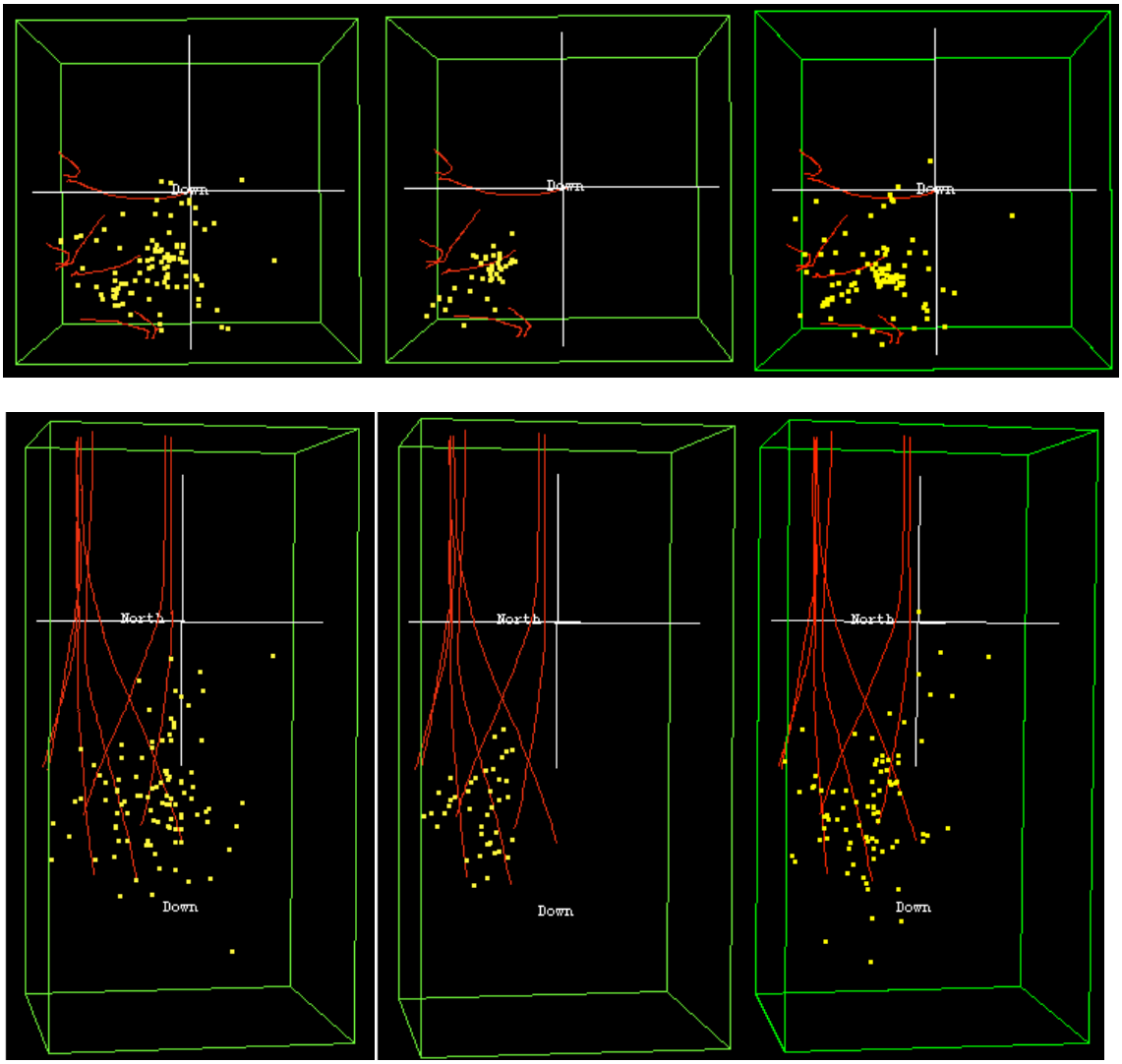

U.S. Navy **hypocc** **toonpics + hypocc**

Figure 25a. Pre-injection period. Locations are displayed as screenshots of rotatable 3D plots. Top row: Horizontal maps, bottom row: Vertical cross sections rotated so the line of sight is NNE, i.e. aligned along the tectonic strike of local faults. Red lines indicate wells 34A-9, 34-9RD2, 38A-9, 38C-9, 38B-9, 38-9, 51-16 and 51A-16. Left panels: U.S. Navy catalog locations, middle panels: **hypocc** locations, right panels: **hypocc+toonpics** locations.

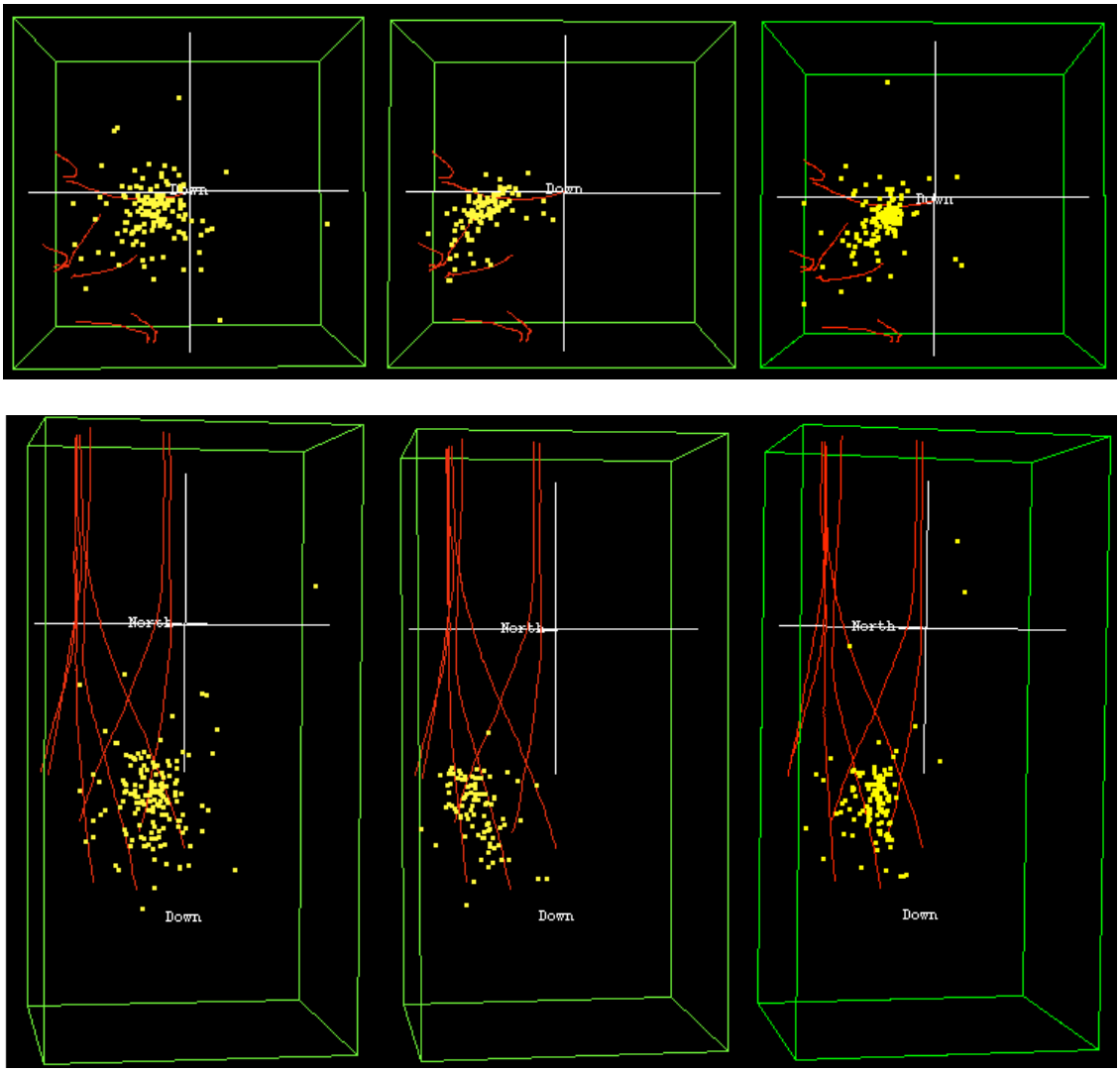

U.S. Navy **hypocc** **toonpics + hypocc**

Figure 25b. As for Figure 25a but for co-injection period.

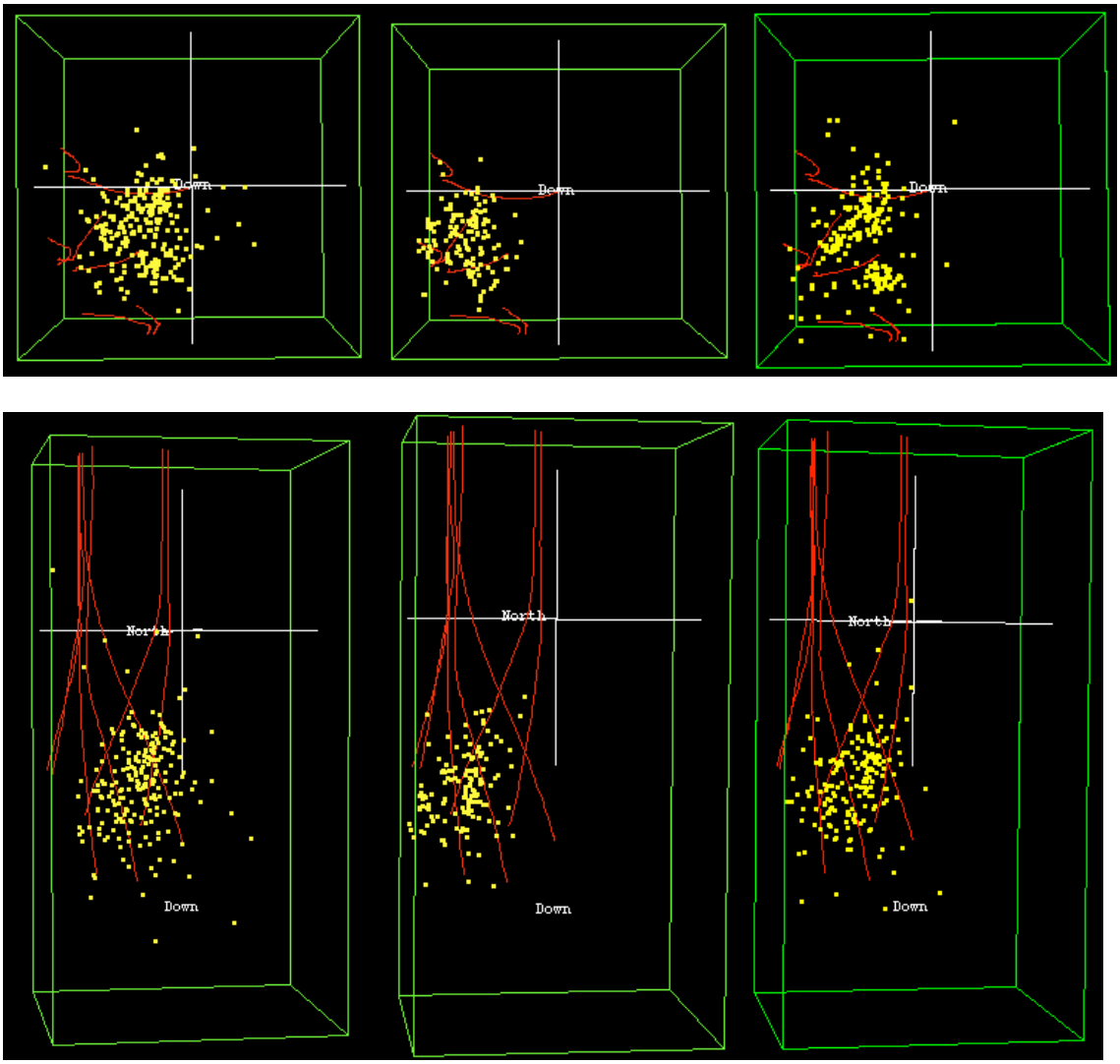

U.S. Navy **hypocc** **toonpics + hypocc**

Figure 25c. As for Figure 25a but for post-injection period.

3.5.4.3.3 *Chronological distribution of the co-injection earthquakes*

In order to determine the geometry of rupture, event occurrence time is plotted vs. northing, easting and depth in Figure 26: The period displayed is 6th - 19th August 2004, which covers both the main co-injection swarm, and the subsidiary swam that was induced by the increased injection rate 14th - 18th August. Figure 26 shows that during the first 24-36 hrs there was a tendency for the earthquake activity to migrate north, west and up. Thereafter, the earthquakes were scattered throughout the activated structure and displayed little consistent systematic

behavior. Most hypocenters lay in the depth range ~ 0.8 - 1.6 km bsl (~ 2.11 - 2.91 km (~ 6,860 - 9,450') below the surface). This may be compared with the depths of the bottoms of nearby wells of:

1. well 34A-9 2.8 km below surface (9,218')
2. well 38A-9 2.9 km below surface (9,407')
3. well 38-9 3.0 km below surface (9,842')

The range in epicentral locations and hypocentral depths suggests that the activated plane was ~ 0.5 km (0.3 mi) in along-strike length and ~ 0.8 km (2,600') in down-dip width.

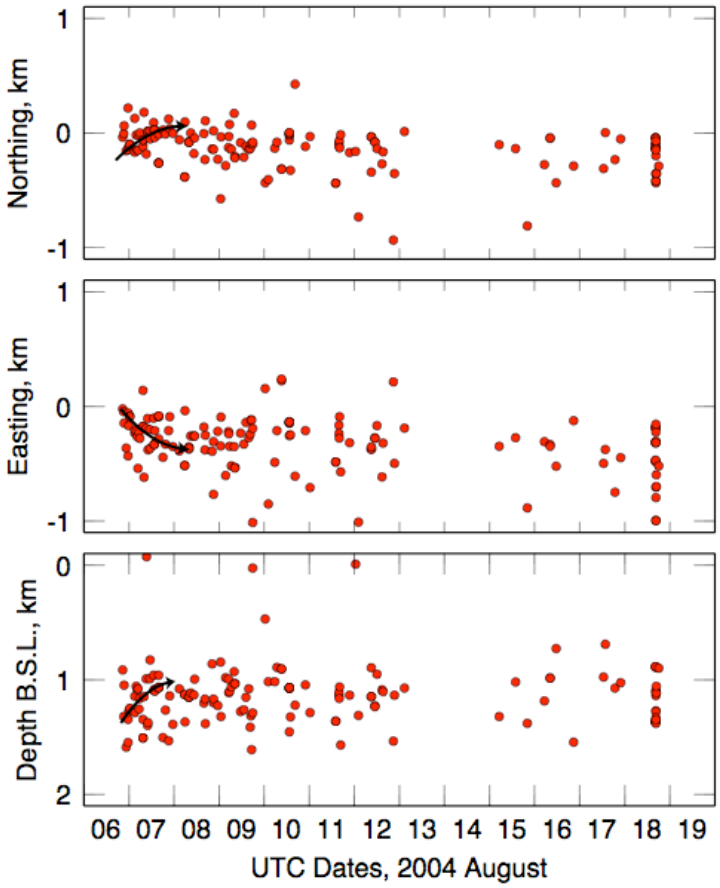

Figure 26: Time of occurrence of co-injection earthquakes vs. northing, easting and depth. Black arrows indicate initial migrations of the most intense activity, following which systematic migrations are not observed.

3.5.4.3.4 *Moment tensors*

Moment tensors were calculated for a large suite of earthquakes spanning the pre-, co- and post-injection periods. All earthquakes for which the magnitude given in the U.S. Navy catalog was

M 0.5 or higher were studied. Fairly good results were typically obtainable for all earthquakes that were listed as having 10 or more P-wave picks in the U.S. Navy catalog. In practice this meant that well-constrained moment tensors could be obtained for the majority of earthquakes with magnitudes of M 0.5 or larger (Table 2). Details of the results are given in Appendix 5.

Table 2. Numbers of moment tensors derived for the pre-, co- and post-injection periods.

Time period	**# of moment tensors**
June:	6
July:	7
August:	40
September:	8
October:	14
Pre-injection:	17
Co-injection:	26
Post-injection:	32
total:	**75**

The largest earthquake for which a good moment tensor could be derived had a magnitude of M 2.8. Three earthquakes had magnitudes M > 2.0 and 32 had magnitudes in the range M 1.0 – 1.9.

The entire set of results are displayed in Figures 27a-c in two forms:

1. *The source-type plot* – this shows the volumetric (V), double couple (DC) and compensated linear vector dipole (CLVD) components of the moment tensors. The point at which each event plots on the diagram is independent of the orientation of the fracture formed, thus the term "source type". Earthquakes that plot in the center of the plot (the 'DC' point) have moment tensors consistent with shear motion on a planar fault. Earthquakes that plot above the center line have explosive components and those that plot below have implosive components.
2. *The source-orientation plot* – equal-area plots of tension (T), intermediate (I) and pressure (P) axes. These axes give a qualitative indication of the orientations of the greatest (σ_1), intermediate (σ_2) and least (σ_3) principal stresses to which each earthquake responded at its time of occurrence.

Some examples of individual solutions are shown in Appendix 5 as **eqmec** screenshots.

The reliability of the moment tensors calculated was studied using the new error-assessment technique developed under Subtask 1.3, described above. The best-fit mechanism and 15 extremal mechanisms were calculated for a candidate earthquake from July 2004 (Figure 28) and two earthquakes from August 2004 (Figures 29 and 30). The results indicate that the suite of good-fit mechanisms for typical well-constrained earthquakes is of the order of ± 0.1 units on the plot in the volumetric component and ± 0.2 units on the plot in the ±CLVD component, as depicted on the source-type plots in this report. [This corresponds to ± 0.1 in the parameter *k*, which varies from +1 at the top of the plot to -1 at the bottom, and ± 1 in ε, which varies from -0.5 at the +CLVD point to +0.5 at the -CLVD point; *Julian et al.*, 1998].

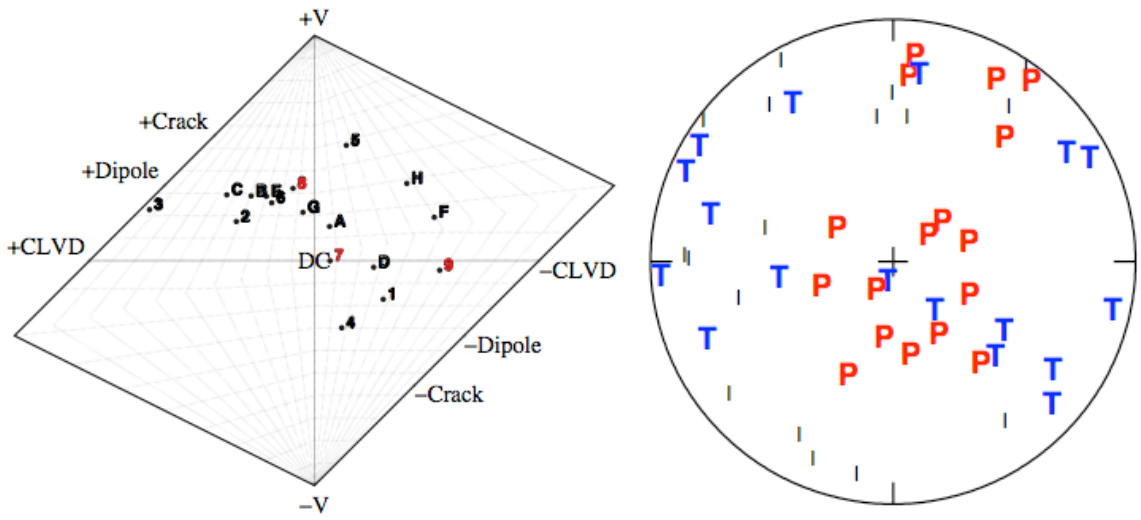

Figure 27a. Moment tensor results for the pre-injection period. Left: Source-type plot for the 17 moment tensors calculated. The earthquakes are labeled 1-9 and then A-Z to denote their time order. The largest earthquakes are indicated in red (M 2.0 – 1.6). Right: Equal-area plot of pressure (P), intermediate (I) and tension (T) axes for the same moment-tensor data set.

For most of the sets of earthquakes analyzed, the array of moment tensor results form a zone elongated in a similar way to, but with more variation than, the suites of near-optimum solutions shown in Figures 28 - 30. In the moment tensor results, there is typically variation of up to ± 0.3 plot units in the ±V component and ± 0.8 plot units in the ±CLVD component. This suggests that some, but not all of the ranges in the results is due to error. Importantly, it places confidence that the non-zero volumetric components are real and not merely a result of observational error.

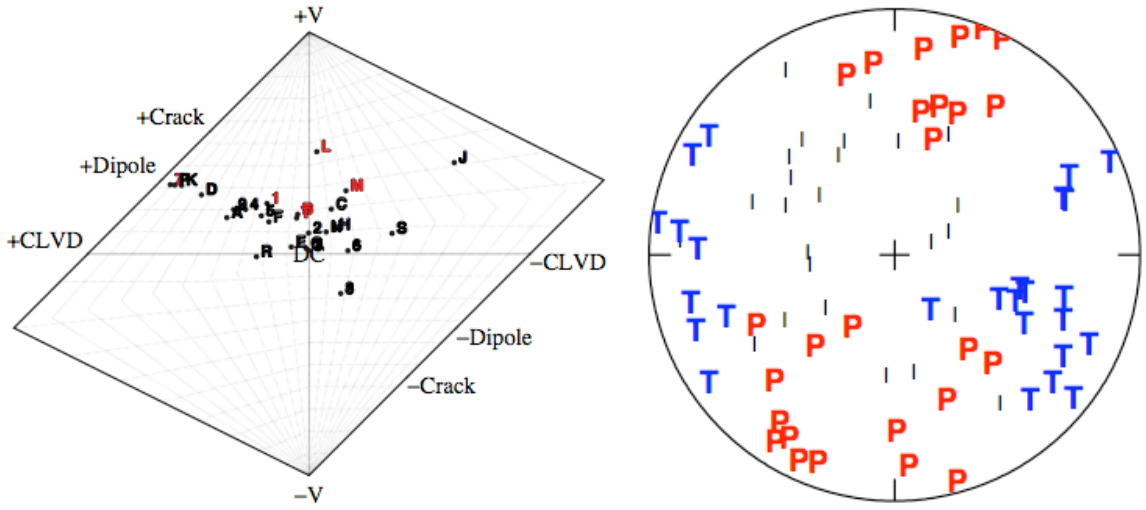

Figure 27b. Same as Figure 27a but for the 26 moment tensors calculated for the co-injection period. Earthquakes denoted in red in plot at left had magnitudes of M 1.3 – 1.2.

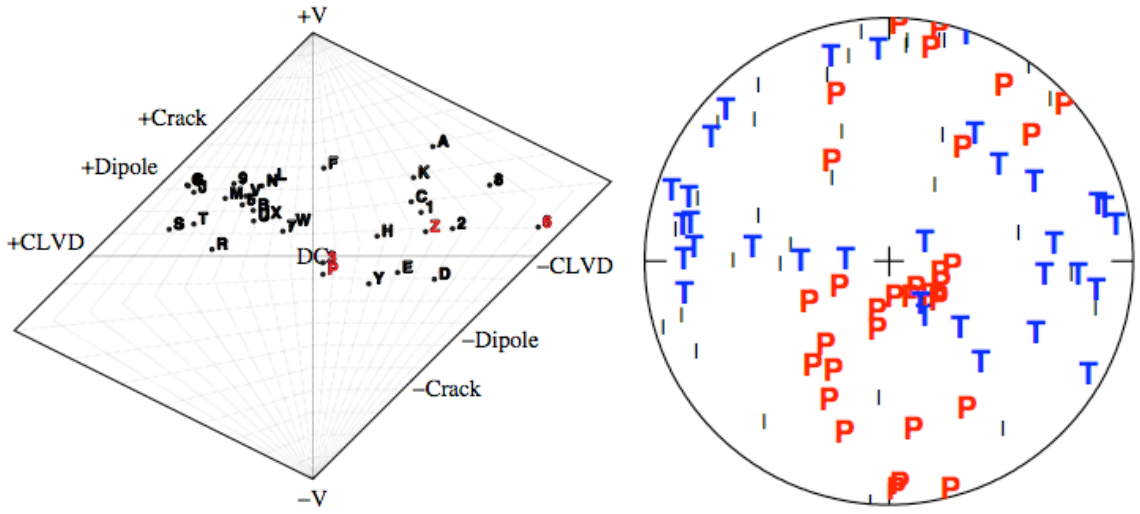

Figure 27c. Same as Figure 27a but for the 32 moment tensors calculated for the post-injection period. Earthquakes denoted in red in plot at left had magnitudes of M = 2.8 – 1.6.

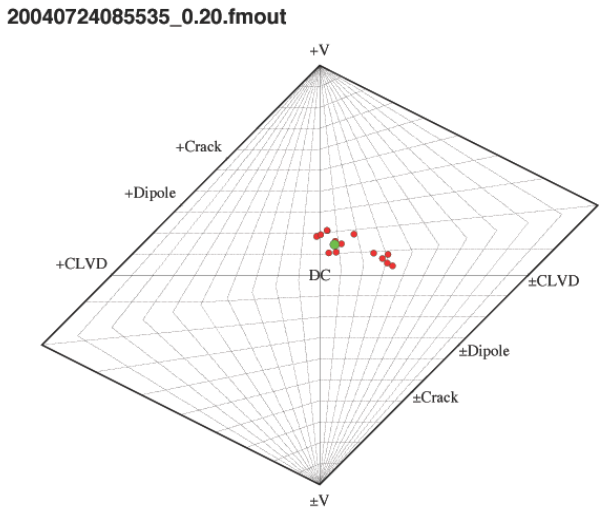

Figure 28: Source-type plot [*Hudson et al.*, 1989] for a single earthquake from the Coso geothermal area, showing the best-fit source mechanism (green) and 15 extremal mechanisms (red) obtained by maximizing specified linear combinations of the moment-tensor components while keeping the L1 norm of the data residuals below a given limit. The example used is the pre-injection earthquake of 20040724 0855. Details of the best mechanism are shown in Appendix 5, Figure A5a.

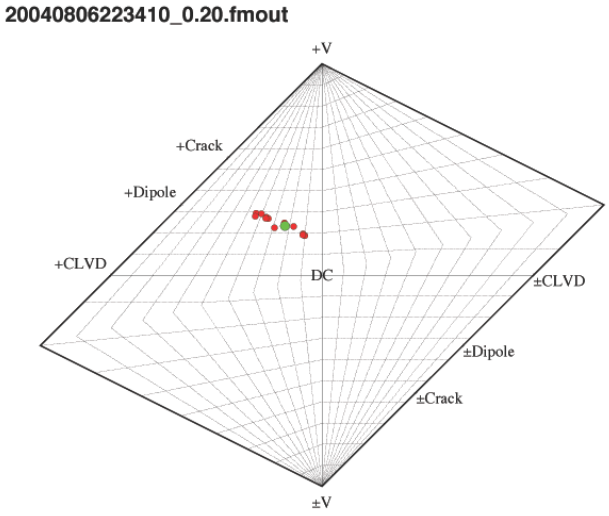

Figure 29: As Figure 28 except for the for the co-injection earthquake of 20040806 2234. Details of the best mechanism are shown in Appendix 5, Figure A5b.

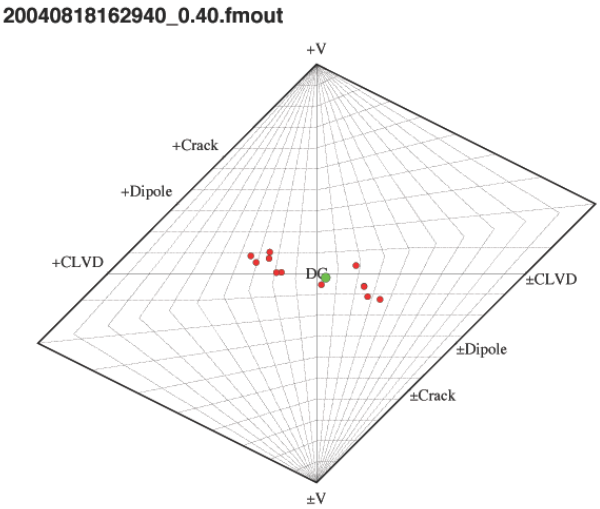

Figure 30: As Figure 28 except for the post-injection earthquake of 20040818 1629. Details of the best mechanism are shown in Appendix 5, Figure A5c.

The following features may be highlighted:

1. The source types for the earthquakes studied vary from double couple (consistent with shear motion on a planar fault) to having significant crack-opening components. Very few earthquakes have implosive source types, and in view of the uncertainty revealed to be inherent in the results, the implosive components are probably not statistically significant.
2. The pre-, co-, and post-injection earthquakes are all distributed in a broadly similar way in source-type space. The injection experiment does not seem to have induced earthquakes that had radically different volumetric components from the background earthquakes unassociated with injection. Nevertheless, if only the largest-magnitude earthquakes are considered (plotted in red in Figures 27a-c, left panels), there is a clear tendency for the co-injection events to have systematically larger volume increase (crack-opening) components than the pre- and post-injection data sets (compare left panel of Figure 27b with left panels of Figures 27a and 27c).
3. The source-orientation plots (right panels of Figures 27a-c) show clear variation between the pre-, co- and post-injection earthquake sets. The P-axes of the pre-injection earthquakes tend to be subvertical, and the T-axes are preferentially orientated WNW-ESE, consistent with the general tectonics of the Coso geothermal area (Figure 27a). The general orientation of the P-axes of the co-injection earthquakes is very different. They are preferentially orientated SSW and NNE. There is a particularly notable absence of high-angle P axes in the region of the plot most heavily populated by pre-injection earthquakes (compare Figures 27a and 27b, left panels). The post-injection P- and T-axes have orientations that are a mix of the pre- and co-injection ones, with many earthquakes having high P-axis angles and a few with SSE orientations.

The systematic variations in P- and T-axis orientations indicates that the co-injection earthquakes occurred in response to a stress field with a different orientation from that which controlled the pre-injection earthquakes. The pre-injection stress field tended to encourage normal-faulting earthquakes with moderate crack-opening components. The co-injection stress field tended to encourage earthquakes with larger strike-slip and crack-opening components. The results suggest that the least principal stress (σ_3) was orientated ESE. Prior to the injection the greatest principal stress (σ_1) was vertical. Injection increased the SSW-orientated intermediate principal stress (σ_2) so it exceeded the vertical principal stress, and the absolute magnitudes of stress were reduced in general. This is illustrated schematically in Figure 31.

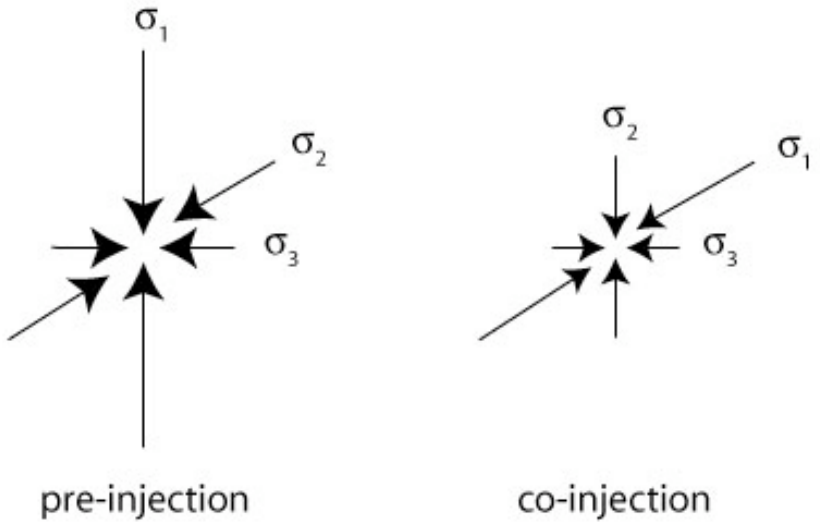

Figure 31: Effect of injection on the absolute and relative magnitudes of principal stresses in the vicinity of well 34A-9.

In order to investigate the longevity of the stress modulation induced by injection, separate source-orientation plots for the months of September and October were made (Figure 32). For both months, some earthquakes have southerly-trending, sub-horizontal P-axes. This suggests that modulation of the stress field orientation lasted for at least 2 months after the injection. On the other hand, the distribution of source types for the post-injection data set is indistinguishable from that of the pre-injection earthquakes. This suggests that modulation of the absolute stress levels decayed rapidly after the main injection.

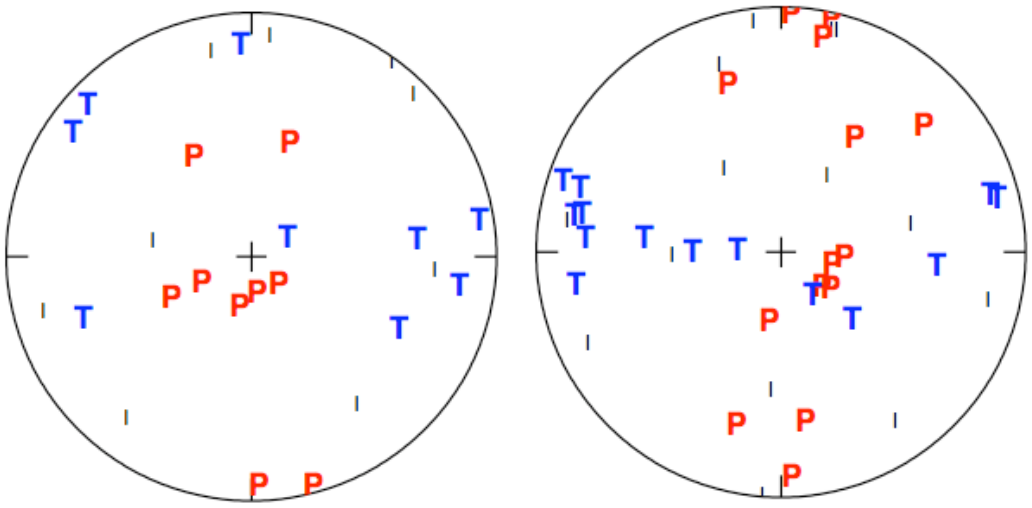

Figure 32: Equal-area plots of pressure (P), intermediate (I) and tension (T) axes of earthquakes for September (left) and October (right).

3.5.4.3.5 *Joint interpretation with other results*

The independent studies most relevant to understanding and interpreting the results of the earthquake analysis are:

1. local geological mapping;
2. hydraulic fracturing tests to obtain stress axis directions and magnitudes;
3. borehole logging, especially for fracture identification;
4. injection monitoring, including the downhole pressure, injection flow rate, pressure, temperature of injectate and wellhead pressure during the EGS experiment;
5. monitoring the fate of injected fluids using tracer testing.

The main results from the earthquake analysis may be summarized as follows:

1. the co-injection seismicity contrasted spatially with pre- and post-injection seismicity. It occurred on a planar structure striking at ~ N 35˚ E, dipping at ~ 83˚ to the E, ~ 0.5 km long and extending throughout the depth range ~ 0.8 - 1.6 km bsl (~ 2.11 - 2.91 km (~ 6,860 - 9,450') below surface). This feature was not particularly seismically active before the injection;
2. the earthquake activity propagated north, west and up initially and thereafter occurred throughout the planar structure;

3. pre-injection earthquakes tended to occur in response to normal motion, with moderate crack-opening components, and co-injection earthquakes tended to be strike-slip with larger crack-opening components;
4. after the injection, the size of the crack-opening components returned rapidly to pre-injection levels, but modulation of the sense of the shear component of failure (i.e., the orientation of the principal stress axes) lasted for at least 2 months.

Intense earthquake activity was induced by the injection. The high seismic rate correlated with wellhead pressure (Figure 33 and 34). The onset and cessation of earthquake activity also corresponded to rapid increases and decreases in injection rate. However, this may merely be a result of the correlation of injection rate with wellhead pressure, since the injection rate remained nearly as high as its maximum value throughout the latter half of August, when there was little seismicity.

The location of the stimulated fault inferred from the earthquake activity is shown as a blue line on the fault map of *Davatzes and Hickman* [2007; Figure 35]. The orientation of the structure is similar to major modern faults in the area, *e.g.*, the Coso Wash Fault. Smaller mapped surface faults have a somewhat more northerly strike. The structure extended from well 34A-9 almost as far south as the 38 well pad.

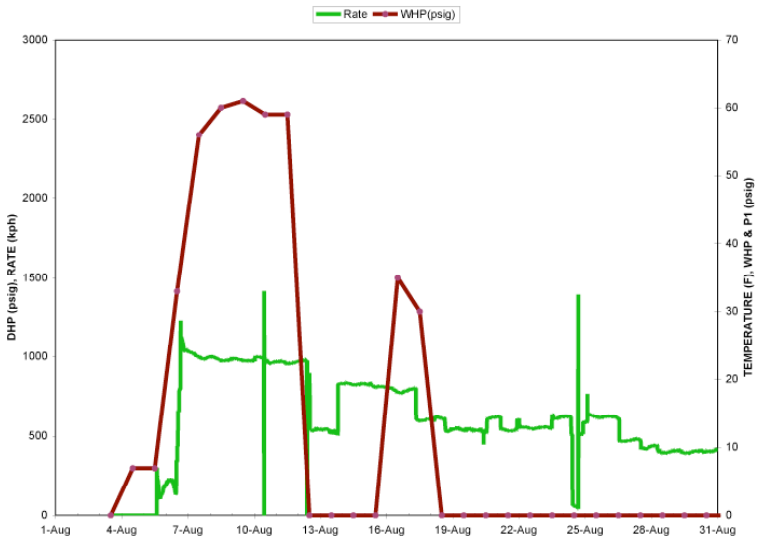

Figure 33: Injection rate (green line) and wellhead pressure (red line) for well 34A-9, August 2004.

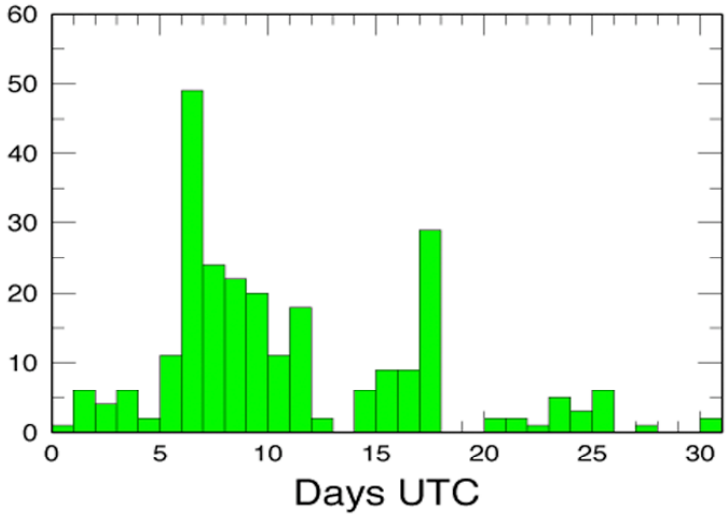

Figure 34: Number of earthquakes per day within 1 km of the base of well 34A-9.

The orientation of the T axes of the co-injection earthquakes is very close to the direction of least principal stress inferred from induced structures in image logs of wells [*Davatzes and Hickman*, 2007; Figure 36]. The stress orientations were little affected by the injection and were consistent with measurements made in local boreholes throughout the pre-, co- and post-injection periods.

The tracer test performed in well 34A-9, 1st September, shortly after the injection, showed strong hydraulic connection with well 38-9 to the south, and a much more delayed connection to well 38A-9 (Figure 19). The best hypocenter locations suggest that the structure that was seismically activated lay midway between these two wellbores, quasi-parallel to their surface traces, and did not intersect either. Since the injected fluid was more readily tapped by well 38-9, this suggests that the fluid flowed downwards towards the bottom of the fault, which would bring it closer to the bottom of well 38-9.

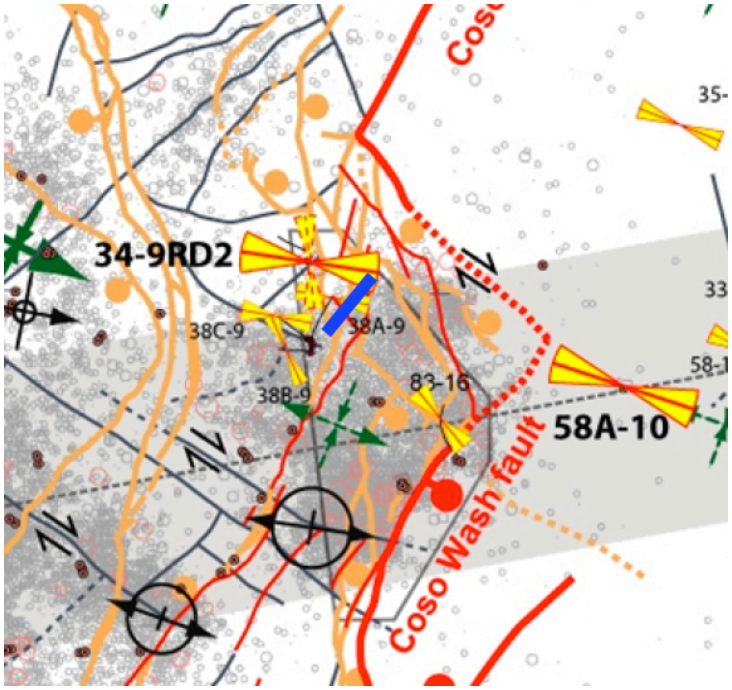

Figure 35: Detail local to well pads 34 and 38 from the fault map of *Davatzes and Hickman* [2007]. Orange: faults active since 1.6 Ma; red: modern faults that have offset Holocene sediments; blue: inferred position of planar structure activated by injection.

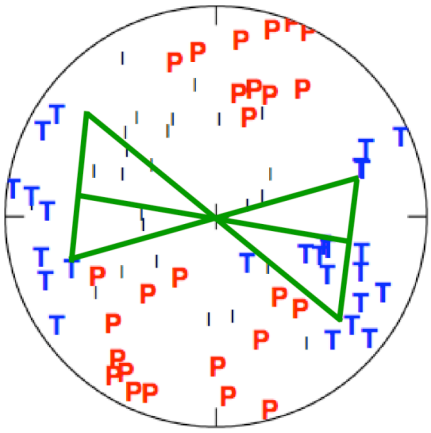

Figure 36: P- and T-axes of co-injection earthquakes. Green: direction of least principal stress inferred from induced structures in image logs of well 34-9RD2 [*Davatzes and Hickman*, 2007].

As a general point, the observation of tracer returns in the producing wells to the south agrees with the seismic observations, which show activation of a structure to the south, and not one to the north. This would suggest that earthquake observations would be relevant in a situation

where EGS stimulations were performed in order to create fracture networks before the producing wells had been drilled.

3.5.5 The EGS experiment in well 34-9RD2, March 2005

3.5.5.1 Details of the well and the stimulation

Before an EGS experiment could be performed in well 34-9RD2, it was necessary to re-work the hole. This was done February – March 2005. In order to ensure that injected fluids entered the formation near the bottom of the hole, the existing slotted liner had to be removed and replaced by one that was not slotted. After removing the slotted liner, open fractures and washout regions were cemented and repaired. On redrilling, however, the bit side-tracked into a large washout zone at ~ 1,415 m (4,600'). The original hole could not be re-found and so the well was redrilled and lined from this depth down to 2,430 m (7,900').

Work then continued with the plan of drilling an additional ~ 150 m (500') and hydraulically stimulating this unlined deep portion of the hole. At 2,654 m (8,625') no fractures or lost circulation had been encountered. However, in the next ~ 20 m (60') three major circulation-loss zones were encountered and total mud loss occurred in a zone at 2,672 m (8,685'). Drilling continued down to 2,700 m (8,775') with total mud losses while injecting water at rates up to 20 l/s (7.5 bpm). A vigorous swam of earthquakes was induced by this unplanned event which thus constituted a somewhat unconventional EGS stimulation and one for which detailed injection data, such as were measured during the stimulation of well 34A-9, are not available.

3.5.5.2 The tracer test in well 34-9RD2

Despite the unconventional nature of this EGS injection, it was possible to conduct tracer tests to explore the fate of fluids injected into well 34-9RD2. Two such tests were conducted. In the first test, 100 kg of liquid 1,3,5-NTS was injected 12th May 2005. The second tracer test was a vapor-phase test using n-propyl alcohol, designed to detect vapor pathways. 500 kg were injected into 34-9RD2 7th July 2005.

The liquid returns from the producing wells are shown in Figure 37. In Figure 38 both liquid and vapor returns are shown together, corrected for thermal decay and normalized by time, flow rate and mass of tracer injected, in order to render them comparable [*Rose et al.*, 2006]. The results may be summarized:

1. Well 38C-9 yielded returns first, with the n-propyl alcohol traveling fastest. The 1,3,5-NTS took a little longer to arrive, and comprised by far the strongest 1,3,5-NTS liquid returns and approximately 75% of the tracer was recovered;
2. Well 38D-9 yielded n-propyl alcohol but no 1,3,5-NTS, suggesting a steam-only pathway from injector 34-9RD2;
3. Well 38B-9 yielded neither tracer;

4. Well 38D-9 yielded n-propyl alcohol. This suggests a steam-only pathway to 38D-9 that bypasses well 38B-9.

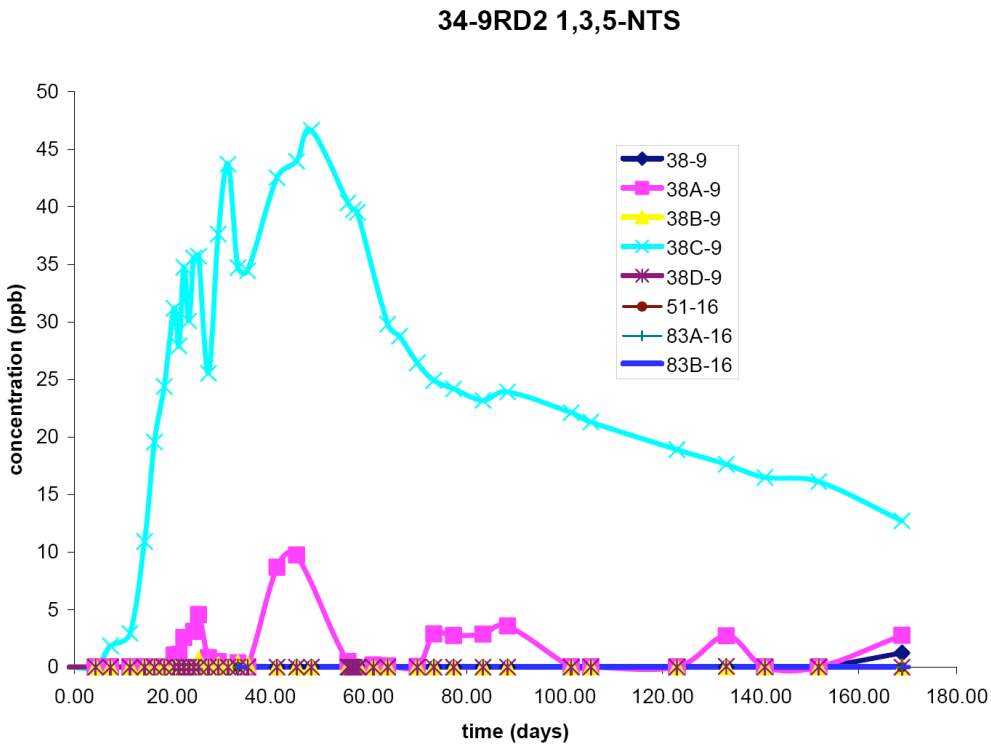

Figure 37: Tracer returns for the 1,3,5-NTS injection [from *Rose et al.*, 2005].

3.5.5.3 Analysis of the induced seismicity

3.5.5.3.1 Earthquake time series and magnitudes

A histogram showing the numbers of earthquakes that occurred day by day for the 3 months surrounding the injection in 34-9RD2 is shown in Figure 39. Earthquakes whose epicenters lie within a horizontal distance of 1.1 km from the base of well 34-9RD2 are shown. The time-history of seismicity is dominated by an intense swarm March 3rd, that accompanied the injection. Over 70 earthquakes were recorded on that day. At other times in the study period, the seismic rate was usually < 10 earthquakes/day.

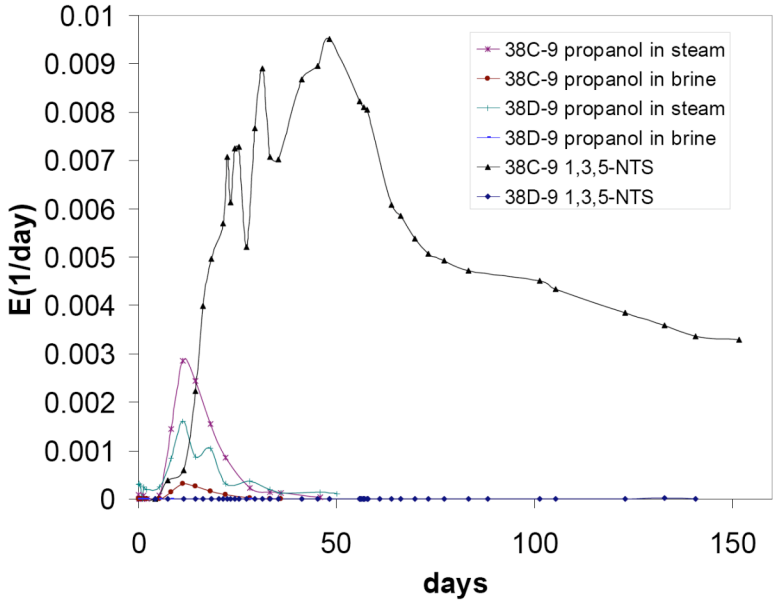

Figure 38: Tracer return curves for the first tracer test in well 34-9RD2 [from *Rose et al.*, 2005].

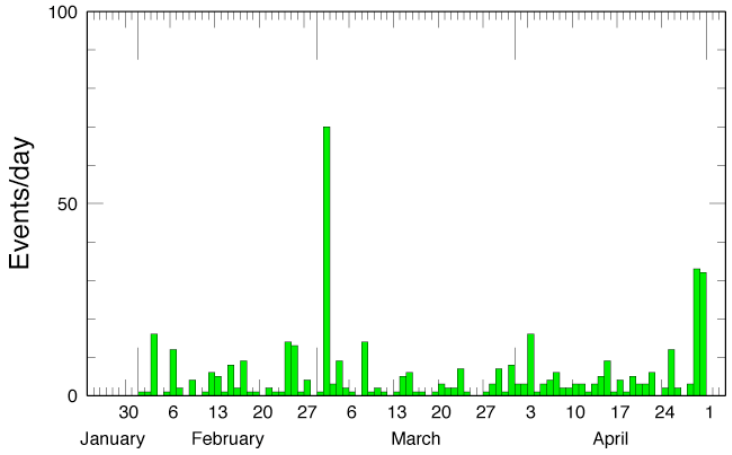

Figure 39: Magnitudes of earthquakes within 1.1 km of the bottom of well 34-9RD2 for the period February - April, 2005.

Plots of magnitude vs. time are shown in Figures 40 - 42. From this it is clear that the swarm of March 3rd included the largest-magnitude earthquakes that occurred in the 4-month study period. The entire swarm occurred very rapidly, and was over in less than 1 hr.

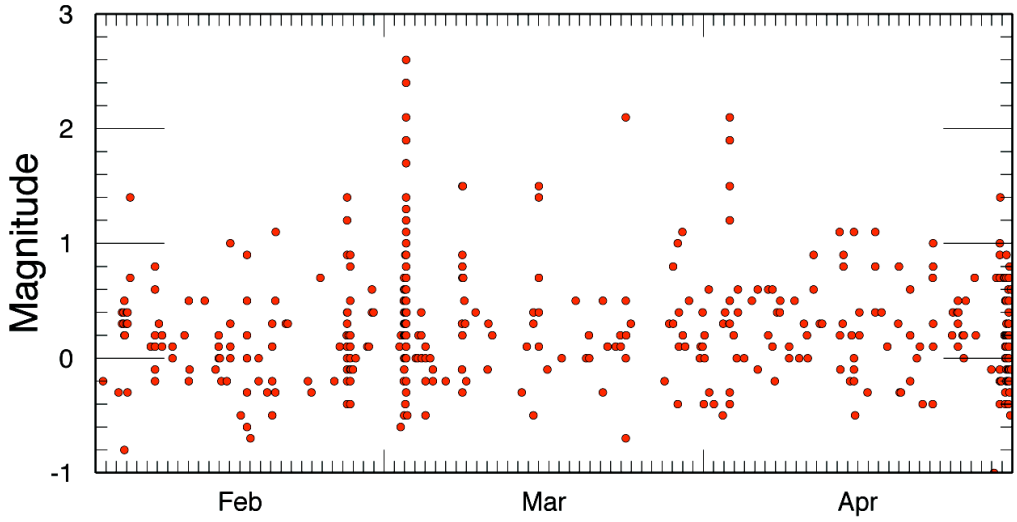

Figure 40: Magnitudes of earthquakes within 1.1 km of the bottom of well 34-9RD2 for the period February - April, 2005.

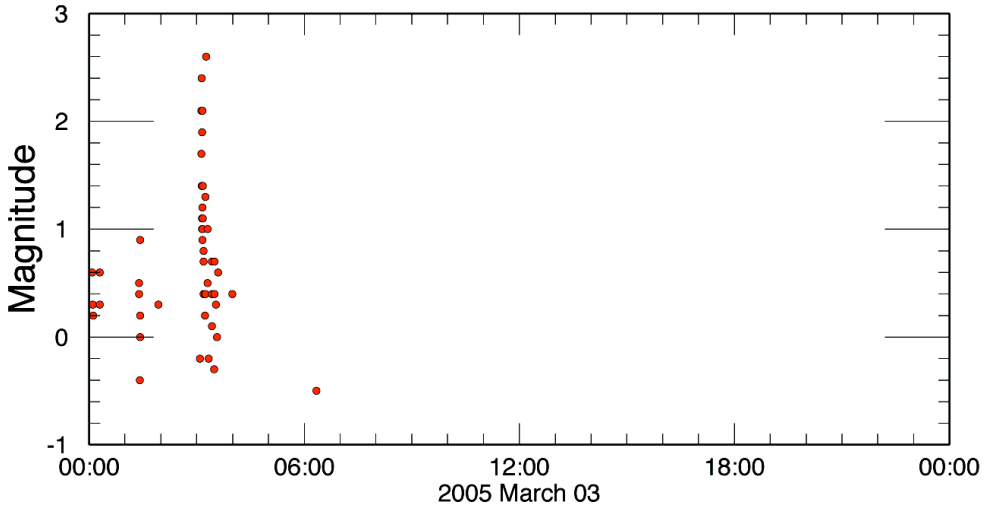

Figure 41: Same as Figure 40, but for March 3rd, 2005 only.

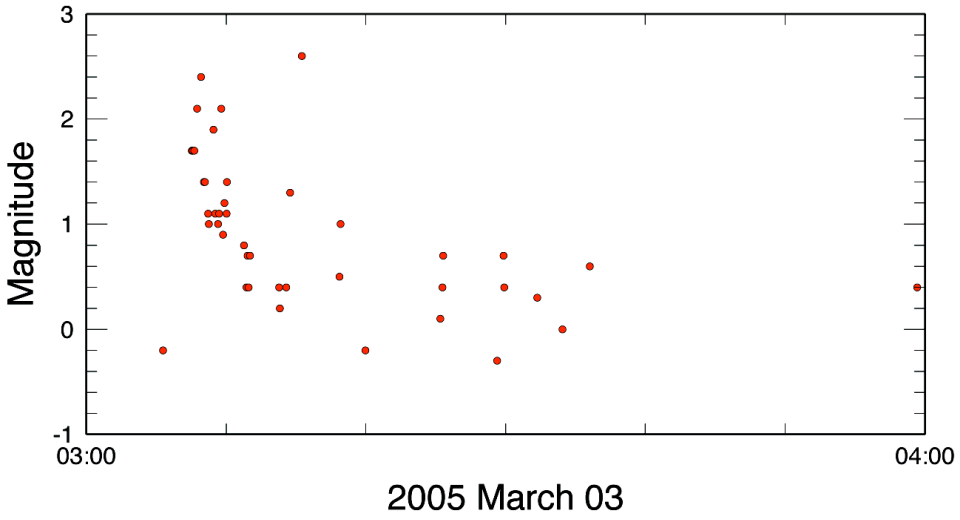

Figure 42: Same as Figure 40, but for 03:00 - 04:00 March 3rd, 2005 only.

On the basis of this pattern of activity, the earthquakes of interest were divided into the following periods for analysis:

1. 20050201 0000 00 20050303 0305 00 – the pre-injection period
2. 20050303 0305 00 20050303 0400 00 – the co-injection period
3. 20050303 0400 00 20050501 0000 00 – the post-injection period

The main, co-injection swarm comprised 44 locatable earthquakes with magnitudes in the range M -0.3 to 2.6. Most of the largest occurred in the first 2 minutes. The largest event was M 2.1 and was felt by at least one member of the crew at the well. Since the expected stimulation was still several weeks away at that point, much of the portable network was not recording. U.S. Navy personnel were in the process of bringing the recorders into the laboratory for maintenance of the GPS clocks and to replace backup batteries on various boards. Data dumps were nevertheless obtained from 6 of the stations that were recording, which provided valuable data.

3.5.5.3.2 Earthquake locations

The data were processed in a similar way to the earthquakes induced by the March 2004 EGS experiment in well 34A-9. Three families of earthquake locations were studied:

1. locations from the U.S. Navy catalog;
2. relatively relocated hypocenters calculated using program **hypocc**, and;
3. hypocenters calculated by repicking the P- and S-wave arrival times using waveform cross-correlation (program **toonpics)** prior to relative relocation (program **hypocc**).

Epicentral maps of the U.S. Navy catalog locations for the entire field for February, March and April 2005 are shown in Figures 43a-e. Selected wells are shown as blue lines. The area around the 34 and 38 well pads was seismically active for the full 3-month period, including the area ~ 1 km SSW of wellpad 34, which was also active during the 2004 EGS experiment in well 34A-9. Details of the U.S. Navy epicenters, and those calculated using **hypocc**, for the co-injection swarm only, are additionally shown at larger scale in Figure 44.

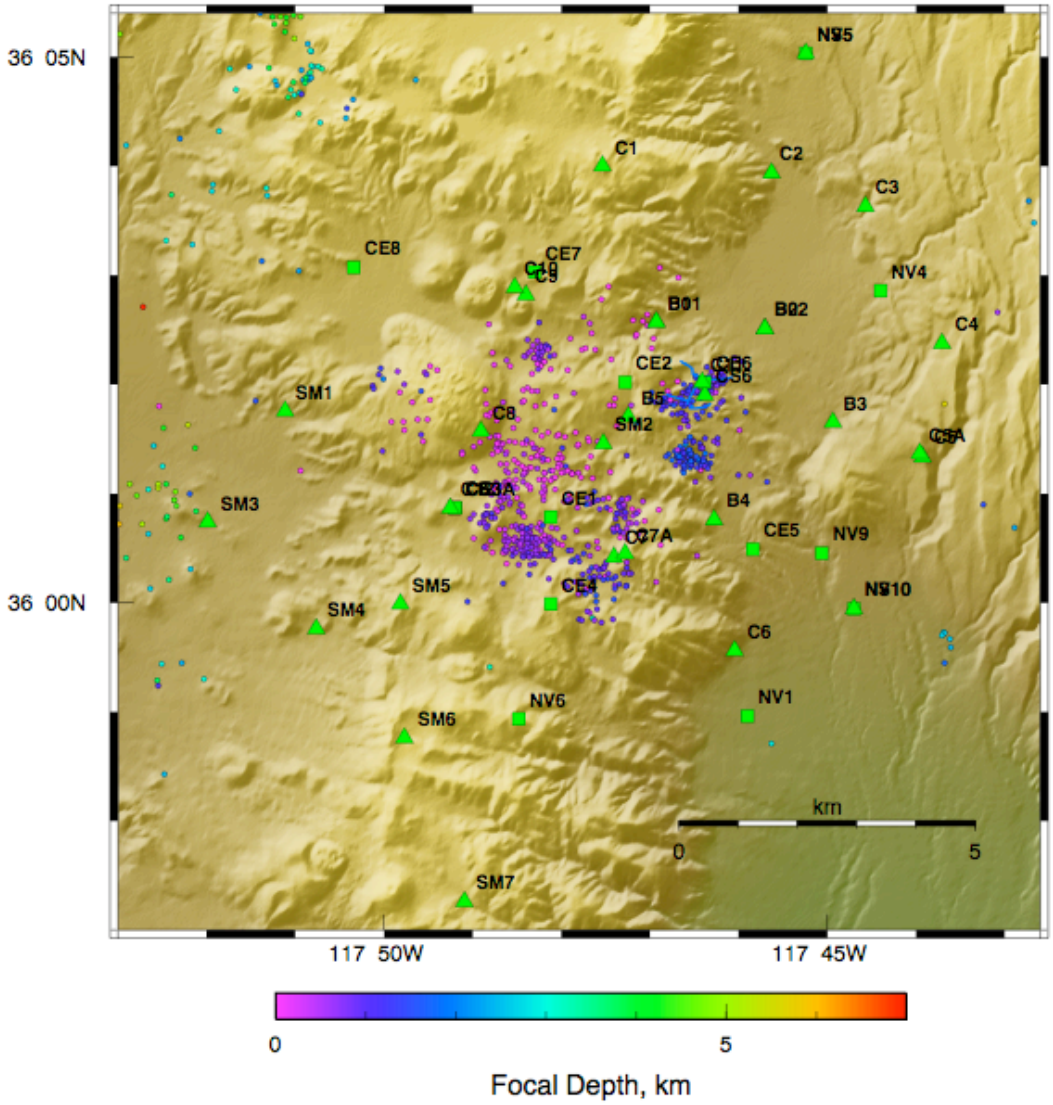

Figure 43a. Epicentral map of U.S. Navy earthquake locations for February 2005. Wells 34A-9, 34-9RD2, 38-9, 38A-9, 38C-9 and 46A-19RD are shown as blue lines.

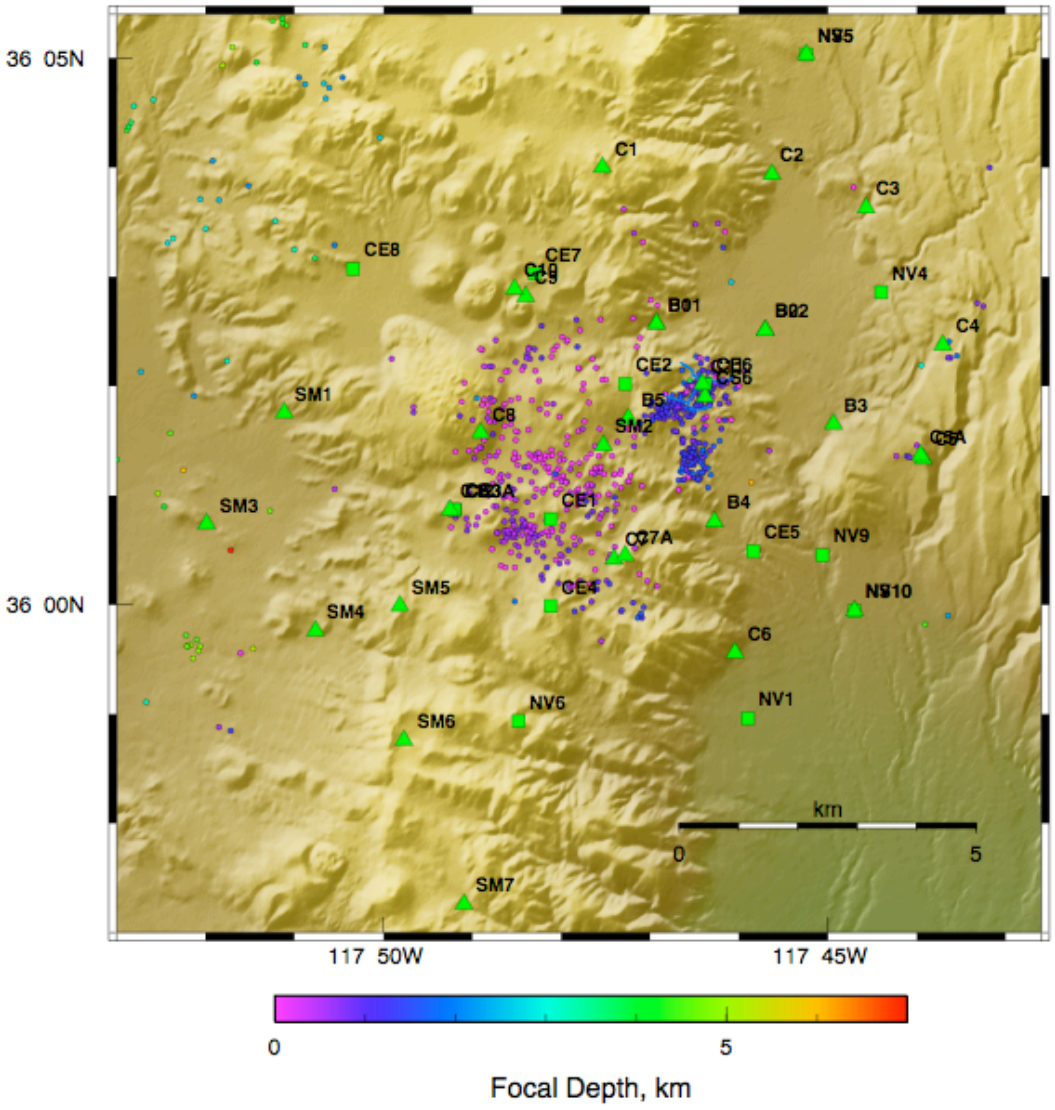

Figure 43b. As for Figure 43a except for March 2005.

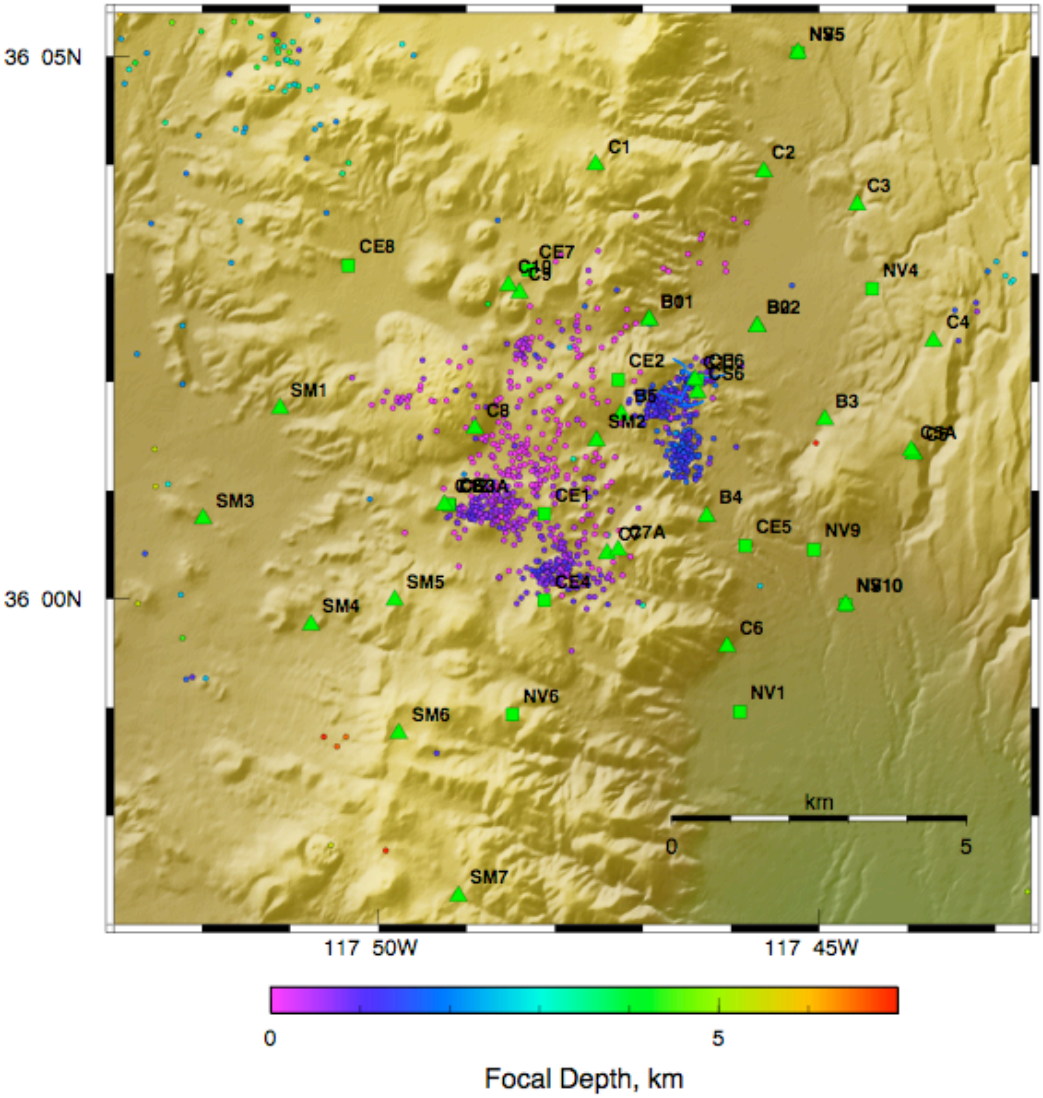

Figure 43c. As for Figure 43a except for April 2005.

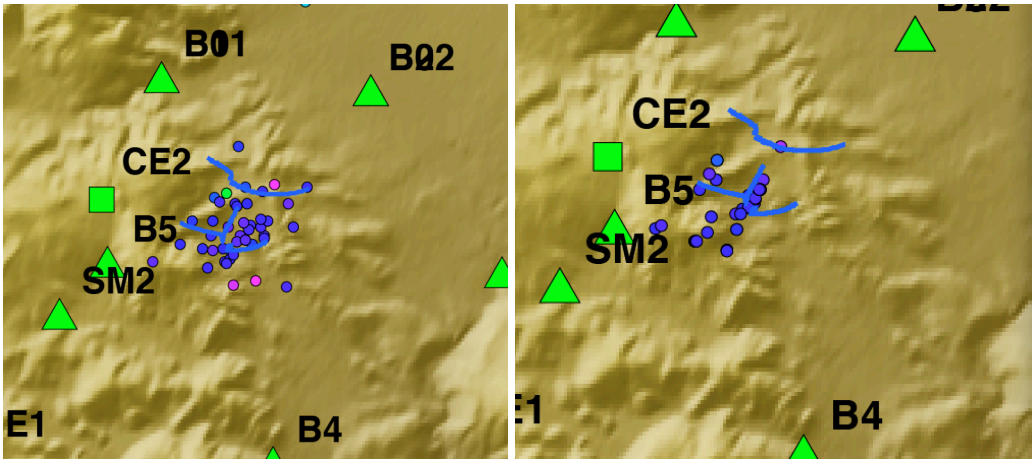

Navy **hypocc**

Figure 44: Maps of co-injection epicenters only, left: from the U.S. Navy catalog, right: from **hypocc**.

Comparison of Figures 44 and 25b show, remarkably, that the EGS injections in wells 34A-9 (in 2004) and 34-9RD2 (in 2005) appear to have both stimulated the same fracture. This is despite the fact that the bottoms of the wells, from where the fluids were introduced into the rock formation, are spaced ~ 1 km apart in a direction approximately perpendicular to the ambient NNE tectonic trend.

The earthquakes were relatively relocated using **hypocc** and also by re-picking the arrival times using **toonpics** prior to relative relocation using **hypocc**. Figure 45 shows the three families of locations in a similar style to Figure 25. The relative relocations obtained using **hypocc** show significantly greater focusing compared with the U.S. Navy catalog locations, for the earthquakes for all of the pre-, co- and post-injection periods. The additional use of **toonpics** prior to **hypocc** improved the clustering still further, but not to the same extent as was achieved for the 34A-9 2004 injection. The reason for this is not clear. There are as yet few case histories of application of the software, and optimal approaches are still under development. The remaining diffuseness in the earthquakes may be a real feature of this data set.

In contrast with the 34A-9 2004 injection, the pre-injection earthquakes for the 34-9RD2 experiment clearly formed elongate distributions that suggested the position of an active planar structure. The diffuse U.S. Navy locations suggest a single structure with an orientation ~ N 50˚E, considerably more easterly than the ambient NNE tectonic trend, and dipping steeply to the SE (Figure 45a, top left panel). Such a large easterly strike would be surprising, in view of the trends of surface mapped faults. The epicentral map of earthquakes relocated using **toonpics** and **hypocc** (Figure 45a, top right panel) shows considerably more structure, and suggests instead that the earthquakes form several clumps that may each represent a NNE-striking en-echelon fault.

The co-injection events, when relocated using **hypocc**, and **toonpics** + **hypocc** combined (Figure 45b), suggest that most of the earthquakes represented failure on a fault striking at ~ N 20˚E, dipping steeply to the W and located a little east of the 38A-9 wellbore. This is a very similar location to the fault activated by the 34A-9 injection in 2004. A few earthquakes suggest a second fault may have been activated, lying ~ 500 m west of, and running parallel to, the main fault.

The post-injection earthquakes (Figure 45c) show a distribution similar to the co-injection earthquakes, with distinct clusters observable in the events located using **toonpics** + **hypocc**, suggestive of several discrete activated structures (Figure 45c, top right panel), features that are not readily distinguishable in the U.S. Navy catalog locations (Figure 45c, top left panel). The locations of faults activated by the EGS experiments in both well 34A-9 and well 34-9RD2 are summarized in Figure 46.

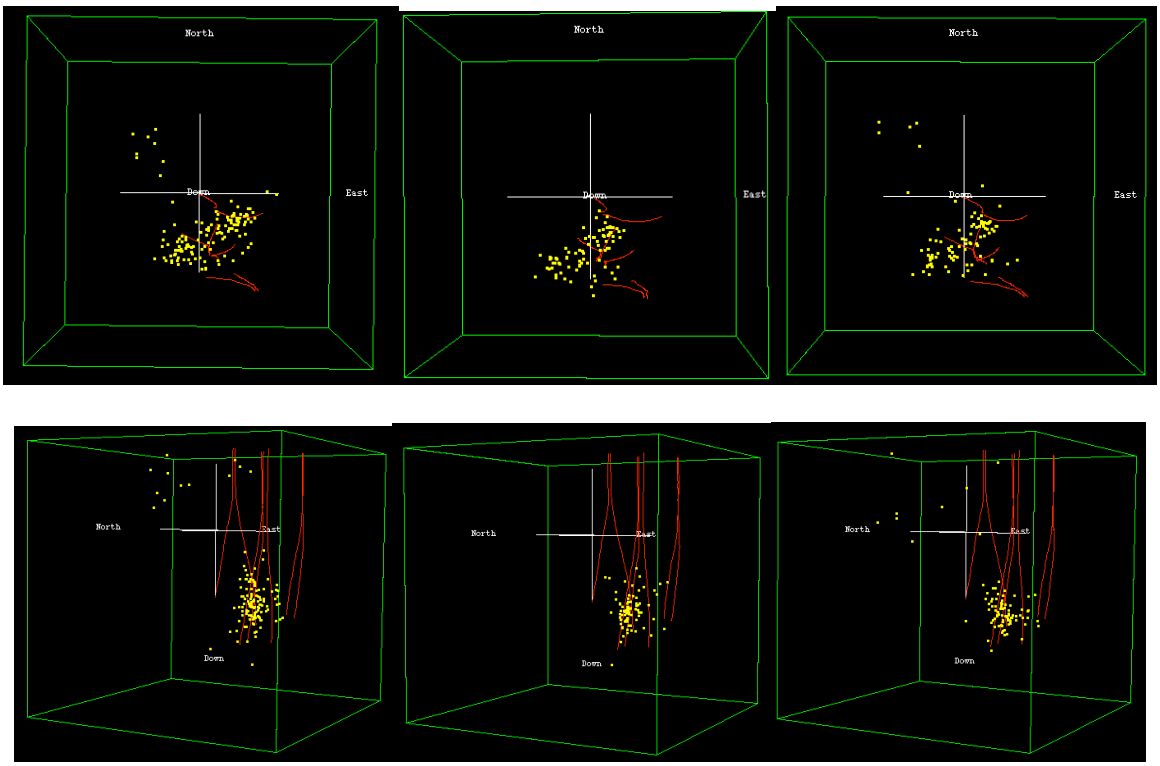

U.S. Navy **hypocc** **toonpics + hypocc**

Figure 45a: Pre-injection period. Locations are displayed as screenshots of rotatable 3D plots. Top row: horizontal maps, bottom row: vertical cross sections rotated so the line of sight is NE. Red lines indicate wells 34A-9, 34-9RD2, 38A-9, 38C-9, 38B-9, 38-9, 51-16 and 51A-16. Left panels: U.S. Navy catalog locations, middle panels: **hypocc** locations, right panels: **hypocc+toonpics** locations.

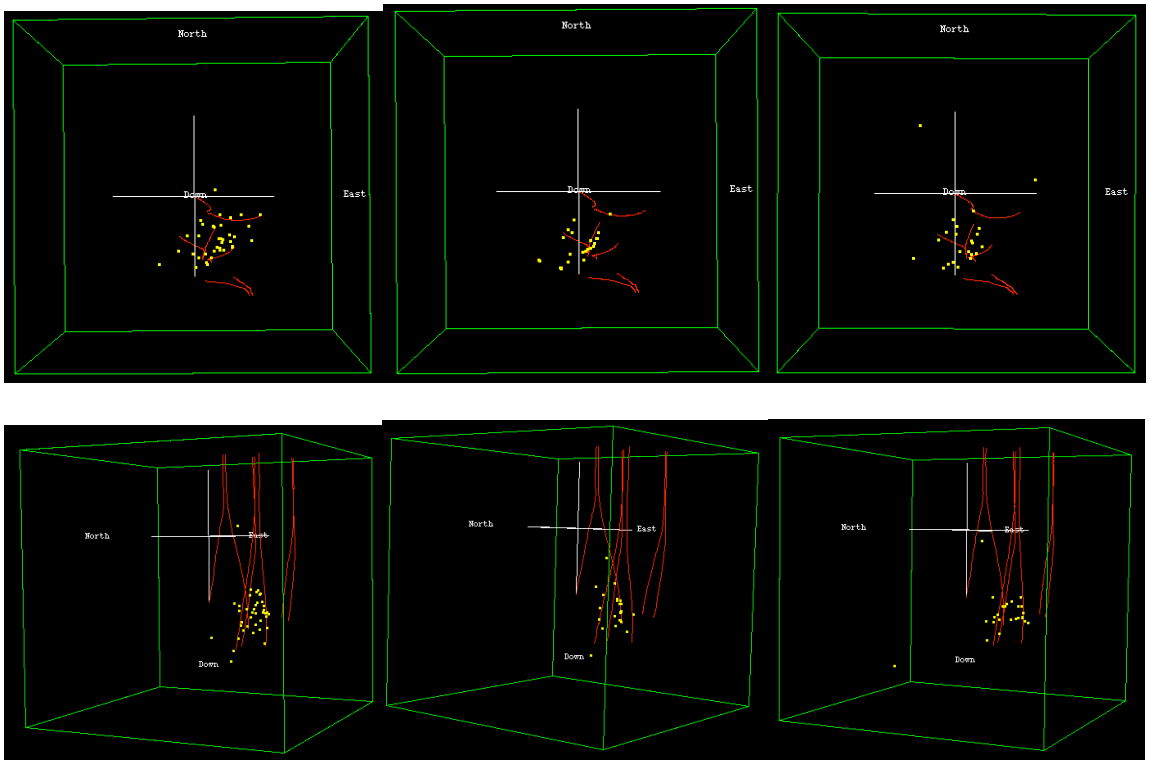

U.S. Navy **hypocc** **toonpics + hypocc**

Figure 45b: As for Figure 45a except for co-injection period.

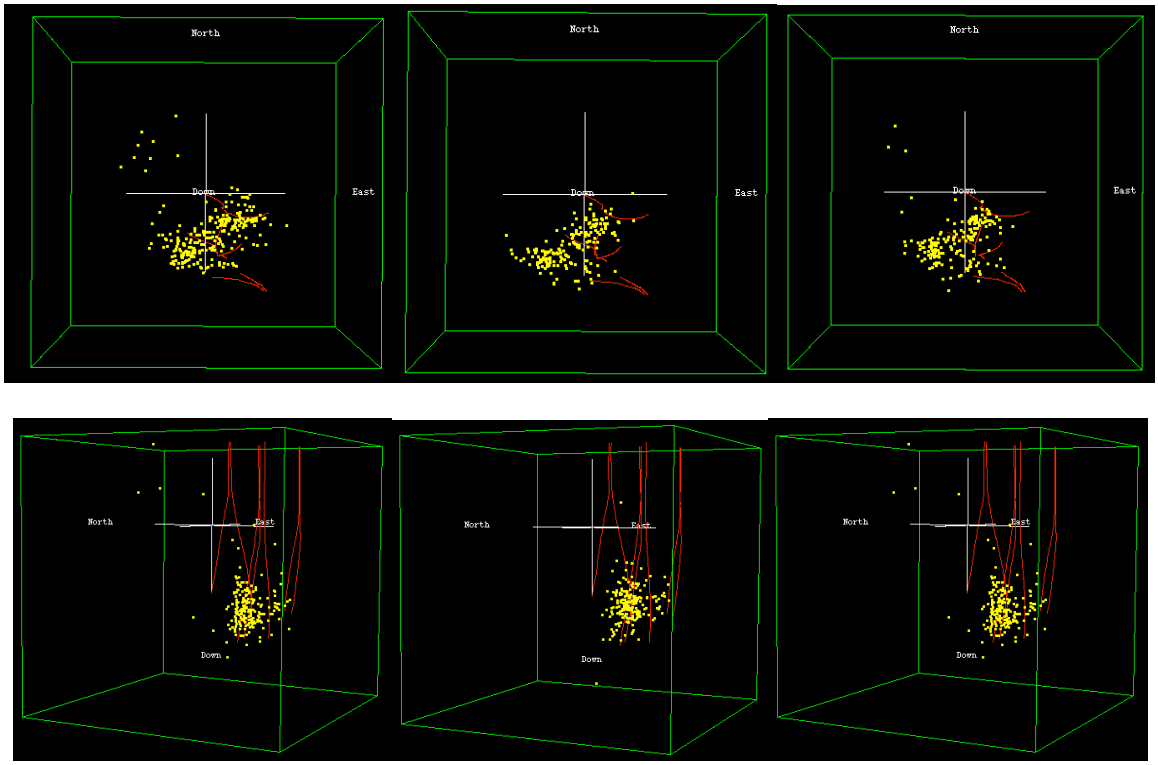

U.S. Navy **hypocc** **toonpics + hypocc**

Figure 45c: As for Figure 45a except for co-injection period.

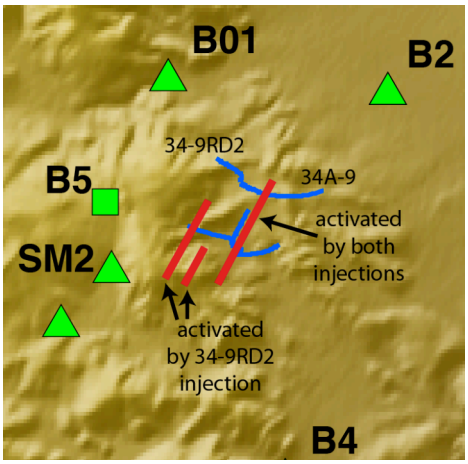

Figure 46: Faults activated by EGS experiments in wells 34A-9 and 34-9RD2, deduced from earthquake relative relocations.

3.5.5.3.3 Chronological distribution of the co-injection earthquakes

Earthquake occurrence time is plotted vs. northing, easting and depth in Figure 47 for the ~ 50-min period during which the injection-induced swarm lasted. The earthquake activity migrated N, E and up during the first ~ 10 min, after which it was scattered throughout the activated structure and showed no further clear systematic behavior. The hypocenters delineated a fault ~ 700 m long, which lay mostly in the depth range ~ 0.8 - 1.425 km bsl (~ 2.05 - 2.71 km (~ 6,662 - 8,808') below the surface). This is similar to the depth range of the structure activated by the injection in well 34A-9 in 2004.

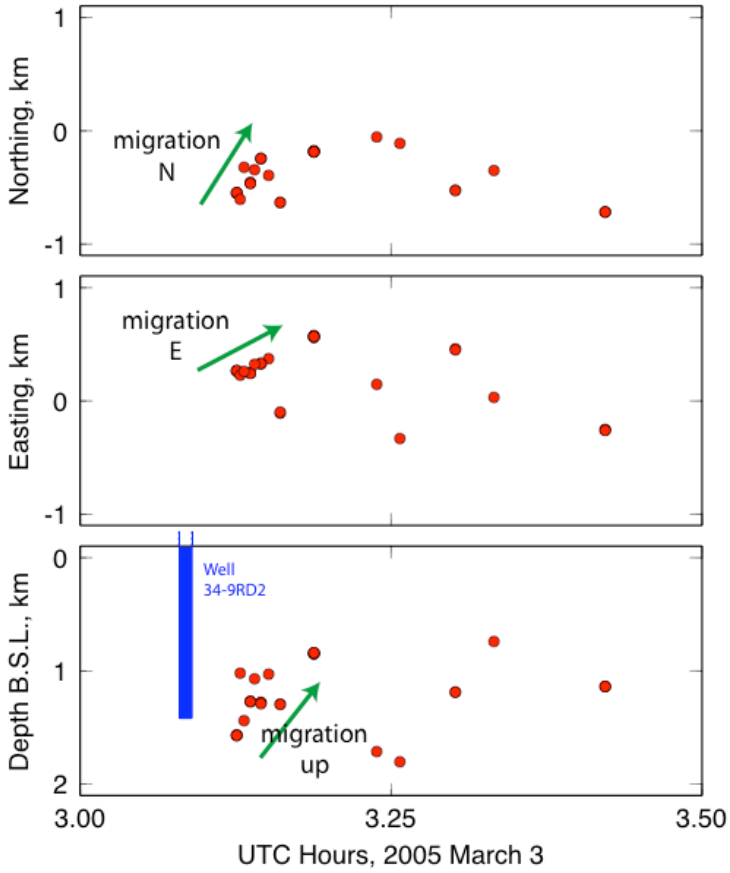

Figure 47. Northing, easting and depth vs. time for co-injection earthquakes, March 2005.

3.5.5.3.4 Moment tensors

Moment tensors were attempted for all of the largest earthquakes in the 3-month period February - April 2005. Table 3 gives the numbers of good moment tensors obtained for the pre-, co- and post-injection periods.

Table 3: Numbers of moment tensors derived for the pre-, co- and post-injection periods.

Time period	# of moment tensors
February:	28
March, pre-swarm:	7
March, co-swarm:	14
March, post-swarm:	17
April:	34
Pre-injection:	35
Co-injection:	14
Post-injection:	51
total:	**100**

A remarkable feature of the co-injection earthquakes was the uniformity of their moment tensors (Figure 48). All the earthquakes had mechanisms that resembled normal or combined normal and strike-slip motion. The dilational portions of the focal sphere were mostly reduced, however, indicating net explosive mechanisms.

Individual moment tensors do not have unique interpretations in terms of physical source processes. The mechanisms shown in Figure 48 could correspond to motion on structures or faults orientated similar to either nodal curve, any plane in between, and even some outside of this range . The ambiguity can be reduced by adding independent constraints, however. In Figure 48, the fault delineated by the relatively relocated hypocenters (Figure 45b), which must indicate an overall activated structure, is superimposed on the moment tensor at top left. This structure bisects the dilatational field, suggesting that it corresponds to an opening crack and not a shear fault. Individual mechanisms of post-injection earthquakes were much more variable (Figure 49).

The results are displayed in the same manner as for the injection in well 34A-9 in 2004, as source-type and source-orientation (P- and T-axis) plots, in Figures 50a-c. The main results have a number of features in common with the results from the 34A-9 2004 EGS experiment:

1. All the source-type plots show that many of the earthquake mechanisms had a net volume increase, i.e., they correspond to opening cracks. A few earthquakes in both the pre- and the post-injection sets had implosive components, but these are mostly relatively small and comparable to the errors in the volumetric component of the moment tensors.
2. Unusually, none of the co-injection earthquakes had implosive components, and none had negative CLVD components. There are 14 earthquakes in the co-injection set, a relatively large number, and their moment tensors are relatively well constrained. These features are thus probably real. The meaning of the CLVD components is not well understood, however. Small geothermal earthquakes with positive CLVD components (i.e., source

types that plot on the left half of the source-type plot) usually lie on a line connecting the DC point to the +Dipole point, suggesting an opening crack with a small amount of fluid inflow. Earthquakes whose source types plot on the right half of the source-type plot might result from shear/tensile crack doublets where the normal to the tensile crack does not lie in the same plane as the P- and T-axes of the shear crack. This issue is, as yet, poorly understood.

3. The pre-injection earthquakes have T-axes orientated generally WNW, similar to what was observed for the 34A-9 sequence. The P-axes are most commonly sub-vertical, with a few subhorizontal and trending NNE/SSW. This indicates dominantly vertical motion with subsidiary strike-slip motion in a similar sense to the ambient tectonic trend. The P- and T-axes of the co-injection earthquakes are systematically distributed with the P-axes falling in a narrow NNE/SSE band and the T-axes subhorizontal and orientated WNW. The post-swarm earthquakes lack sub-horizontal P-axes.

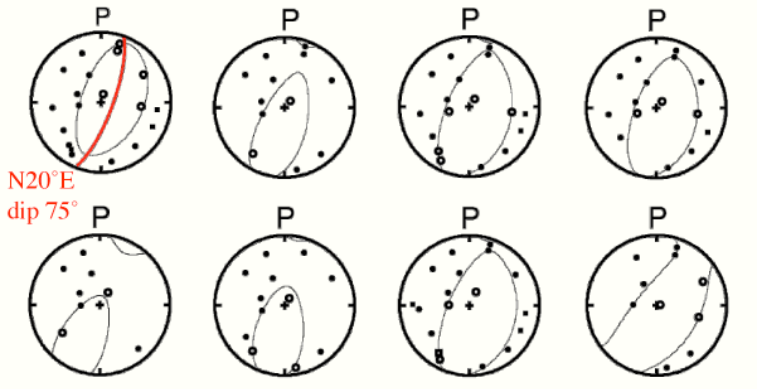

Figure 48: Moment tensor results for 8 co-injection earthquakes. The fault delineated by the relatively relocated hypocenters (Figure 45b) is superimposed on the moment tensor at top left.

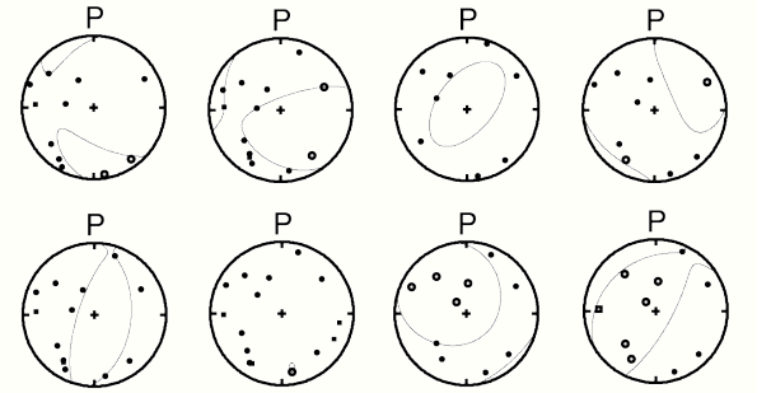

Figure 49: Moment tensor results for 8 post-injection earthquakes.

The picture that emerges is essentially similar to that of the injection in well 34A-9 though with slight variations. Prior to the injection much stress release was in the normal-faulting mode. During injection there was a larger tendency for strike slip motion, and following injection a reduced component of strike-slip motion occurred compared with pre-injection earthquakes. The dearth of strike-slip earthquakes was initially strong for the first month following injection (Figure 50b, right panel) but this reduced during the subsequent month (Figure 50c, right panel).

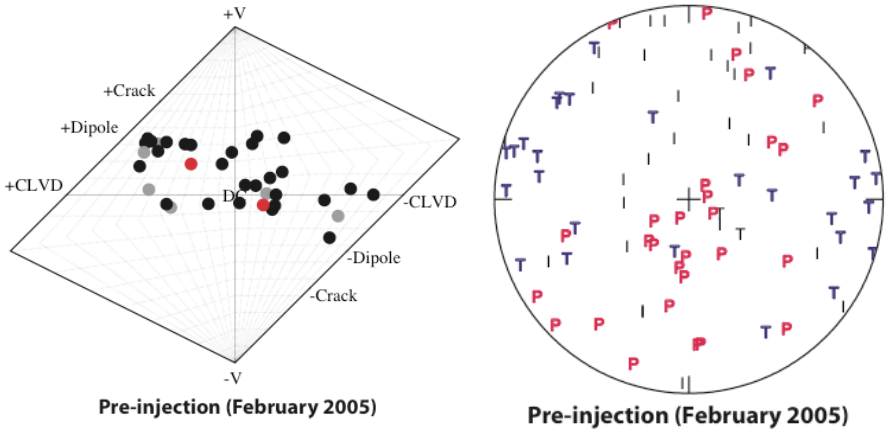

Figure 50a. Moment tensor results for February 2005. Left: Source-type plot for the 28 moment tensors calculated. Red: excellently constrained moment tensors, black: well-constrained, gray: weakly constrained. Right: Equal-area plot of pressure (P), intermediate (I) and tension (T) axes for the same moment-tensor data set.

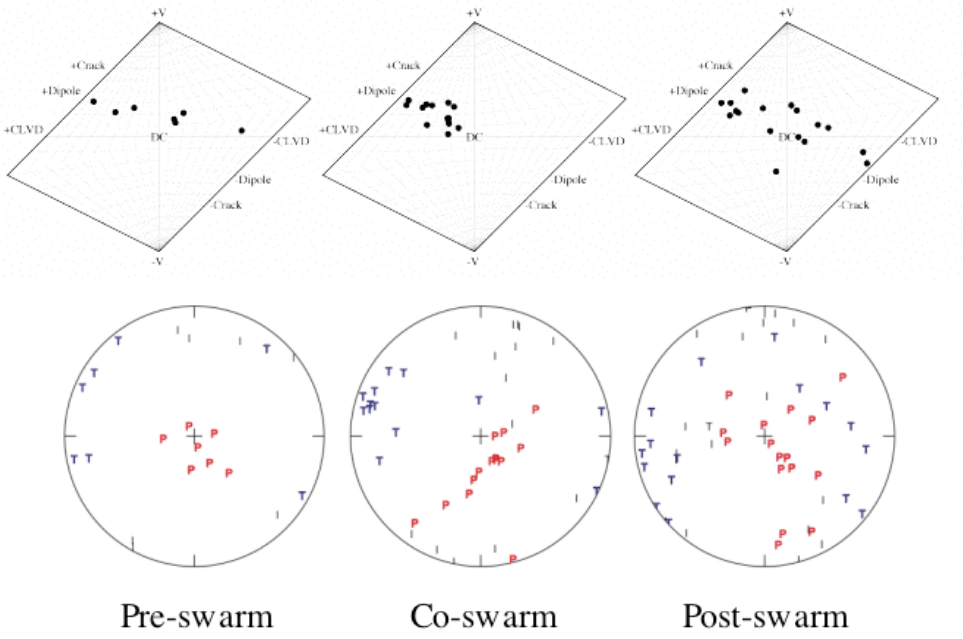

Figure 50b: Top: Source-type plots for the pre-, co- and post-injection periods in March, 2005. Bottom: Source orientation plots for the same earthquake sets.

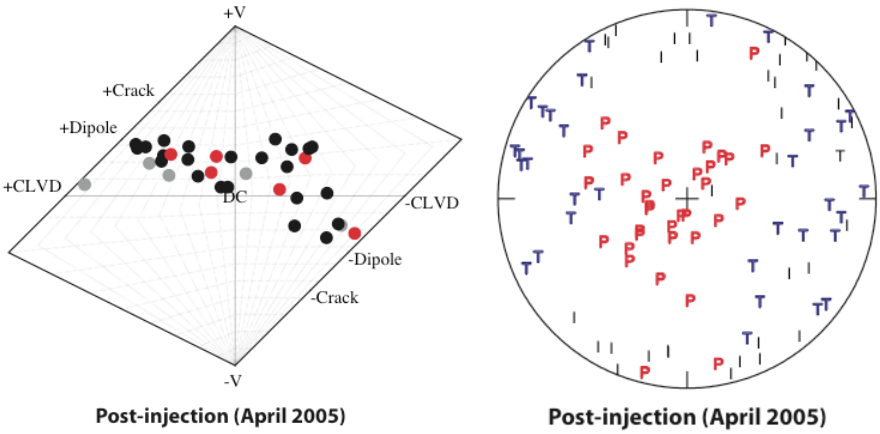

Figure 50c: Same as Figure 50a except for April 2005.

A schematic model that combines and summarizes the results from the hypocenter locations and moment tensors is shown in Figure 51.

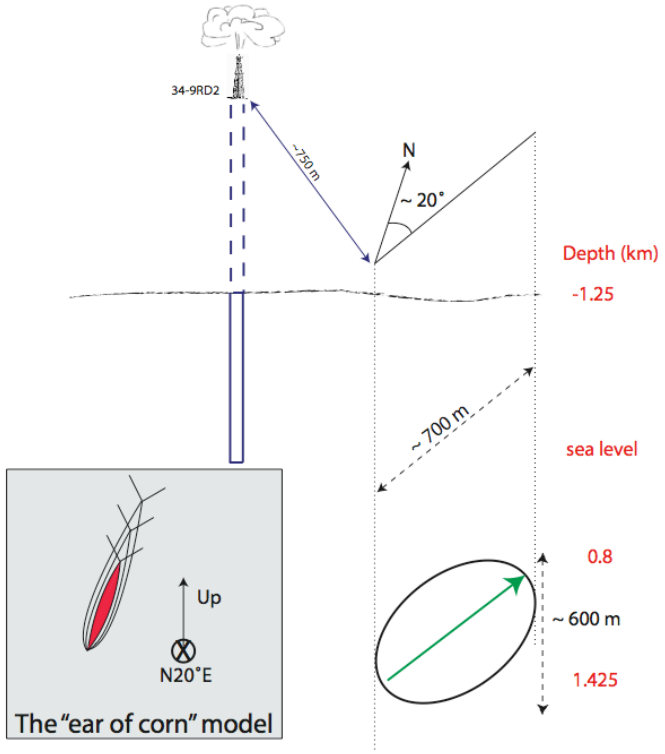

Figure 51: Schematic diagram summarizing the inferences that can be made from the earthquake locations and moment tensors concerning the location, size and mode of failure that accompanied injection in well 34-9RD2 in March 2005.

3.5.5.3.5 Joint interpretation with other results

The main results from the earthquake analysis for the injection in well 34-9RD2, and comparison with the results for the EGS experiment in well 34A-9, may be summarized as follows:

1. the seismic rate in the volume of interest before, during and after the injection was high compared with the months preceding the injection in well 34A-9;
2. the earthquakes that occurred prior to stimulation of well 34-9RD2 were already clustered on the fault that was later activated. This might indicate that the effects of the stimulation of well 34A-9 were still felt;
3. far fewer co-injection earthquakes were induced by the injection in 34-9RD2 compared with the injection in well 34A-9. This is unsurprising given the much lower wellhead pressures involved (atmospheric only), the shorter duration and the smaller volumes of liquid injected, for the former event;
4. surprisingly, the co-injection earthquakes for both injections occurred in the same volume, suggesting that the same structure was activated, despite the fact that the bottoms of the two wells are ~ 1 km apart horizontally;
5. there is some suggestion in the locations of the co-injection earthquakes for well 34-9RD2 that a second structure parallel to the main fault and 500 m to the west was also activated (Figure 45b);
6. the structure was activated from south to north and from bottom to the top. It was ~ 700 m long, ~ 600 m high, and had a strike of ~ N20˚E and a dip of ~ 75˚ to the W;
7. the co-injection earthquakes were very uniform in mechanism and showed dominantly normal failure with a subsidiary component of strike-slip motion. Pre- and post-injection earthquakes had much more variable mechanisms;
8. pre-, co- and post-injection earthquakes all had significant crack-opening components. Minor implosive components were observed but are probably statistically insignificant;
9. pre-injection earthquake mechanisms tended to have more strike-slip components than was the case for earthquakes prior to the 34A-9 EGS experiment. Co-injection earthquakes had predominately normal mechanisms with subsidiary strike-slip motion. Post-injection earthquakes largely lacked strike-slip components.

Unfortunately, parameters such as downhole pressure, injection flow rate, pressure, temperature of injectate and wellhead pressure are not available for the mud-loss event in well 34-9RD2 since it was unplanned and uncontrolled. The most relevant independent data that can support the results of the earthquake analyses comprise the results of borehole stress measurements and tracer testing.

The orientations of principal stresses indicated by the earthquake P- and T-axes are broadly consistent with the borehole stress measurements taken in well 34-9RD2. This confirms the results obtained for the earthquakes associated with the EGS experiment in well 34A-9.

The proposed fault just west of production well 38A-9 was successfully ground truthed using surface geological observations and data from a televiewer borehole log in well 34-9RD2 (Figure 52). A Quaternary fault scarp, dipping to the W is observed in surface sediments just north of well 34A-9. In addition, there is evidence for a fault intersecting the well bore of well 34-9RD2. The proposed seismically active fault lies colinear to these.

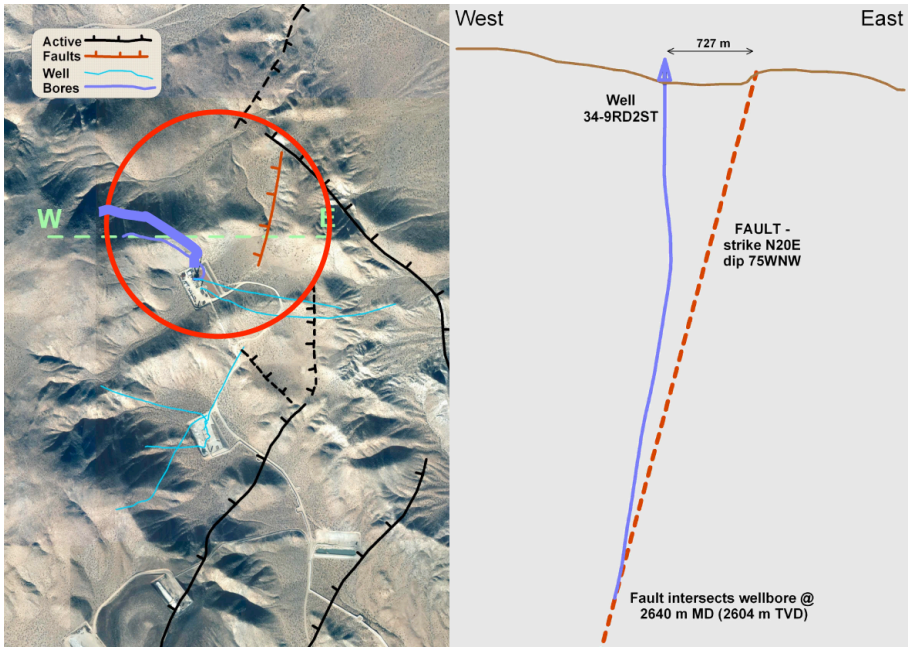

Figure 52: Ground truthing of lineation detected in relatively relocated earthquake hypocenters from the March 2005 injection into well 34-9RD2. The feature correlates with surface topography and fault intersection detected in wellbore televiewer data.

Both liquid-phase and vapor-phase tracer tests were performed in well 34-9RD2 following the mud-loss event. Liquid tracer returns arrived strongly and rapidly in producing well 38C-9, and weakly and with greater delay in well 38A-9. Vapor tracer returns arrived most strongly in steam from wells 38C-9 and 38D-9, and weakly and later in brine in well 38C-9. These results, along with those from the tracer test in well 34A-9, are shown schematically in Figure 53.

It is clear that there is significant cross-strike connectivity at depth in the production/injection volume in this part of the field. Not only did the injection in well 34-9RD2 induce vigorous seismicity on a fault considerably to the E, but tracers returned from production wells off-strike for both injections.

It appears that the most critically stressed fault in this region is the easternmost one, since it was strongly seismically activated by both injections. Lower levels of seismicity were induced on the westernmost two faults illustrated in Figure 53: The three hypothesised faults are likely to comprise elements of an en-echelon zone and be connected by faults non-optimally orientated

for failure in the ambient stress field or cavity-rich permeable zones. Significantly, little seismicity was induced north of either well, suggesting that the faults there are less critically stressed than those to the south.

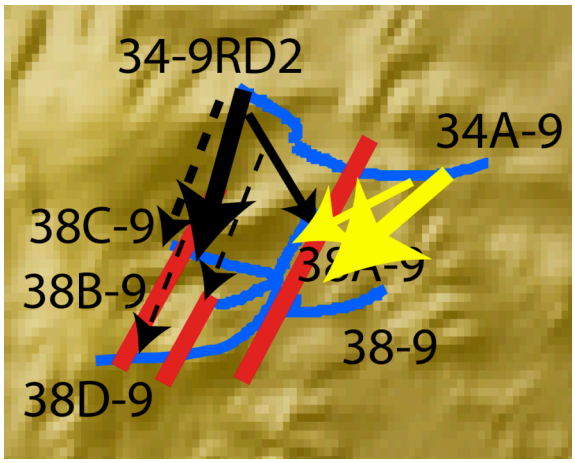

Figure 53: Schematic diagram showing the fates of tracers injected in wells 34A-9 and 34-9RD2, after stimulation. Blue: boreholes, red: faults seismically activated by injections, solid arrows: liquid tracers, dashed arrows: vapor tracers, black: 34-9RD2, yellow: 34A-9. Width of arrows indicates strength of returns, not to scale.

3.5.6 The planned EGS experiment in well 46A-19RD, January 2007

3.5.6.1 Details of the well

The following information was provided by the U.S. Navy. The wellpad of well 46A-19RD is in BLM West land. There are 2 wellheads on the pad, 46-19, and 46A-19. Both have been redrilled and the redrilled wells are coded 46-19RD and 46A-19RD. The old bores below ~ 3,000' are sealed off. The drilling completion dates are:

46-19	May 1988	6801'	(2093 m, producer)	
46-19RD	Oct 1998	7559'	(2326 m, injector)	Still injecting February 2007.
46A-19	Dec 1988	6996'	(2153 m, producer)	
46A-19RD	Oct 1994	13,500'	(4115 m, injector)	Injection started April 1995 and tailed off and stopped January – March 2006.

The original wells were drilled for production, but when they ceased producing they were redrilled for injection. BLM West is the hottest, highest-enthalpy part of the field and pressure and production have remained fairly constant since production started in the late 1980s. Whereas

reservoir pressure in BLM East is declining in production at 2-3%/year, the decline in BLM West is only ~ 1%/year.

It is planned to conduct an injection experiment in well 46A-19RD in 2009. 46A-19RD is an ideal target because it is very deep and it penetrates below the main reservoir where permeability is high. It is hoped to bring about deep pressure, and perhaps mass support in the producing reservoir above. The project is expected to cost ~$5.5 million, and if successful total payback is estimated to be achieved in 1.35 - 1.9 years.

46A-19RD is directionally-drilled, and underlies several producing wells. The objective of injection is to create transmissive fractures from the injection well to the producers so that fluids injected will convert to steam and hot brines that will increase production in the other wells. When it goes ahead, this experiment will be globally unique – a first test of a procedure that has been widely discussed amongst commercial practitioners. Fracture stimulation will involve forcing fluid into a tight, superheated (345˚C), impermeable wellbore using a combination of high-pressure/high-rate, low-pressure/low-rate, and low-pressure/high-rate injection. Surface pressures of > 345 bars will be required. Downhole hydrostatic pressures are expected to exceed 770 bars.

Near-real-time seismic monitoring will comprise a critical element of the operation. Earthquakes, and parameters at the wellhead during injection, *e.g.*, pressure, are essentially the only data that can be monitored during injection to give information on the efficacy of the experiment. Of these data, only the earthquakes can give information on the fate of the injected fluids. It is thus indispensable to monitor the induced earthquake activity in as near real time as possible, if it is to be used to guide injection operations.

When the work described in this report was done, it was planned to conduct the injection experiment in late January 2007. The experiment did not occur because of unforseen difficulties in replacing the liner in the well prior to injection. Nevertheless, valuable information on the seismicity has been acquired, which will provide useful background information when the experiment finally goes ahead.

In addition, considerable progress was made in automating data processing and speeding up calculation of useful parameters such as relative relocations and moment tensors. A modus operandi was developed in the weeks leading up to the wellhead work. In this scheme, information on the seismicity will be calculated rapidly around the clock and uploaded to a password-protected website that could be interrogated as required during injection, http://cosomeq.wr.usgs.gov/ (Figures 54 and 55). After consideration of the experimental requirements, degree of automation currently possible, and staffing levels, it was planned to upload data processing updates at 2-hourly intervals throughout the experiment. Although the injection did not go ahead when planned, this infrastructure is in place for use when the experiment is finally performed.

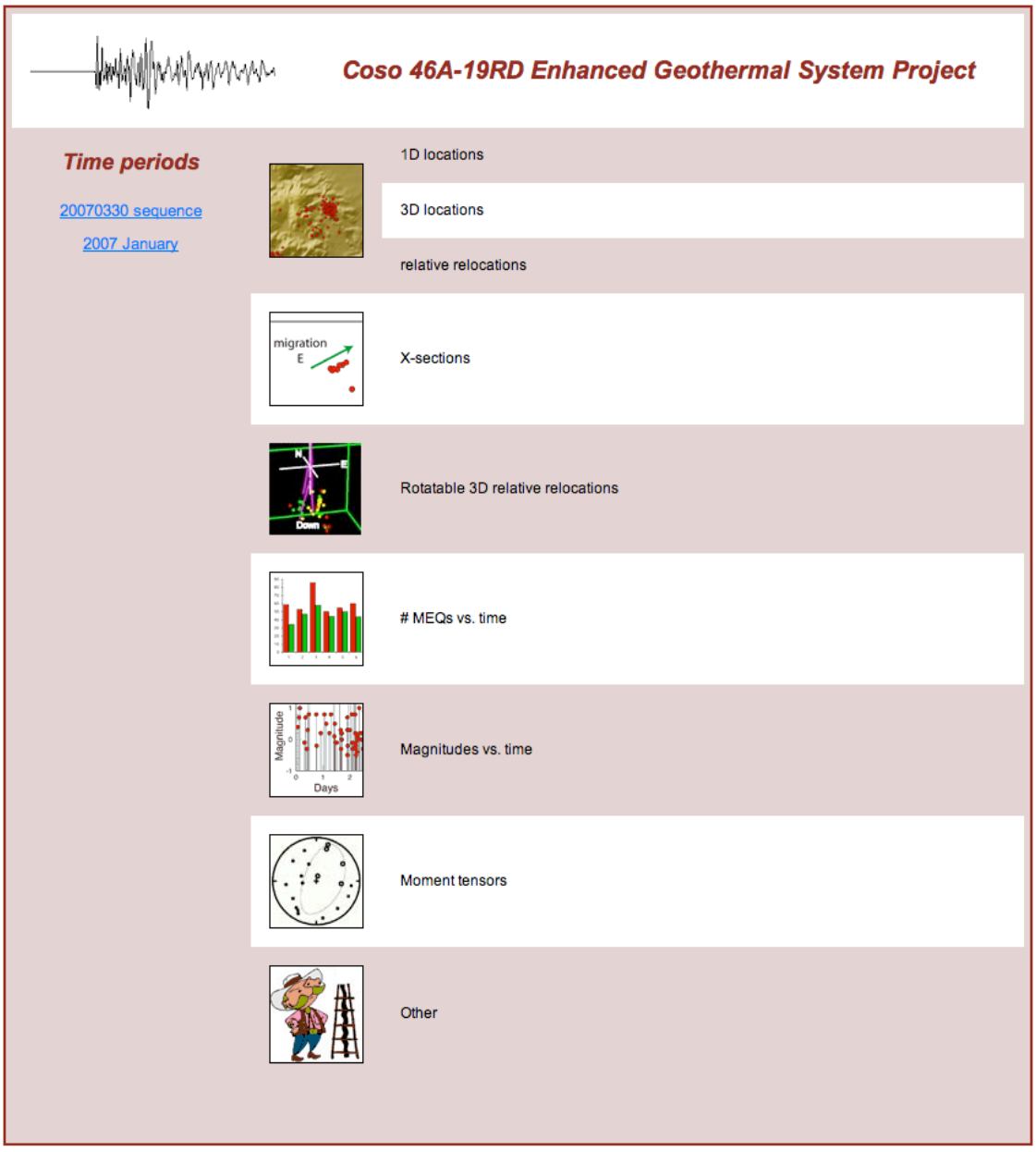

Figure 54: Home page of the website developed to provide near-real-time earthquake parameters for use during the EGS experiment in well 46A-19RD.

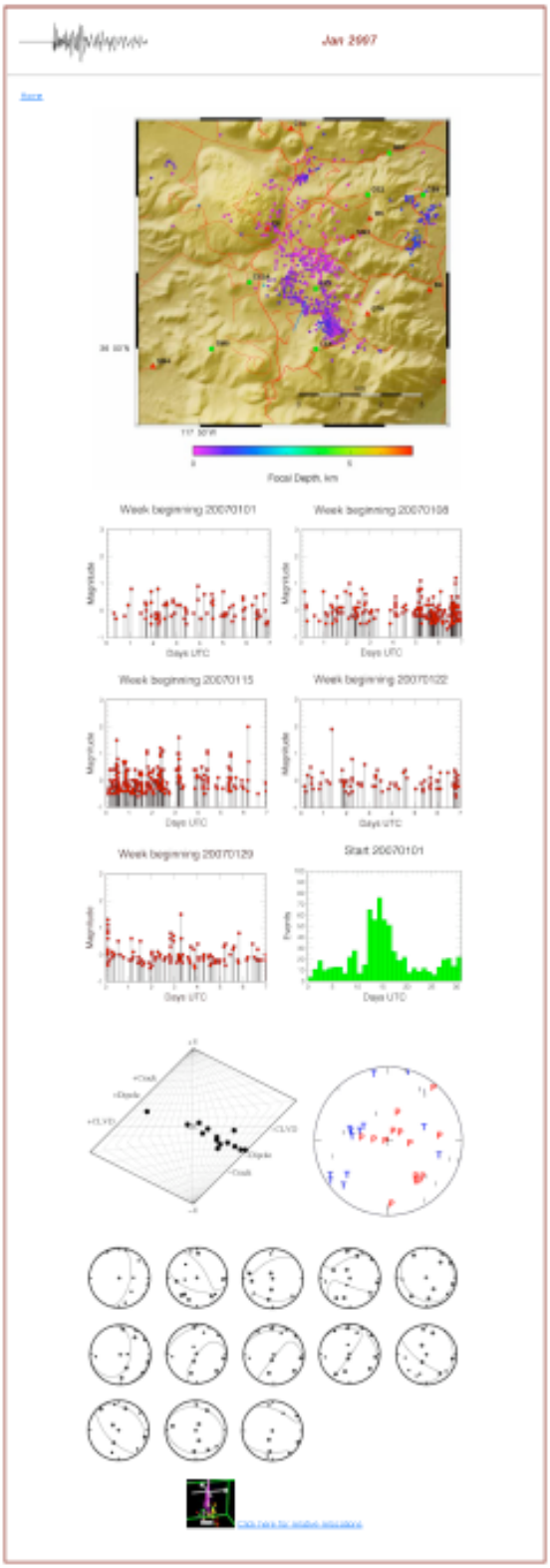

Figure 55: Example of a website sub-page, giving seismic results for January 2007.

3.5.6.2 Analysis of the seismicity in January 2007

3.5.6.2.1 Earthquake time series and magnitudes

The number of earthquakes for each day that occurred within 2 km of the bottom of well 46A-19RD in January 2007 is shown in Figure 56. The typical background was ~ 10 earthquakes per day, but the rate was much higher in the period 13th - 20th January.

Earthquake magnitudes vs. time are shown in Figure 57. Again, the increase in seismic rate in the middle of the month is clear, with particularly high rates during the period 13th - 17th January.

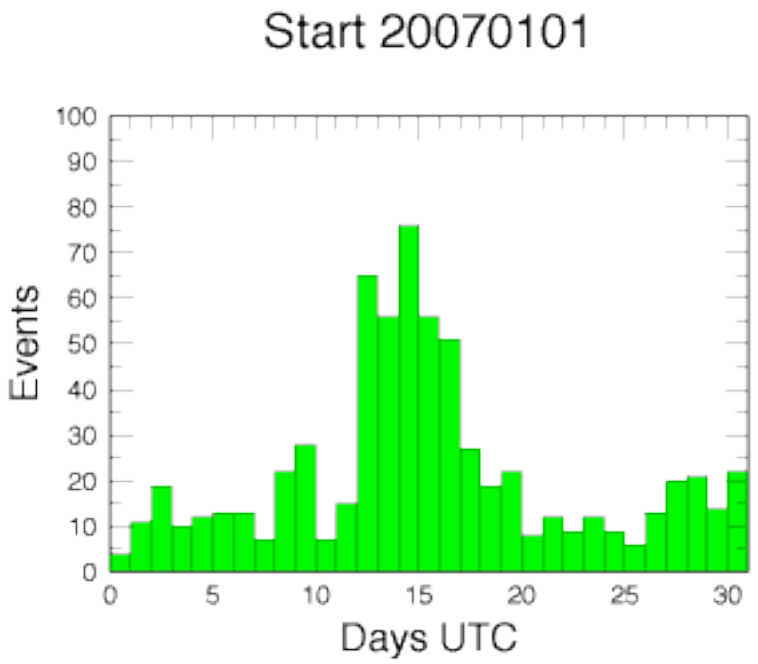

Figure 56: Histogram showing numbers of earthquakes each day within 2 km of the base of well 46A-19RD, for January 2005.

3.5.6.2.2 Earthquake locations

Epicentral locations in the SW part of the geothermal area from the U.S. Navy catalog are shown in Figure 58. Well 46A-19RD itself is in an aseismic region. The densest seismicity forms a NW-trending swathe ~ 1 km north of well 46A-19RD. The bottom of well 46A-19RD extends into this seismogenic zone. This distribution suggests a significant reservoir boundary at this location.

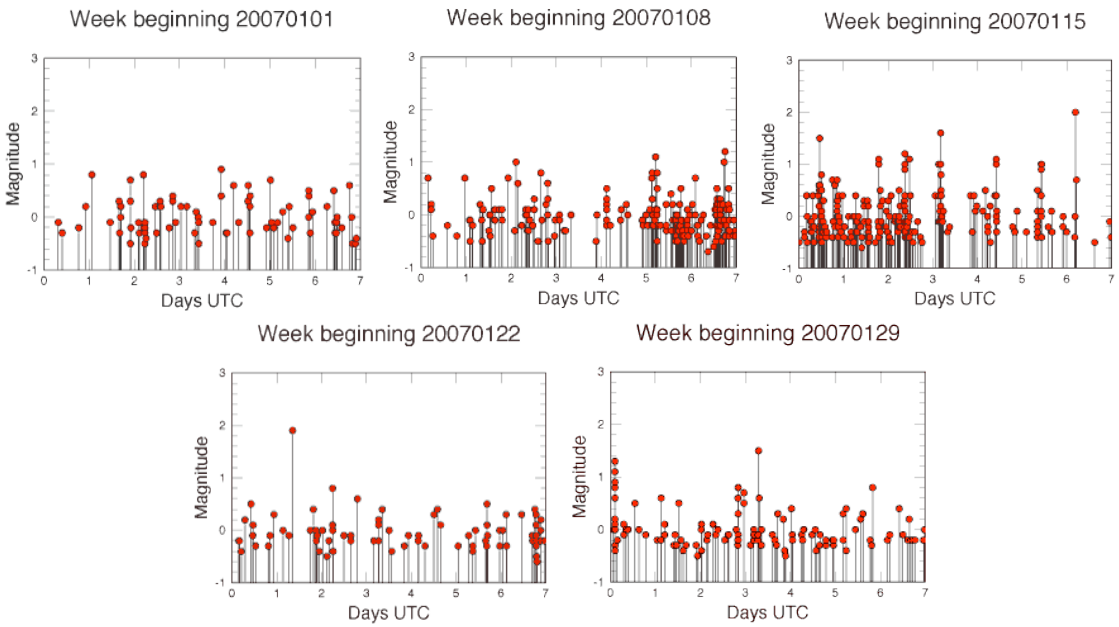

Figure 57: Plots of earthquake magnitude vs. time for January, 2007. A surge of earthquake activity occurred in the period 13th – 17th January.

Earthquakes within 2 km of the base of well 46A-19RD were relocated using program **hypocc** and also using **toonpics** + **hypocc**. The results are shown in Figure 59 in the form of maps and NS vertical sections (i.e., looking from W toward the E). As for the earthquakes studied in the East Flank injection tests, the U.S. Navy catalog locations show the most scatter, significant focusing is achieved by applying **hypocc**, and further increase in the clustering by the use of waveform cross-correlated P- and S-wave arrival times calculated by **toonpics** prior to applying **hypocc**.

The most remarkable feature of the seismicity is the strong deepening of earthquakes toward the south, where they abruptly cease. This zone probably represents the production zone. Well 46A-19RD curves beneath this zone, suggesting that it is well-positioned to introduce fluids beneath the production zone that would likely heat up and rise to replenish the producing reservoir.

Another remarkable feature is the extremely sharp northeastern lower boundary of the seismic zone, most clearly seen in the locations from **hypocc** when viewed toward the NW (Figure 59, middle bottom panel). This also suggests a sharp fault-controlled boundary to the production zone.

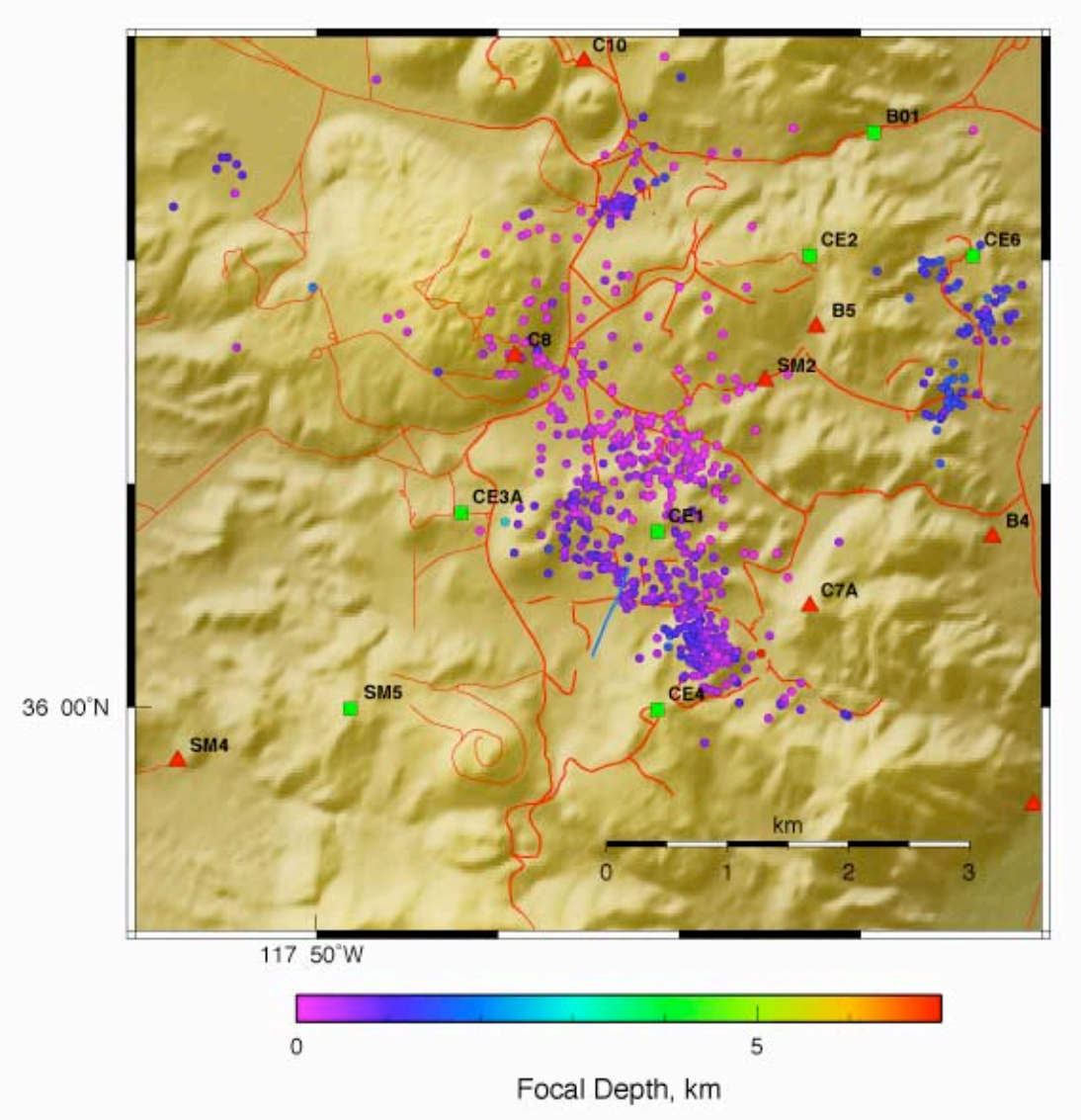

Figure 58: Epicentral map of U.S. Navy earthquake locations for the SW part of the Coso geothermal area for the month of January 2007. Well 46A-19RD is shown as a blue line. Green squares: permanent seismometer stations, red triangles: temporary seismic stations.

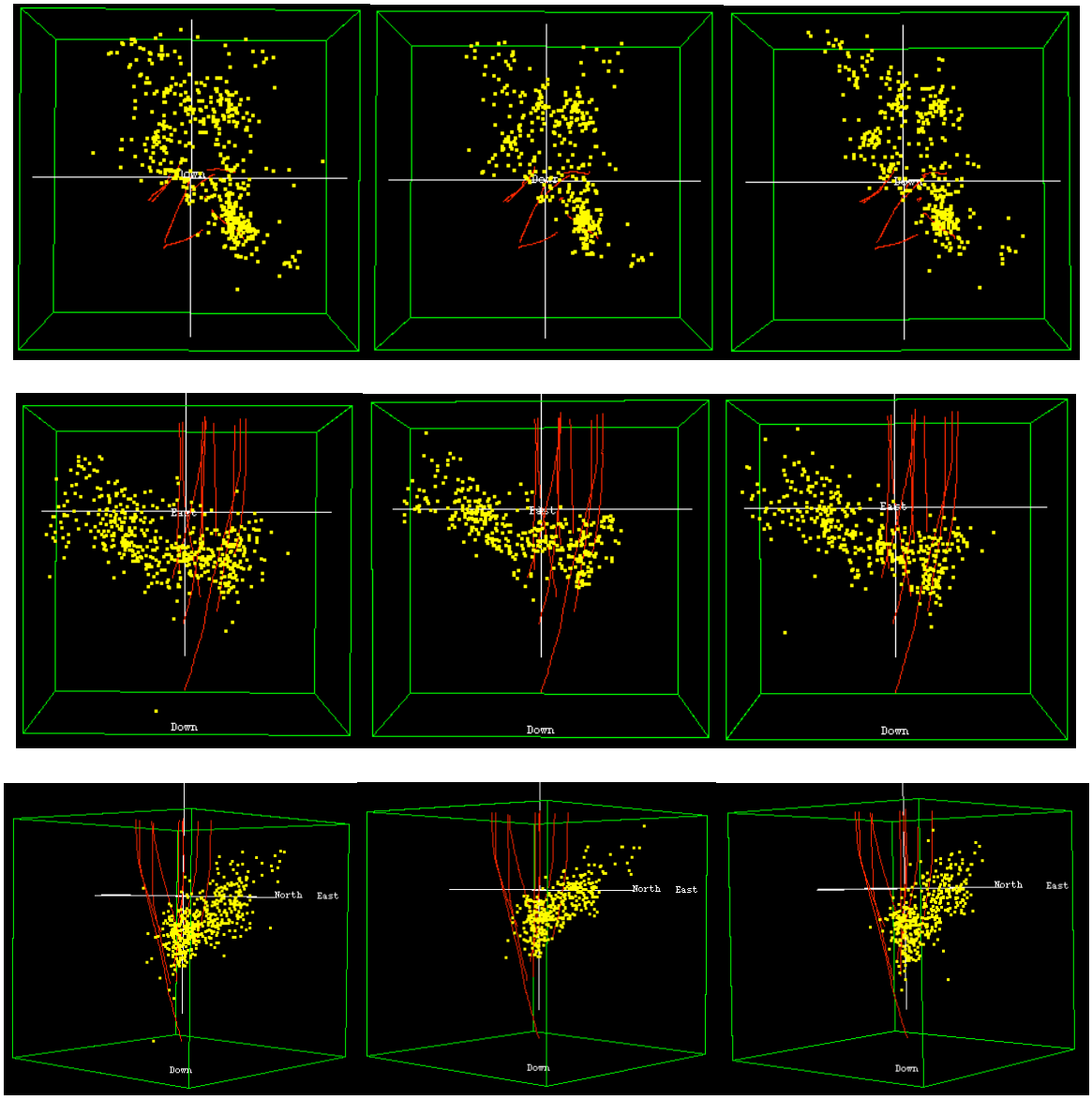

U.S. Navy **hypocc** **toonpics + hypocc**

Figure 59: Locations as screenshots of rotatable 3D plots, for earthquakes within 2 km of the bottom of well 46A-19RD. This well is clearly visible in the middle and lower rows of panels as it is the deepest, and extends beneath the shallower wells further north. The plot is centered on the bottom of this well. Top row: Horizontal maps, middle row: Vertical cross sections rotated so the line of sight is toward the E, bottom row: vertical cross sections looking NW, i.e., along the NW-trending zone of earthquakes that extends into the SE quarter of the horizontal maps. Red lines indicate wells 46-19, 46A-19RD, 72B-19, 33-19, 81-19, 73-19, 33A-19, 16A-20, 74-19, 72A-19RD and 46-19RD. Left panels: U.S. Navy catalog locations, middle panels: **hypocc** locations, right panels: **hypocc+toonpics** locations.

3.5.6.2.3 Moment tensors

Of the 511 earthquakes in the U.S. Navy catalog for January 2007, 116 had 10 or more P-wave arrival time picks, indicating that good moment tensors could potentially be obtained for them. It was not practical to calculate moment tensors for every earthquake in such a large data set, and thus it was decided to focus on the earthquakes that had both large magnitudes and a large number of reported P-wave picks. All earthquakes with magnitudes reported by the U.S. Navy to be > 1.0 were processed, and moment tensors were obtained for 17 (Table 4).

Table 4: Dates, times and qualitative qualities of moment tensors obtained for earthquakes from January 2007, with magnitudes > 1.0 in the U.S. Navy catalog.

date & time	quality of moment tensor
20070108 2314 48	MODERATE
20070110 0230 24	WEAK
20070114 1728 13	GOOD
20070114 1756 49	GOOD
20070115 1110 56	EXCELLENT
20070116 1855 21	MODERATE
20070116 1859 06	MODERATE
20070117 0853 44	WEAK
20070117 0900 29	MODERATE
20070117 0901 16	MODERATE
20070117 0901 26	EXCELLENT
20070117 1125 03	EXCELLENT
20070119 1008 28	EXCELLENT
20070124 0552 39	GOOD
20070129 0222 25	FAIR
20070129 0222 53	WEAK
20070131 2005 28	GOOD

Graphical plots showing details of the data fit are given in Appendix 7. Plots of source type and source orientation are shown in Figure 60. The results are significantly different from those obtained for East Flank earthquakes. The majority of the earthquakes in the region of well 46A-19RD have significant implosive mechanisms. Also, many earthquakes had high-angle T-axes, in contrast with East Flank earthquakes, which tended to have sub-horizontal T axes. This result is consistent with a more compressive stress field around well 46A-19RD than in the East Flank area.

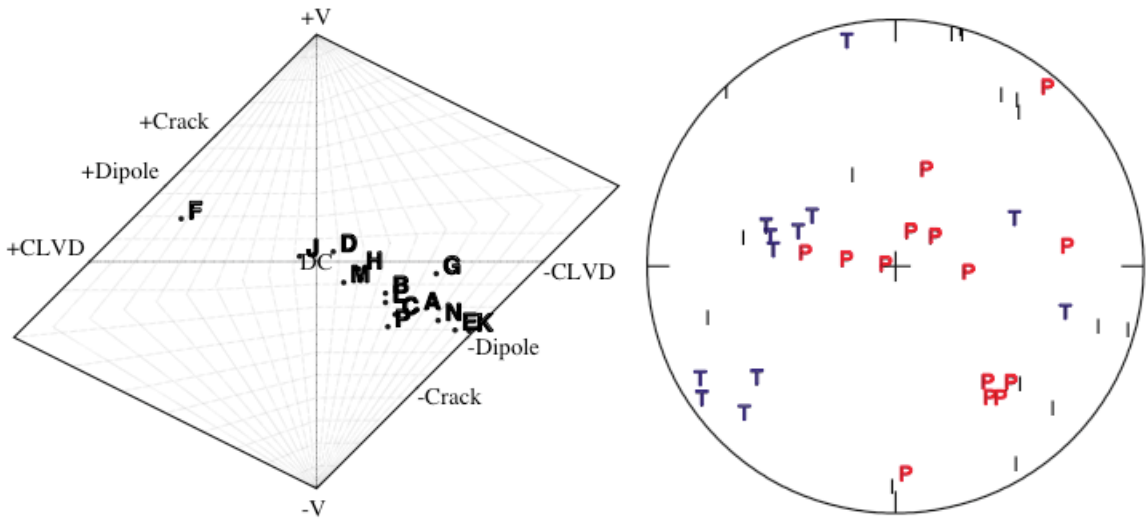

Figure 60: Moment tensors for 17 earthquakes within 2 km of the base of well 46A-19RD, January 2007. Left: Source-type plot. The earthquakes are labeled to denote their time order. Right: Equal-area plot of pressure (P), intermediate (I) and tension (T) axes for the same moment-tensor data set.

3.5.6.2.4 *Discussion*

January 2007 was an unusual month for the Coso geothermal area. Very cold weather there had resulted in icing in nearby plant cooling towers, necessitating stopping production and closing off producing wells for the period 13th - 17th January. It thus seems likely that the surge in seismicity during this period was related to this production shut-in. Many of the surge earthquakes clustered in the NNW-trending seismic zone beneath the single production well to the SE of 46A-19RD. It seems likely that they were induced by rather different processes from the normal background production/injection related events, and thus their characteristics were explored further.

b-values were calculated for the two earthquake populations:

1. 1st - 12th + 18th - 31st January, and
2. 13th - 17th January.

Experiments with rocks in laboratories have shown that *b*-value is inversely proportional to stress. This parameter was thus examined in the expectation that population 2. would have a lower *b*-value, corresponding to an increase in stress in the highly pressured reservoir. The results, shown in Figure 61, show instead that there is no significant difference in the *b*-values for the two populations. The error in slope on a cumulative number vs. magnitude plot is $\pm 1.96b/\sqrt{n}$, yielding an error of $\sim \pm 1.4$ (1σ) in the *b*-values, which depend on ~ 200 earthquakes forming the linear parts of the plots. The slopes of the two populations are statistically the same.

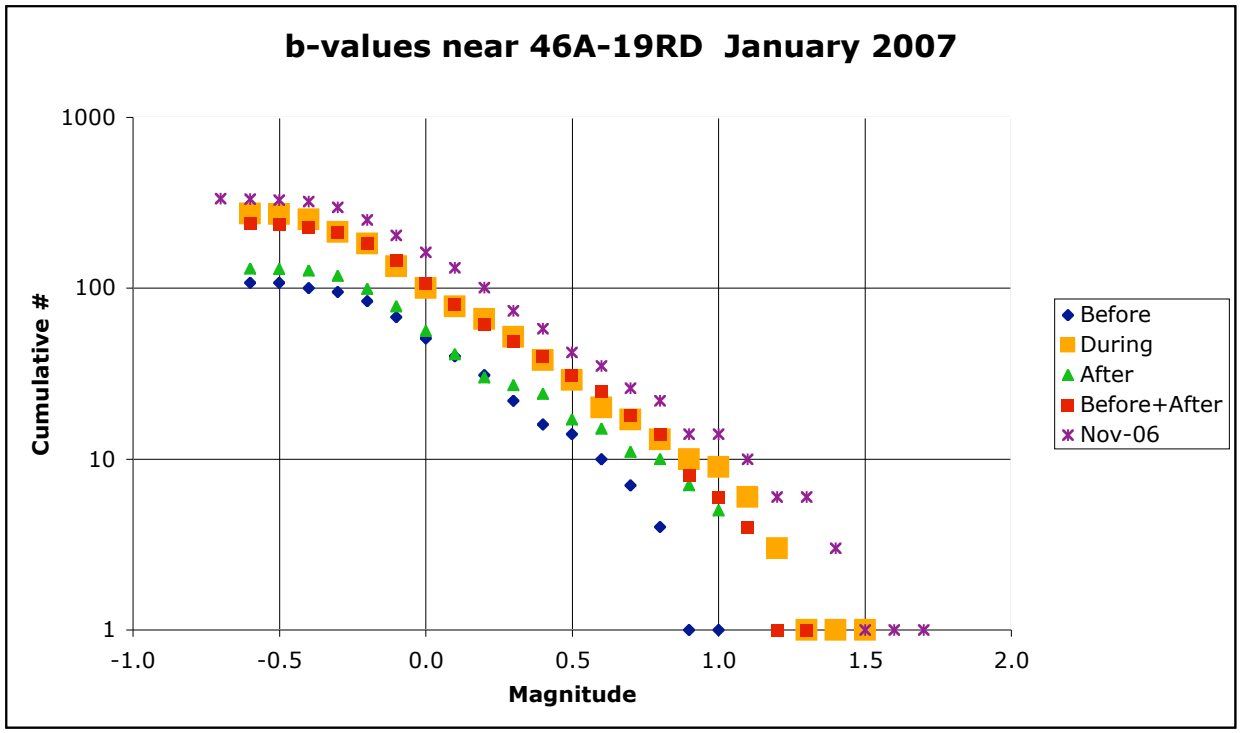

Figure 61: Plots of cumulative number vs. magnitude for earthquakes from January 2007, within 2 km of well 46A-19RD. Before, During, After and Before+After refer to the "shut-in" period 13th - 17th January. *b*-value is the negative slope of the linear part of the curves.

The surge coincided with an increase in pressure in the reservoir, which might intuitively suggest that crack-opening and cavity formation would occur. However, this was not the case. Of the 17 earthquakes for which moment tensors were obtained, 10 occurred in the 5-day surge period. Very surprisingly, there was an unusually large preponderance of implosive components throughout the whole month, indicating that the pressure increase worked to cause cavities to collapse and reduce reservoir permeability. This result has not been explored further as part of the present project. However, this result serves to illustrate that there are still intriguing unanswered questions regarding the processes that govern seismic failure at Coso.

3.5.7 EGS fracture network lifecycles

Data spanning two months before and after the EGS experiment in well 34A-9 in August 2004, and one month before and after the EGS experiment in well 34-9RD2 in March 2005, were processed in order to a) establish the nature of the pre-injection background seismicity, and b) monitor parameters that might have changed during the injection and taken time to return to background afterwards. If such changing parameters could be identified, they would offer the potential for measuring the longevity of the injection effects.

Parameters that were studied were:

1. seismic rate
2. magnitudes
3. locations
4. source type
5. source orientation (i.e., directions of the earthquake P- and T-axes)

During the injection in well 34A-9 in August 2004, the seismic rate increased rapidly and there is evidence that larger that usual magnitude earthquakes occurred towards the end. Earthquakes clustered on an activated fault.

The source types were similar before, during and after injection. The only evidence for modified source characteristics was in the source orientations. The injection induced more strike-slip motion than was typical for pre-injection earthquakes in the area, and there is evidence that this modification of the sense of motion may have persisted for 2 months after injection.

During the injection in well 34-9RD2 in March 2005, the seismic rate increased rapidly and larger earthquakes occurred than were recorded in the weeks before or after. In contrast with the injection in well 34A-9, the co-injection source types were very uniform and comprised a sub-group of the types that occurred before and after the injection. However, there is no evidence that source types after the injection differed significantly from those prior to it. In common with the injection in well 34A-9, there is some evidence that the source orientations following the injection were modified. In this case, however, there was less strike-slip motion after the injection than before.

The work done for the month of January in the vicinity of well 46A-19RD provides an interesting cautionary case history of the variations in seismicity that can occur in response to variations in production activities, in the absence of EGS experiments. There, icing of power-station cooling towers resulted in production-well shut in. This resulted in a transient intense swarm of earthquakes with similar magnitude distribution to the pre- and post-shut-in earthquakes. Source types and source orientations were radically different from any other set studied from Coso, both indicating higher compressional stress than observed elsewhere.

Taken together, the results thus suggest that the most promising earthquake-related parameter that might be measured to monitor the longevity of EGS effects would be highly accurate locations, and source orientation. In order to monitor source orientation effectively, a statistical approach would need to be developed since it is difficult to assess what is statistically significant and what is mere scatter and noise in the results, merely from scrutinising source-orientation plots.

Having said this, a striking aspect about the geothermal seismicity at Coso, and other geothermal areas, is its uniformity of style. Industrial activities, including production and injection, change

most notably the time and place when and where earthquakes occur. Source type and orientation are more strongly controlled by the ambient regional stress. EGS injections can change that stress locally, if injection is conducted under high pressure, but the modification effect on earthquakes may not last very long.

3.5.8 Discussion and consolidation of EGS results

The first EGS experiment, in well 34A-9 in August 2004, went as planned and provided a good case history. It is well supported by background data, including detailed injection data and later tracer tests. The second EGS experiment, in well 34-9RD2, was not so successful since it essentially comprised an unplanned mud-loss event resulting from drilling into massive permeability, rather than a controlled injection. Fewer supporting data are thus available with which to correlate the earthquake results. In particular there are few wellhead injection measurements. A later tracer test did return useful data, however.

The earthquake analyses, including joint interpretation with other data, were able to provide the following information:

1. the locations and orientations of faults activated, thus providing information on the fate of the fluids. In these cases the fluids flowed south, probably along multiple fractures, though one fracture was particularly seismically active during both injections. This suggests that critically stressed faults are likely to be activated by nearby injections, rather than faults that might be closer to the injection site but which are not critically stressed;
2. the sense of motion on the faults. In these cases both crack opening and a combination of right-lateral shear and normal motion was induced;
3. information about the connectivity of fracture networks at depth. There is considerable cross-strike connectivity in the volume studied;
4. understanding of the injection parameters most highly correlated with the induced earthquake activity. The information available suggests that wellhead pressure is most effective in inducing earthquakes, rather than injection rate;
5. ground truthing of other results, including tracer tests and borehole stress measurements.

It is arguable that injection tests should be conducted with the objective of inducing earthquake activity. Earthquakes indicate rock fracturing at depth and are thus direct evidence that fracture networks are being created. When tuning injection wellhead parameters, earthquakes would then not be viewed merely as a convenient by-product that enables monitoring, nor as a potentially dangerous nuisance, but as the means to achieving the objective of the experiment, which is enhanced permeability, injectivity and production. In that case, maintaining high wellhead injectate pressure might be important for achieving the best EGS outcome. An important goal for future research is to discover how to induce myriads of small earthquakes without directly inducing large, potentially damaging events, if this is possible

A recommended EGS microearthquake monitoring application practice can now be proposed. This is based on a large body of work, experimentation, trial and error, rejecting approaches that have been found to be less useful and pursuing those that have been discovered to be more useful. The following is recommended:

1. Near-real-time locations, seismic rates and magnitude time-series;
2. Rapid correlation of seismic rates and magnitude time-series with wellhead injection data. Wellhead pressure may be particularly important, and possibly injection rate;
3. Rapid relative relocations, both with and without waveform cross-correlation of P- and S-waves;
4. Rapid provision of interactively rotatable three-dimensional hypocenter plots;
5. Rapid correlation of locations with local fault maps;
6. Rapid calculation of moment tensors for the largest earthquakes and provision of source-type plots and source-orientation plots;
7. Correlation of trends of relatively relocated hypocenters and moment tensors, to aid interpretation of the moment tensors;
8. Correlation with information on the local orientation of stress axes;
9. Subsequent to the injection, correlation with the results of tracer tests.

3.6 Closing statements

This project provided an excellent opportunity to develop and test several state-of-the-art seismological techniques and software tools that existed previously only in an embryonic state. Several major techniques and software packages are now much more mature and suitable for application to real problems in the field on a timescale that is useful to the industry.

Repeat tomography was demonstrated to be capable of reliably monitoring change in structure of the reservoir with time. This had previously been shown at The Geysers geothermal field. The Coso geothermal field has now provided a second successful case history.

Painstaking and detailed application of the new techniques to two EGS experiments have provided unprecedented tests of the power of earthquake results to provide useful information to underpin EGS stimulation in geothermal areas. Exploration of many approaches, correlations and variations in parameters were explored, which has clarified what is potentially useful and what is unlikely to be helpful. The positive results provide a proof-of-concept that earthquake monitoring can provide information useful to optimizing EGS technology. In the light of the experience gained it has been possible to develop a provisional recommendation for standard industrial field practice for this emerging new technology.

4 Products

4.1 Publications, conference papers and public releases of results.

These products may be accessed via the website http://www.dur.ac.uk/g.r.foulger/.

Colombo, D., G.R. Foulger, L. De Luca and R. Grossi, Integrated analysis of passive and active seismic data in a producing oil field, *68th European Association of Geoscientists & Engineers (EAGE) Conference*, Vienna, Austria, 12-15th June, 2006.

Foulger, G.R., B.R. Julian and F.C. Monastero, Seismic Monitoring of EGS Tests at the Coso Geothermal Area, California, Using Accurate MEQ Locations and Full Moment Tensors, *Thirty-Third Workshop on Geothermal Reservoir Engineering, Stanford University*, Stanford, California, January 28-30, 2008.

Foulger, G.R., B.R. Julian, B.R. and F. Monastero, Seismic monitoring of EGS tests at the Coso Geothermal area, California, using accurate MEQ locations and full moment tensors, *Proceedings, Thirty-Third Workshop on Geothermal Reservoir Engineering, Stanford University*, Stanford, California, January 28-30, SGP-TR-185, 261-268, 2008.

Foulger, G.R., B.R. Julian and F.C. Monastero, Time-dependent Seismic Tomography of the Coso Geothermal Area, 1996-2006, invited paper, *EOS Trans. AGU*, Fall Meet. Suppl., Abstract, 2007.

Foulger, G.R., Is there a free lunch out there? Geothermal energy, its potential and challenges as a renewable, alternative energy resource, invited talk to the Technology and Society Committee (TASC), Santa Clara County, CA, 10 July, 2007.

Foulger, G.R., B.R. Julian and F.C. Monastero, Earthquake characterisation of an artificially stimulated hydraulic fracture at the Coso geothermal area, California, *EOS Trans. AGU*, Fall Meet. Suppl., Abstract, 2006.

Foulger, G.R., Seismic (earthquake) Characterization of EGS Fracture Network Lifecycles, Dept. Energy Program Review meeting, Golden, Colorado, 18th-19th July, 2006.

Julian, B.R., G.R. Foulger and F.C. Monastero, Time-dependent seismic tomography and its Application to the Coso geothermal area, 1996-2006, *Thirty-Third Workshop on Geothermal Reservoir Engineering, Stanford University*, Stanford, California, January 28-30, 2008.

Julian, B.R., G.R. Foulger and F. Monastero, Time-dependent seismic tomography and its application to the Coso geothermal area, 1996-2006, *Proceedings, Thirty-Third Workshop on Geothermal Reservoir Engineering, Stanford University*, Stanford, California, January 28-30, SGP-TR-185, 387-390, 2008.

Julian, B.R., G.R. Foulger and F. Monastero, Earthquake moment tensors from the Coso Geothermal area, *Proceedings, Thirty-Second Workshop on Geothermal Reservoir Engineering, Stanford University*, Stanford, California, January 22-24, SGP-TR-183, 2007.

Julian, B.R., G.R. Foulger and F.C. Monastero, Seismic characterisation of hydraulic stimulation tests at the Coso geothermal area, California, *EOS Trans. AGU*, Fall Meet. Suppl., Abstract, 2007.

Julian, B.R., G.R. Foulger and F. Monastero, Earthquake moment tensors from the Coso Geothermal area, *Thirty-Second Workshop on Geothermal Reservoir Engineering, Stanford University*, Stanford, California, January 22-24, 2007.

Julian, B.R., G.R. Foulger, K. Richards-Dinger and F. Monastero, Time-dependent seismic tomography of the Coso geothermal area, 1996-2004, extended abstract, *Proceedings, Thirty-First Workshop on Geothermal Reservoir Engineering, Stanford University*, Stanford, California, January 30-February 1, 2006.

4.2 Web site

The software developed is freely available via the website ftp://ehzftp.wr.usgs.gov/julian

Results are presented on the password-protected site http://cosomeq.wr.usgs.gov/, hosted by the U.S. Geological Survey.

4.3 Networks and collaborations fostered

Effective working relations have been built with a large group of practitioners and researchers as a result of this project. These include scientists at the Energy and Geoscience Institute, University of Utah, the Geothermal Program Office of the U.S. Navy, Lawrence Livermore National Laboratory, and numerous individuals in industry and foreign universities and institutions. These contacts have been made through attendance of several geothermal conference sessions and meetings and ongoing collaborative work on the Coso project. These new networks have led to current discussions regarding collaborative work on a planned DOE-supported EGS experiment in the Desert Peak geothermal area, Nevada.

4.4 Technologies

Three major software packages have been developed. They are described above under Task 1 and manual pages are given in Appendices 1-4.

4.5 Other products

A huge collection of miscellaneous materials has been collected in the course of this project. This includes a vast database of raw, processed and formatted U.S. Navy earthquake data from the Coso geothermal area, many short programs and scripts for automating data processing and generating specific lists of earthquakes, locations and plots, reference libraries and PowerPoint presentations.

5 References cited

Barker, B. J., et al. (1992), Geysers reservoir performance, in *Monograph on The Geysers Geothermal Field*, edited by C. Stone, pp. 167-177, Geothermal Resources Council, Davis, California.

Davatzes, N., and S. Hickman (2007), Mechanical, mineralogical, andn petrophysical analysis of fracture permeability, in Rose, P. et al., Creation of an Enhanced Geothermal System

through hydraulic and thermal stimulation, DOE progress report for year ending December 31, 2006, 98-154 pp, University of Utah, Salt Lake City.

Duffield, W. A., et al. (1980), Late Cenozoic volcanism, geochronology, and structure of the coso Range, Inyo County, California, *J. geophys. Res.*

Feng, Q., and J. M. Lees (1998), Microseismicity, stress, and fracture in the Coso geothermal field, California, *Tectonophysics*, *289*, 221-238.

Foulger, G. R. (2009), Time-dependent tomography at the Coso geothermal field, *U.S. Geological Survey Open-File Report in preparation*.

Foulger, G. R., et al. (1997), Industrially induced changes in Earth structure at The Geysers geothermal area, California, *Geophys. Res. Lett.*, *24*, 135-137.

Foulger, G. R., et al. (2007), Time-dependent Seismic Tomography of the Coso Geothermal Area, 1996-2006, paper presented at AGU Fall Meeting, American Geophysical Union, San Francisco.

Foulger, G. R., et al. (2003), Tomographic crustal structure of Long Valley caldera, California, and evidence for the migration of CO2 between 1989 and 1997, *J. geophys. Res.*, *108*, 10.1029/2000JB000041.

Gunasekera, R. C., et al. (2003), Four dimensional tomography shows progressive pore-fluid depletion at The Geysers geothermal area, California, *J. geophys. Res.*, *108*, DOI: 10.1029/2001JB000638.

Hudson, J. A., et al. (1989), Source type plot for inversion of the moment tensor, *J. geophys. Res.*, *94*, 765-774.

Julian, B. R. (1986), Analysing seismic-source mechanisms by linear-programming methods, *Geophys. J. R. astron. Soc.*, *84*, 431-443.

Julian, B. R., and G. R. Foulger (1996), Earthquake mechanisms from linear-programming inversion of seismic-wave amplitude ratios, *Bull. seismol. Soc. Am.*, *86*, 972-980.

Julian, B. R., and D. Gubbins (1977), Three-dimensional seismic ray tracing, *J. Geophys.*, *43*, 95-113.

Julian, B. R., et al. (1998), Non-double-couple earthquakes I. Theory, *Rev. Geophys.*, *36*, 525-549.

Monastero, F. C., et al. (2005), The Coso geothermal field: A nascent metamorphic core complex, *Bull. Geol. Soc. Am.*, *117*, 1534-1553.

Rose, P., et al. (2006), Creation of an Enhanced Geothermal System through hydraulic and thermal stimulation, DOE progress report for year ending December 31, 2005, 239 pp, University of Utah, Salt Lake City.

Rose, P., et al. (2005), An EGS stimulation experiment under low wellhead pressures, paper presented at Thirtieth Workshop on Geothermal Reservoir Engineering, Stanford University, Stanford, California, January 31-February 2.

Shook, G. M., and J. H. Forsman (2005), Tracer interpretation using temporal moments on a spreadsheet, INL Report INL/EXT-05-00400.

Unruh, J. R., et al. (2002), Seismotectonics of the Coso Range—Indian Wells Valley region, California: Transtensional deformation along the southeastern margin of the Sierran microplate, in *Geological evolution of the Mojave Desert and Southwestern Basin and Range*, edited by A. F. Glazner, et al., Geological Society of America, Boulder, CO.

Waldhauser, F., and W. L. Ellsworth (2000), A double-difference earthquake location algorithm: Method and application to the northern Hayward Fault, California, *Bull. seismol. Soc. Am.*, *90*, 1353-1368.

William Lettis & Associates, I. (2004), Mapping and Characterization of Neotectonic Structures in a Releasing Stepover, Northern Coso Range, Eastern California, Final Technical Report prepared for the Geothermal Program Office, Naval Air Warfare Center, China Lake, CA under contract N68936-02-C-0208., 54 pp, Walnut Creek, California.

6 Appendices

*6.1 Appendix 1: **cat2dt** manual page*

NAME

cat2dt – Generate time-difference data from earthquake catalogs

SYNTAX

cat2dt [*option...*] [*catalog_file...*]

DESCRIPTION

cat2dt reads earthquake catalog data (event locations and seismic-wave arrival times) from the speciTed *catalog_file*s (standard input default), generates time-difference data of the type needed by the program **hypocc**(1Q), and writes them to user-speciTed Tles. It also writes a summary of its activity to standard output.

OPTIONS

The following command-line *option*s control **cat2dt**. They are read Trst from the Tle **.cat2dtrc** if it exists, otherwise from **$HOME/.cat2dtrc**, if it exists, and then from the command line. In any case, options given on the command line override those from startup Tles. Options are scanned from left to right; if they conTict, the last ones scanned have effect. Only enough characters are needed to uniquely identify an *option*.

-help [*pattern...*]
Print brief explanations of all options matching the given *pattern*s on the standard error output. If no *pattern*s are given, explain all options.

-ignore *file*
Read a list of event keys from the named *file* (free format) and ignore these events and do not read in or process any data from them. See also the **-wanted** option, below.

-maxdist *d*
Ignore seismic-wave observations ("picks") from stations whose epicentral distance exceeds *d* (default: **500.0**).

-maxnabor *n*
Connect an event to at most *n* other ("neighbor") events (default: **10**).

-maxobs *n*
Connect each event pair by at most *n* time-difference data (default: **50**). If more data exist, those for the *n* closest statons (measured from the centroid of the evnts) are used.

-maxsep *d*
Do not connect events that are separated by more than the distance *d* (default: **10.0**).

-minlinks *n*
Connect an event pair only if the events have at least *n* time-difference observations (default: **8**).

-minweight *value*
Ignore data with weights less than *value* (default: **0.0**). Negative weights are regarded as special cases, indicating data of unusual importance because of the event and station geometry, and such data are kept, regardless of *value*.

-outfile *file*
Write generated time-difference data to *file* (default: **dt.ct**).

-radius *value*
Set the radius of the planet to *value* (default: **6371.2**).

-station *file*
Read the locations of seismic stations from the named *file* (Default: **station.dat**). See **STATION-FILE FORMAT**, below.

-tolerance *time_interval*
When identifying outlier data, use the speciTed *time_interval* as the tolerance. Time differences are regarded as outliers, and ignored, if their absolute value exceeds the hypocentral separation divded by the wave speed by the amount *time_interval* or more (default: **0.5**). See the **-vfocus** option, below.

-vfocus *Vp Vs*
When testing for outlier data, use *Vp* and *Vs* as the hypocentral compressional- and shear-wave speeds (default: **5.0 2.9**). See the **-tolerance** option, above.

-wanted *file*
Read a list of event keys from the named *file* (free format) and read only these events from the event file. If this option is not given, all the events in the event file are read and processed. See also the **-ignore** option, above. The **-ignore** option takes precedence over this option; if an event appears in both, it is ignored.

CATALOG-FILE FORMAT

Each input *catalog_file* contains one or more events, each of which consists of an event line, followed by any number of reading lines.

An event line begins with a percent-sign (%) character, followed by the date, time, latitude, longitude, and depth, in that order, in free format. The last field on the event line is the event key, which is a character string of maximum length 11. Any fields between the focal depth and the event key are ignored. Latitudes and longitudes are in degrees, and may include optional minutes and seconds fields delimited by colons. North latitude and east longitude are positive. For example, these are (equivalent) legal event lines:

% 19840101 21435050 37.3327 -121.6993 7.980 1.1 0.20 0.60 0.00 391
% 19840101 21435050 37.3327 -121.6993 7.980 391
% 19840101 21435050 37:19.962 -121.:41.958 7.980 391
% 19840101 21435050 37:19:57.72 -121:41:57.48 7.980 1.1 0.20 0.60 0.00 391

Each reading line contains the station code, travel time, weight, and phase code, in free format. Weights should be inversely proportional to the squares of the estimated uncertainties of the arrival times. Negative weights are regarded as indications that data are unusually important because of the event-station geometry. Such data are excluded from testing specified by the **-minweight** option, and the signs of their weights are otherwise ignored. Example reading lines:

NCCCO 1.460 -0.500 P
NCCMH 2.680 0.200 P
NCCAO 2.720 -1.000 P
NCCAO 4.850 0.100 S
NCCAD 3.330 1.000 P

STATION-FILE FORMAT

Each line of a station file corresponds to one station, and contains the station code (maximum 7 characters), the latitude, the longitude, and optionally the elevation, in free format. Latitudes and longitudes are in degrees, and may include optional minutes and seconds fields delimited by colons. North latitude and east longitude are positive. Example station lines:

NCAAR 39.275936 -121.026962
NCAAR 39.275936 -121.026962 1.234
NCAAR 39:16.55616 -121:01.61772 1.234
NCAAR 39:16:33.37 -121:01:37.06 1.234

MEASUREMENT UNITS

All angles (station and earthquake latitudes and longitudes) are measured in degrees. The default values associated with the **-maxdist**, **-maxsep**, **-radius**, **-tolerance**, and **-vfocus** options are based on assumed distance and time units of kilometers and seconds, but the user is free to change these values and use any consistent system of units.

FILES

dt.ct	default output file (option **-dtfile**).
event.dat	default output earthquake list (option **-evfile**).
station.dat	default input seismometer-station list (option **-station**).

EXAMPLES

To...

SEE ALSO

Waldhauser, Felix, and William L. Ellsworth, A double-difference earthquake location algorithm: Method and application to the northern Hayward fault, California, Bull. Seismol. Soc. Amer., v. 90, no. 6, pp. 1353-1368, 2000.

Waldhauser, Felix, hypoDD - A Program to Compute Double-Difference Hypocenter Locations, USGS Open-Ṭle Report 01-113, 2001. http://geopubs.wr.usgs.gov/open-Ṭle/of01-113/

hypocc(1Q) – simultaneously locate clusters of earthquakes

toonpics(1Q) – adjust seismic arrival-time picks by comparing digital seismograms

DIAGNOSTICS

AUTHOR

Bruce R. Julian, USGS Menlo Park, Calif. (julian@usgs.gov) after program **ph2dt** of Waldhauser & Ellsworth (2000).

*6.2 Appendix 2: **toonpics** manual page.*

NAME

toonpics – adjust seismic arrival-time picks by comparing digital seismograms

SYNTAX

toonpics [*-option...*] *event_code...*

DESCRIPTION

toonpics modiṪes seismic-wave measurements ("picks"), by comparing portions of AH-format digital seismograms, adjusting ("tuning") the arrival times so that the waveforms match as well as possible.

For each *event_code* on the command line, there must exist an ASCII "listṪle", named *event_code***.list**, which speciṪes the locations of the seismogram Ṭles, and a binary "pickṪle", named *event_code***.ep**, which contains the picks that are to be adjusted. (An alternate sufṪx for the pickṪles can be speciṪed using the **-picktype** option, described below.) Any **.ep** or **.list** extensions already present in the *event_code*s given on the command line are ignored. PickṪles can be generated n a variety of ways, for example using an interactive seismogram-analysis program such as **epick**(1Q), using the automatic program **autopick**(1Q), or by converting data from other formats. Picks are read through a UNIX Ṭlter program (see the **-pfilter** option, below), to facilitate conversion between formats. See **epick**(1Q) for a description of the listṪle format.

toonpics has two modes of operation, depending on how many *event_code*s are speciṪed:

Teleseism Mode (single *event_code*)

This is the simpler mode, and is is appropriate when the waveforms at different stations are similar, as when a distant earthquake is recorded on a small array. **toonpics** compares seismograms from all possible pairs of stations and uses the results to adjust the pick times. In this mode **toonpics** writes modiṪed picks to a Ṭle of the same (**epick**(1Q)) format, named *event_code***.tp**. Picks are written through a UNIX Ṭlter program (see the **-pfilter** option, below), to facilitate conversion between formats.

Local-earthquake Mode (multiple *event_code*s)

This mode is appropriate when the waveforms for many earthquakes are similar at each station but the waveforms at different stations differ, for example when tightly clustered earthquakes are recorded by a local network. For each station and channel, **toonpics** compares seismograms from all possible pairs of earthquakes and uses the results to adjust the pick times. It writes the results to its standard output, in the "Correlation Data" format of the **hypocc**(1Q) command.

OPTIONS

The following command-line *option*s control **toonpics**. Options are scanned from left to right; if they conṪict, the rightmost ones take effect. Only enough characters are needed to uniquely identify an *option*.

-help [*pattern ...*]

Print brief explanations of all options matching the given *pattern*s on the standard error output. If no *pattern*s are given, explain all options.

-case Distinguish between upper- and lower-case letters in station codes. By default, case is ignored.

-dtfile *file*

Write computed picks for Local-Earthquake mode to the named *file* (default: **dt.cc**).

-lineup *base_path*

Generate AH-format Ṭles of aligned windowed digital seismograms. Each Ṭle contains the windowed portions of all the seismograms from one station, and has the name *base_path***.***station_code***.ah**. The start time for the Ṭrst seismogram is correct; all other seismograms are shifted using the computed arival-time differences to make all the arrival times equal.

-lowpass *frequency*

Low-pass Ṭlter the seismograms, using the speciṪed corner *frequency* (Hz), before cross-correlating them.

-pfilter *input output*

Read in pick Ṭles in through the UNIX Ṭlter **input**, (both modes) and write them through the Ṭlter **output** (Teleseism Mode only) (defaults for both: **/bin/cat**). The use of Ṭlters facilitates the

handling of different pickṬle formats.

-phase *code*
Adjust the picks for seismic phase *code* (for example, **P**, **S**, **Pg**). This option may be repeated as many times as necessary to specify all desired phases.

-picktype *suffix*
Read picks from Ṭles with the speciṬed *suffix* (default: **.ep**).

-station *start n*
When a station code is longer than four characters, use a shortened code consisting of only the *n*-character substring starting at position *start*. This option allows ṭexibility in dealing with the snafu caused by station codes that will not Ṭt into the current pickṬle format. By default, *start* = **1** and *len* = **4** (the Ṭrst four characters are used). We intend to modify the format soon, to eliminate this problem (and this option).

-weight *exponent*
Apply weights to the time-difference estimates in porportion to their correlation coefṬcients raised to the power *exponent* (default: **2**). An *exponent* of zero causes all estimates to be weighted equally. Higher *exponent*s cause more severe down-weighting of estimates from poorly correlated signals.

-window *lead length*
Correlate portions of seismograms that begin *lead* seconds before the pick time (default: **0.03**) and are *length* seconds long (default: **0.1**).

SEE ALSO

autopick(1Q) – Automatically measure seismic phases on digital seismograms
epick(1Q) – Interactive seismogram analyzer
hypocc(1Q) – Simultaneously locate clusters of earthquakes using differential arrival-time dat

AUTHORS

Bruce R. Julian, USGS Menlo Park, Calif.

*6.3 Appendix 3: **hypocc** manual page.*

NAME

hypocc – Simultaneously locate clusters of earthquakes using differential arrival-time data

SYNTAX

hypocc [*option...*] [*file*]

DESCRIPTION

hypocc reads differential seismic-wave arrival-time data for a collection of earthquakes from the speciTed *file* (standard input default), computes origins (hypocenters and origin times) that best Tt these data, and writes the results to various Tles. It reads other needed information such as initial event origins, seismometer station locations, and a regional Earth model, from user-speciTed Tles (see the **-event**, **-station**, and **-model** options, below.) **hypocc** also writes a summary of its actions to its standard output, and optionally writes a more detailed summary to a user-speciTed log Tle (see the **-log** option.)

hypocc uses the method of Waldhauser and Ellsworth [2000], which is sensitive to the relative locations of nearby events. It can therefore well resolve small-scale details of the seismicity distribution. Although **hypocc** is functionally similar to the program **hypoDD** [Waldhauser, 2001], it uses more efTcient algorithms and incorporates many bug Txes. Its input formats are upward compatible with those of **hypoDD**.

hypocc supports two different data formats, one for data derived from earthquake catalogs and one for data measured by waveform correlation. The two formats (and data types) may be interspersed.

Differential arrival-time data suitable for input to **hypocc** can be generated from conventional earthquake data catalogs using the **cat2dt (1Q)** command, or more accurately by cross-correlation of digital seismograms using the **toonpics (1Q)** command.

OPTIONS

The following command-line *option*s control **hypocc**. They are read Trst from the Tle **.hypoccrc** if it exists, otherwise from **$HOME/.hypoccrc**, if it exists, and then from the command line. In any case, options given on the command line override those from startup Tles. Options are scanned from left to right; if they conTict, the last ones scanned have effect. Only enough characters are needed to uniquely identify an *option*.

-help [*pattern ...*]
Print brief explanations of all options matching the given *pattern*s on the standard error output. If no *pattern*s are given, explain all options.

-damping *value*
Use the given *value* (default: **1.0**) as the initial numerical damping factor in solving the design equations by least-squares.

-ddemulate
This option is provided for backward compatability, and emulates the behavior of the **hypoDD** program when reading in cross-correlation time-difference data by assuming that the time differences have been corrected for the difference in event origin times. See **Correlation Data** under **FORMATS**, below.

-event *file*
Read initial origins for the earthquakes from the named *file* (Default: **event.dat**). See **FORMATS**, below.

-ignore *file*
Read a list of event keys from the named *file* (free format) and ignore these events and do not process any data from them. See also the **-wanted** option, below.

-log *file* Write detailed information about program execution to the named *file*.

-maxdist *distance*
Use data from only those seismic stations within the given *distance* of the centroid of the initial event locations given in the event Tle.

-maxiter number

Perform at most *number* iterations (default: **5**). (An iteration involves relocating all the earthquakes in a cluster.) If *number* is zero, then travel times, residuals, etc. are computed for the initial origins only, and the origins are not changed.

-maxsep *distance*

Connect events in clusters only if their epicenters are separated by less than *distance*. Of course, event pairs can be connected only if time-difference data are present in the input data *file*.

-minclust *number*

Do not process clusters conatining fewer than *number* events (Default: **10**).

-model *file*

Read the Earth model from the named *file* (Default: **model.dat**). See **libttplyr**(4) for a description of the format.

-mu *value*

output *file*

-phase *code*

Use data for the seismic phase *code* (for example, **P**, **S**, **Pg**). This option may be repeated as many times as necessary to specify all desired phases.

-rmstol *factor*

Print a warning message whenever the computed RMS residual exceeds by the given *factor* (default: **1.1**) the value predicted from the linearized design equations. This occurrence is caused by nonlinearity in the true design equations, and may be caused by poor starting locations or inadequate numerical damping (see the **-damping** option).

-scale *factor*

Scale the variables using the speciṬed *factor*, (default: **0.1**) to improve the condition number of the design equations. This action is equivalent to dividing the time unit by *factor* (Time/Length), in order to make the values in different columns of the design matrix similar in magnitude.

-station *file*

Read the locations of seismic stations from the named *file* (Default: **station.dat**). See **FORMATS**, below.

-wanted *file*

Read a list of event keys from the named *file* (free format) and read only these events from the event Ṭle. If this option is not given, all the events in the event Ṭle are read and processed. See also the **-ignore** option, above. The *-ignore* option takes precedence over this option; if an event appears in both, it is ignored.

FORMATS

Event file

Each line corresponds to one event, and contains the date, time, latitude, longitude, and depth, in that order, in free format. The last Ṭeld on the line is the event key, which is a character string of maximum length 14. Any Ṭelds between the focal depth and the event key are ignored. The seconds Ṭeld begins at the Ṭfth character of the origin-time Ṭeld and is two or more characters in length. If it does not contain a decimal point, one is assumed after the second character. Latitudes and longitudes are in degrees, and may include optional minutes and seconds Ṭelds delimited by colons. North latitude and east longitude are positive. For example, these are (equivalent) legal event lines:

19840101 21435050 37.3327 -121.6993 7.980 1.1 0.20 0.60 0.00 391
19840101 214350.50 37.3327 -121.6993 7.980 391
19840101 21435050 37:19.962 -121.:41.958 7.980 391
19840101 21435050 37:19:57.72 -121:41:57.48 7.980 1.1 0.20 0.60 0.00 391

Station File

Each line corresponds to one station, and contains the station code (maximum 7 characters), the latitude, the longitude, and optionally the elevation. Latitudes and longitudes are in degrees, and may include optional minutes and seconds Ţelds delimited by colons. North latitude and east longitude are positive. Example station lines:

NCAAR 39.275936 -121.026962
NCAAR 39.275936 -121.026962 1.234
NCAAR 39:16.55616 -121:01.61772 1.234
NCAAR 39:16:33.37 -121:01:37.06 1.234

Earth Model

See **libttplyr**(4).

Earthquake-Catalog Data

Data from each event pair begin with a line consisting of a percent sign (**%**) followed by the event keys of the two events, corresponding to the keys in the event Ţle. This line is followed by any number of lines, each of which gives a station code, the travel times of a seismic phase from the two events to this station (relative to the origin times in the event Ţle), a weight, and the phase code.

The weights should be inversely proportional to the *squares* of the expected observational errors (sigmas). The expected error in a difference is the square root of the sum of the squares of the individual errors. Many commonly used seismological computer programs compute weights incorrectly.

Example:

% 1 104
NV2 1.512 1.282 1.0000 P
NV2 2.472 2.202 1.0000 S
NV3 1.836 1.906 1.0000 P
NV5 2.236 2.258 1.0000 P
NV10 2.724 2.558 1.0000 P
CE2 2.836 2.774 1.0000 P
CE2 4.760 4.626 1.0000 S
NV6 6.072 5.898 1.0000 S
NV6 3.628 3.418 1.0000 P

Correlation Data

Data from each event pair begin with a line consisting of a percent sign (**%**) followed by the event keys of the two events, corresponding to the keys in the event Ţle, followed by an "origin-time correction". This line is followed by any number of lines, each of which gives a station code, the difference in the travel times of a seismic phase from the two events to this station (typically a large number, possibly in the tens of millions), a weight, and the phase code.

The "origin-time correction" should usually be zero (but must be present to distinguish between formats.) It is a historical artifact that was intended to deal with time differences that have been adjusted for origin times using incorrect values. Because arrival-time differences can be measured without regard to origin times, there is no need to adjust for origin times, or to correct erroneous adjustments. See the **-ddemulate** option, above.

Note the discussion of weights under **Earthquake-Catalog Data**, above.

Example:

```
% 20040806211259 20040806203508 0.0000
B01   2271.0086     0.308  P
CE2   2271.0025     0.649  P
NV4   2270.9848     0.286  P
CE4   2270.9532     0.342  P
NV5   2270.9966     0.343  P
NV6   2270.9813     0.211  P
```

FILES

.hypoccrc	startup file, containing options as described above.
$HOME/.hypoccrc	startup file if **.hypoccrc** is not found.
station.dat	default input station file
event.dat	default input event file
model.dat	default input Earth-model file
hypocc.reloc	default output origin file

EXAMPLES

To...

SEE ALSO

Waldhauser, Felix, and William L. Ellsworth, A double-difference earthquake location algorithm: Method and application to the northern Hayward fault, California, Bull. Seismol. Soc. Amer., v. 90, no. 6, pp. 1353-1368, 2000.

Waldhauser, Felix, hypoDD - A Program to Compute Double-Difference Hypocenter Locations, USGS Open-file Report 01-113, 2001. http://geopubs.wr.usgs.gov/open-file/of01-113/

cat2dt(1Q) – compute differential arrival times from a conventional earthquake data catalog
qloc(1Q) – locate earthquakes one at a time
libttplyr(4) – body-wave travel-time library for plane-layered Earth models
toonpics(1Q) – compute differential arrival times by waveform cross-correlation

DIAGNOSTICS

AUTHOR

Bruce R. Julian, USGS Menlo Park, California, after the program **hypoDD** of Waldhauser & Ellsworth (2000).

*6.4 Appendix 4: **dtomo** manual page*

NAME

dtomo – Time-dependent local-earthquake tomography

SYNTAX

dtomo [*-option...*] [*file...*]

DESCRIPTION

dtomo inverts sets of seismic-wave arrival times from earthquakes as observed on a local network of seismometers to derive three-dimensional models of seismic-wave speed variations at different epochs. It uses algorithms that seek agreement between models for different epochs, so that difference in derived models are likely to reflect actualy structural changes, rather than artifacts of statistical noise or variations in earthquake or station distributions.

dtomo reads data from files specified by the command-line options **-quakes**, **-blasts**, and **-shots**, described below, and writes results to its standard output.

OPTIONS

The following command-line *option*s control **dtomo**. They are read first from the file **.dtomorc** if it exists, otherwise from **$HOME/.dtomorc**, if it exists, and then from the command line. In any case, options given on the command line override those from **.dtomorc** files. Options are scanned from left to right; if they conflict, the last ones scanned take effect. Only enough characters are needed to uniquely identify an *option*.

-help [*pattern ...*]
Print brief explanations of all options matching the given *pattern*s on the standard error output. If no *pattern*s are given, explain all options.

-accuracy *d*
In numerical ray-tracing computations, strive for an accuracy in the paths of *d* km (default: **0.001**).

-blasts *file*
Read arrival-time data for blasts (events with known locations but unknown times) from the specified *file*, in the format of the **simulps12** command (Evans et al., 1994).

-maxiter *number*
Perform at most *maxiter* iterations, in each of which the event locations and the structural model are perturbed (default: **10**). If *maxiter* equals zero, then **dtomo** computes epicentral distances, theoretical arrival times, etc. for the initial locations and model, without doing any perturbations.

-pmodel *file*
Read the initial model of the compressional-wave speed, Vp, from *file* (default: **dtomo_p.m3d**). This must be an ASCII file in the input format used by the **mkmdl3d**(1Q) command.

-quakes *file*
Read arrival-time data for earthquakes (events with unknown locations and times) from the specified *file*, in the format of the **simulps12** command (Evans et al., 1994).

-rayseg *d*
In numerical ray-tracing computations, divide each ray into segments approximately *d* km long (default: **0.2**).

-shots *file*
Read arrival-time data for shots (events with known locations and times) from the specified *file*, in the format of the **simulps12** command (Evans et al., 1994).

-smodel *file*
Read the initial model of the shear-wave speed, Vs, from *file* (default: **dtomo_s.m3d**). This must be an ASCII file in the input format used by the **mkmdl3d**(1Q) command.

-station *file*
This option is required. It specifies the *file* (default: **dtomo.sta**) giving seismometer coordinates. This is an ASCII file, with each line giving the station code, latitude (degrees), longitude (degrees), and elevation (km), in free format. Any fields beyond the elevation are ignored.

MEASUREMENT UNITS

All angles, such as station and event latitudes and longitudes, are measured in degrees. The default values associated with the **-accuracy** and **-rayseg** options are based on assumed distance units of kilometers, but the user is free to change these values and the model files (options **-pmodel** and **-smodel**) to use any consistent distance unit.

SEE ALSO

mkmdl3d(1Q) – generate regional three-dimensional seismic-wave models

Evans, J. R., D. Eberhart-Phillips, and C. Thurber (1994), User's manual for SIMULPS12 for imaging Vp and Vp/Vs, a derivative of the Thurber tomographic inversion SIMUL3 for local earthquakes and explosions, 142 pp, Open-File Report 94-431, U.S. Geological Survey.

AUTHOR

Bruce R. Julian, USGS Menlo Park, Calif.
julian@usgs.gov

6.5 Appendix 5: Details of the moment tensor results: well 34A-9.

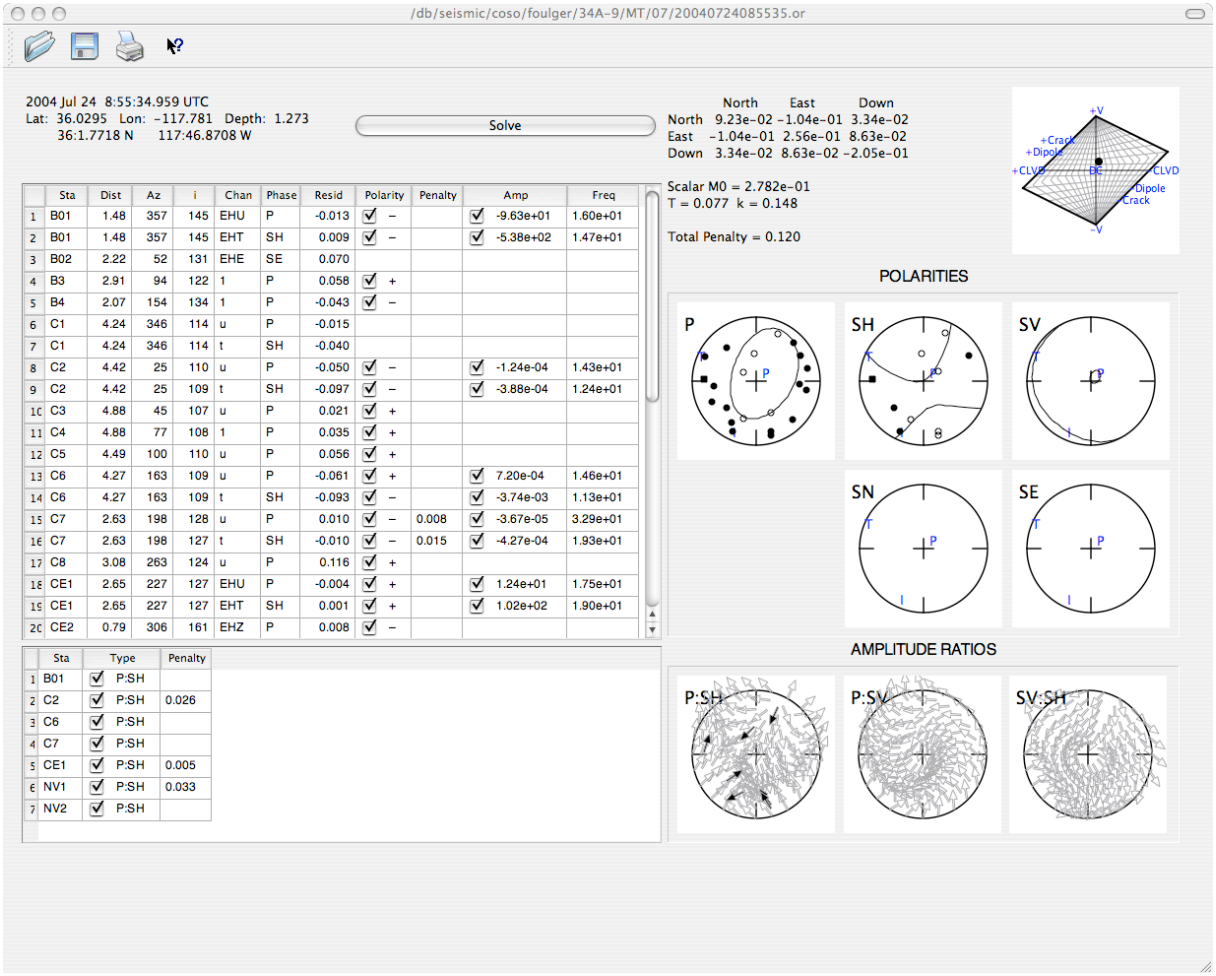

	Sta	Dist	Az	i	Chan	Phase	Resid	Polarity	Penalty	Amp	Freq
1	B01	1.48	357	145	EHU	P	-0.013	–		-9.63e+01	1.60e+01
2	B01	1.48	357	145	EHT	SH	0.009	–		-5.38e+02	1.47e+01
3	B02	2.22	52	131	EHE	SE	0.070				
4	B3	2.91	94	122	1	P	0.058	+			
5	B4	2.07	154	134	1	P	-0.043	–			
6	C1	4.24	346	114	u	P	-0.015				
7	C1	4.24	346	114	t	SH	-0.040				
8	C2	4.42	25	110	u	P	-0.050	–		-1.24e-04	1.43e+01
9	C2	4.42	25	109	t	SH	-0.097	–		-3.88e-04	1.24e+01
10	C3	4.88	45	107	u	P	0.021	+			
11	C4	4.88	77	108	1	P	0.035	+			
12	C5	4.49	100	110	u	P	0.056	+			
13	C6	4.27	163	109	u	P	-0.061	+		7.20e-04	1.46e+01
14	C6	4.27	163	109	t	SH	-0.093	–		-3.74e-03	1.13e+01
15	C7	2.63	198	128	u	P	0.010	–	0.008	-3.67e-05	3.29e+01
16	C7	2.63	198	127	t	SH	-0.010	–	0.015	-4.27e-04	1.93e+01
17	C8	3.08	263	124	u	P	0.116	+			
18	CE1	2.65	227	127	EHU	P	-0.004	+		1.24e+01	1.75e+01
19	CE1	2.65	227	127	EHT	SH	0.001	+		1.02e+02	1.90e+01
20	CE2	0.79	306	161	EHZ	P	0.008	–			

	Sta	Type	Penalty
1	B01	P:SH	
2	C2	P:SH	0.026
3	C6	P:SH	
4	C7	P:SH	
5	CE1	P:SH	0.005
6	NV1	P:SH	0.033
7	NV2	P:SH	

Figure A5a. Screenshot of **eqmec** output showing an example pre-injection earthquake moment tensor solution (M = 1.1).

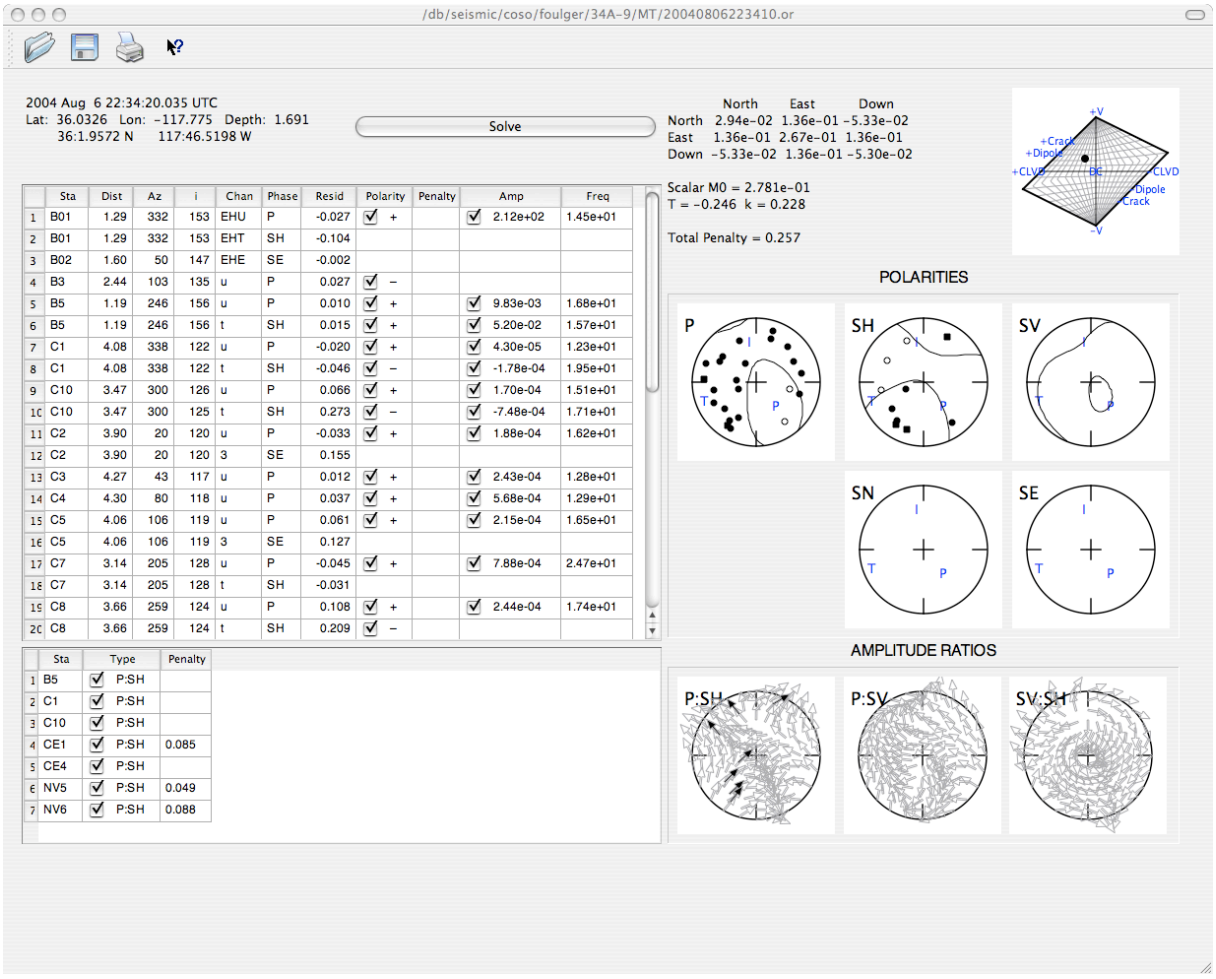

	Sta	Dist	Az	i	Chan	Phase	Resid	Polarity	Penalty	Amp	Freq
1	B01	1.29	332	153	EHU	P	-0.027	☑ +		☑ 2.12e+02	1.45e+01
2	B01	1.29	332	153	EHT	SH	-0.104				
3	B02	1.60	50	147	EHE	SE	-0.002				
4	B3	2.44	103	135	u	P	0.027	☑ −			
5	B5	1.19	246	156	u	P	0.010	☑ +		☑ 9.83e-03	1.68e+01
6	B5	1.19	246	156	t	SH	0.015	☑ +		☑ 5.20e-02	1.57e+01
7	C1	4.08	338	122	u	P	-0.020	☑ +		☑ 4.30e-05	1.23e+01
8	C1	4.08	338	122	t	SH	-0.046	☑ −		☑ -1.78e-04	1.95e+01
9	C10	3.47	300	126	u	P	0.066	☑ +		☑ 1.70e-04	1.51e+01
10	C10	3.47	300	125	t	SH	0.273	☑ −		☑ -7.48e-04	1.71e+01
11	C2	3.90	20	120	u	P	-0.033	☑ +		☑ 1.88e-04	1.62e+01
12	C2	3.90	20	120	3	SE	0.155				
13	C3	4.27	43	117	u	P	0.012	☑ +		☑ 2.43e-04	1.28e+01
14	C4	4.30	80	118	u	P	0.037	☑ +		☑ 5.68e-04	1.29e+01
15	C5	4.06	106	119	u	P	0.061	☑ +		☑ 2.15e-04	1.65e+01
16	C5	4.06	106	119	3	SE	0.127				
17	C7	3.14	205	128	u	P	-0.045	☑ +		☑ 7.88e-04	2.47e+01
18	C7	3.14	205	128	t	SH	-0.031				
19	C8	3.66	259	124	u	P	0.108	☑ +		☑ 2.44e-04	1.74e+01
20	C8	3.66	259	124	t	SH	0.209	☑ −			

	Sta	Type	Penalty
1	B5	☑ P:SH	
2	C1	☑ P:SH	
3	C10	☑ P:SH	
4	CE1	☑ P:SH	0.085
5	CE4	☑ P:SH	
6	NV5	☑ P:SH	0.049
7	NV6	☑ P:SH	0.088

Figure A5b. Same as Figure A5a but for the first co-injection earthquake (M = 1.2).

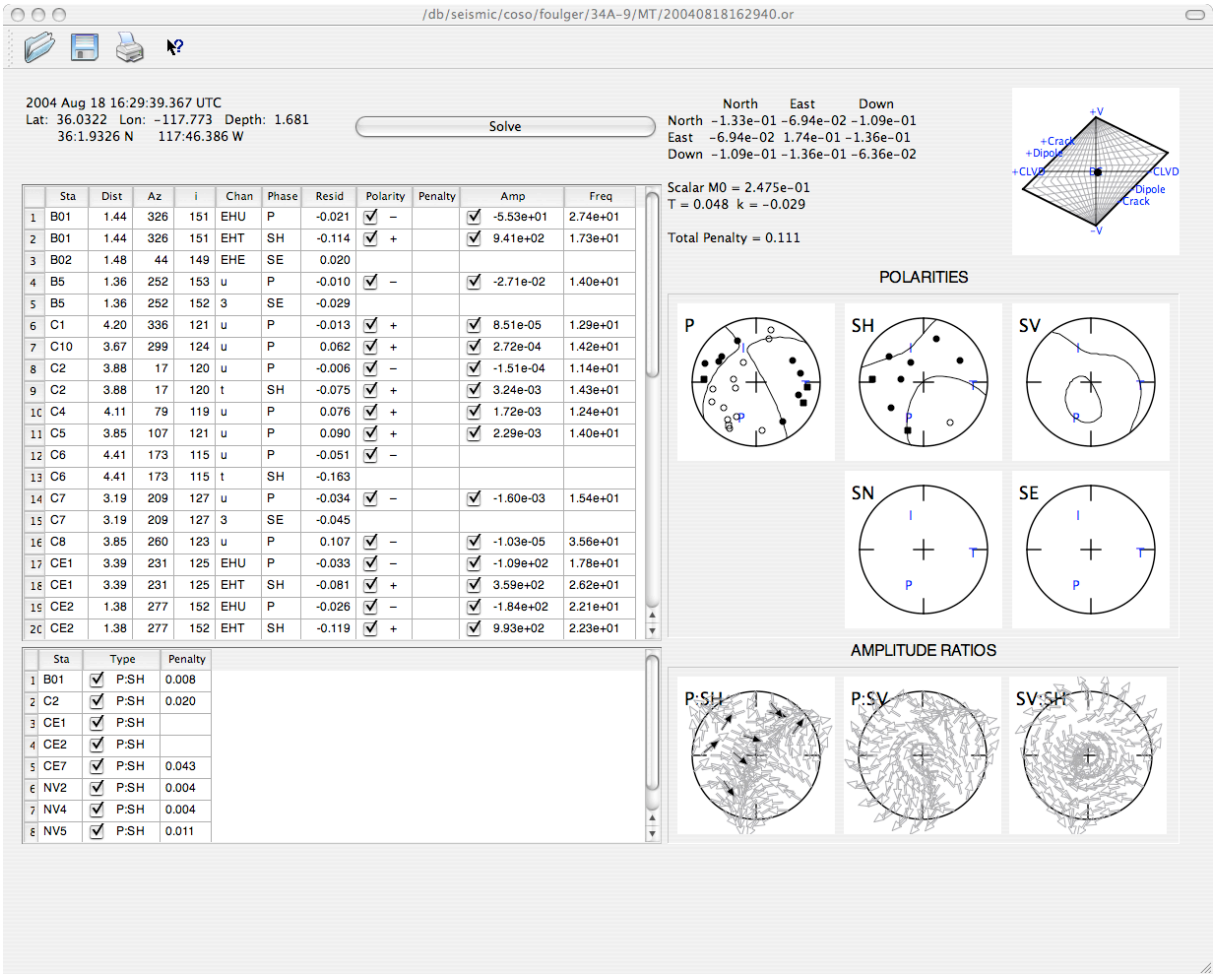

	Sta	Dist	Az	i	Chan	Phase	Resid	Polarity	Penalty	Amp	Freq
1	B01	1.44	326	151	EHU	P	-0.021	–		-5.53e+01	2.74e+01
2	B01	1.44	326	151	EHT	SH	-0.114	+		9.41e+02	1.73e+01
3	B02	1.48	44	149	EHE	SE	0.020				
4	B5	1.36	252	153	u	P	-0.010	–		-2.71e-02	1.40e+01
5	B5	1.36	252	152	3	SE	-0.029				
6	C1	4.20	336	121	u	P	-0.013	+		8.51e-05	1.29e+01
7	C10	3.67	299	124	u	P	0.062	+		2.72e-04	1.42e+01
8	C2	3.88	17	120	u	P	-0.006	–		-1.51e-04	1.14e+01
9	C2	3.88	17	120	t	SH	-0.075	+		3.24e-03	1.43e+01
10	C4	4.11	79	119	u	P	0.076	+		1.72e-03	1.24e+01
11	C5	3.85	107	121	u	P	0.090	+		2.29e-03	1.40e+01
12	C6	4.41	173	115	u	P	-0.051	–			
13	C6	4.41	173	115	t	SH	-0.163				
14	C7	3.19	209	127	u	P	-0.034	–		-1.60e-03	1.54e+01
15	C7	3.19	209	127	3	SE	-0.045				
16	C8	3.85	260	123	u	P	0.107	–		-1.03e-05	3.56e+01
17	CE1	3.39	231	125	EHU	P	-0.033	–		-1.09e+02	1.78e+01
18	CE1	3.39	231	125	EHT	SH	-0.081	+		3.59e+02	2.62e+01
19	CE2	1.38	277	152	EHU	P	-0.026	–		-1.84e+02	2.21e+01
20	CE2	1.38	277	152	EHT	SH	-0.119	+		9.93e+02	2.23e+01

	Sta	Type	Penalty
1	B01	P:SH	0.008
2	C2	P:SH	0.020
3	CE1	P:SH	
4	CE2	P:SH	
5	CE7	P:SH	0.043
6	NV2	P:SH	0.004
7	NV4	P:SH	0.004
8	NV5	P:SH	0.011

Figure A5c. Same as Figure A5a but for one of the largest (M = 1.7) post-injection earthquake.

6.6 Appendix 6: Table of earthquake parameters, June-October 2004.

The origin times, latitudes, longitudes and depths given were calculated using **eloc**, the location program attached to the moment tensor GUI user interface **eqmec**. The magnitudes quoted are from the U.S. Navy catalog. *k* is a measure of the volumetric component and ranges from +1 (pure explosion) to –1 (pure implosion). Such extreme values have never been observed in natural earthquakes. Red cells indicate earthquakes associated with the 6th – 13th August injection.

#		Date/hr/min	Second	Lat	Long	Depth	Navy mag	k
1	June	200406040903	29.03	36N0195	117W4595	3.01	0.9	-0.172
2		200406071200	52.62	36N0185	117W4620	2.91	1.1	0.174
3		200406071233	61.29	36N0187	117W4622	2.81	1.6	0.227
4		200406180051	58.99	36N0204	117W4607	2.58	0.7	-0.298
5		200406240233	12.09	36N0179	117W4617	2.47	0.5	0.479
6		200406302107	35.81	36N0199	117W4638	2.65	0.6	0.257
7	July	200407160336	42.64	36N0184	117W4617	2.42	2.0	0.000
8		200407172343	47.74	36N0171	117W4651	2.81	1.9	0.322
9		200407172343	23.40	36N0169	117W4641	2.68	1.6	-0.042
10		200407240855	34.90	36N0190	117W4660	2.69	1.1	0.148
11		200407280312	19.20	36N0186	117W4622	2.18	0.9	0.287
12		200407302013	5.35	36N0172	117W4637	2.69	1.0	0.293
13		200407302016	60.15	36N0168	117W4642	2.50	0.8	-0.030
14	August	200408020100	44.66	36N0162	117W4594	2.74	1.0	0.152
15		200408020104	66.84	36N0172	117W4601	2.49	0.7	0.215
16		200408020622	46.07	36N0193	117W4646	2.29	0.7	0.284
17		200408040434	4.62	36N0183	117W4617	2.31	0.5	0.228
18		200408062234	19.98	36N0196	117W4621	3.01	1.2	0.094
19		200408062326	29.05	36N0195	117W4606	2.86	0.5	0.015
20		200408062351	14.15	36N0192	117W4611	2.56	1.1	0.201
21		200408062351	39.74	36N0190	117W4608	2.60	0.8	0.173
22		200408062351	21.67	36N0193	117W4598	2.49	0.6	0.015
23		200408062352	23.00	36N0200	117W4614	2.56	0.5	0.314
24		200408070519	27.45	36N0205	117W4616	2.63	1.2	-0.177
25		200408070953	49.16	36N0207	117W4615	2.74	0.6	0.202
26		200408071333	33.72	36N0207	117W4619	2.39	0.7	0.164
27		200408071546	67.05	36N0194	117W4629	2.40	0.5	0.179
28		200408072112	51.07	36N0207	117W4614	2.87	1.2	0.193
29		200408072136	58.98	36N0209	117W4610	2.41	0.6	0.267
30		200408072320	52.39	36N0208	117W4624	2.75	0.6	0.032
31		200408080552	32.15	36N0210	117W4606	2.67	1.1	0.145
32		200408080752	33.26	36N0205	117W4617	2.45	0.8	0.025
33		200408081629	25.21	36N0196	117W4622	2.47	1.1	0.310
34		200408090045	39.79	36N0180	117W4626	2.12	0.6	0.104

35		200408091128	34.77	36N0206	117W4621	2.70	0.7	0.310
36		200408091311	71.80	36N0199	117W4621	2.61	0.9	0.453
37		200408091314	56.71	36N0195	117W4627	2.67	1.2	0.263
38		200408091721	14.78	36N0207	117W4608	2.91	1.3	0.096
39		200408101327	40.76	36N0202	117W4609	2.88	0.5	0.311
40		200408101330	65.35	36N0207	117W4617	2.75	0.6	-0.012
41		200408111550	62.90	36N0205	117W4614	2.46	1.0	0.078
42		200408111552	47.04	36N0203	117W4617	2.40	0.7	0.162
43		200408130246	35.12	36N0205	117W4617	2.40	1.3	0.158
44		200408181623	62.94	36N0203	117W4618	2.70	1.6	0.099
45		200408181629	39.34	36N0198	117W4619	2.73	1.7	-0.029
46		200408181629	11.11	36N0185	117W4644	2.50	0.6	0.315
47		200408181630	4.11	36N0190	117W4638	2.57	1.1	0.229
48		200408181630	20.35	36N0188	117W4629	2.76	1.0	0.104
49		200408181631	12.58	36N0190	117W4645	2.72	2.2	0.287
50		200408181634	71.61	36N0204	117W4613	2.69	0.9	0.111
51		200408181641	21.84	36N0189	117W4641	2.44	0.7	0.228
52		200408181646	35.15	36N0188	117W4643	2.41	0.5	0.325
53		200408311217	57.14	36N0201	117W4642	2.72	1.0	0.387
54	September	200409011422	30.37	36N0196	117W4636	2.60	1.1	0.205
55		200409070751	8.98	36N0209	117W4623	2.49	0.8	0.200
56		200409151837	71.63	36N0198	117W4625	2.34	0.8	-0.103
57		200409162121	61.89	36N0176	117W4654	2.46	1.0	-0.073
58		200409192320	45.60	36N0192	117W4639	2.54	1.5	0.385
59		200409200155	14.38	36N0188	117W4629	2.76	0.8	0.319
60		200409211353	39.69	36N0179	117W4611	2.73	1.3	0.077
61		200409211353	49.52	36N0173	117W4615	2.51	0.6	0.285
62	October	200410101957	51.11	36N0188	117W4646	2.05	0.5	0.288
63		200410160157	53.96	36N0198	117W4629	2.15	0.6	0.340
64		200410250503	42.70	36N0175	117W4638	2.52	1.1	0.259
65		200410250505	40.09	36N0173	117W4639	2.34	0.5	0.316
66		200410280132	41.43	36N0178	117W4625	2.24	0.7	-0.018
67		200410280353	44.70	36N0178	117W4627	2.00	0.6	0.031
68		200410280415	8.96	36N0176	117W4624	2.11	1.1	0.121
69		200410280416	57.53	36N0182	117W4616	2.09	1.1	0.143
70		200410280700	20.13	36N0178	117W4622	2.34	1.3	0.157
71		200410280718	22.08	36N0180	117W4623	2.19	1.1	0.268
72		200410281228	52.34	36N0199	117W4630	1.92	0.5	0.136
73		200410301232	26.37	36N0185	117W4620	2.85	0.6	0.169
74		200410311226	31.82	36N0181	117W4629	2.22	1.0	-0.124
75		200410312302	16.12	36N0179	117W4622	2.53	2.8	0.090

6.7 *Appendix 7. Details of moment tensor results: well 46A-19RD*

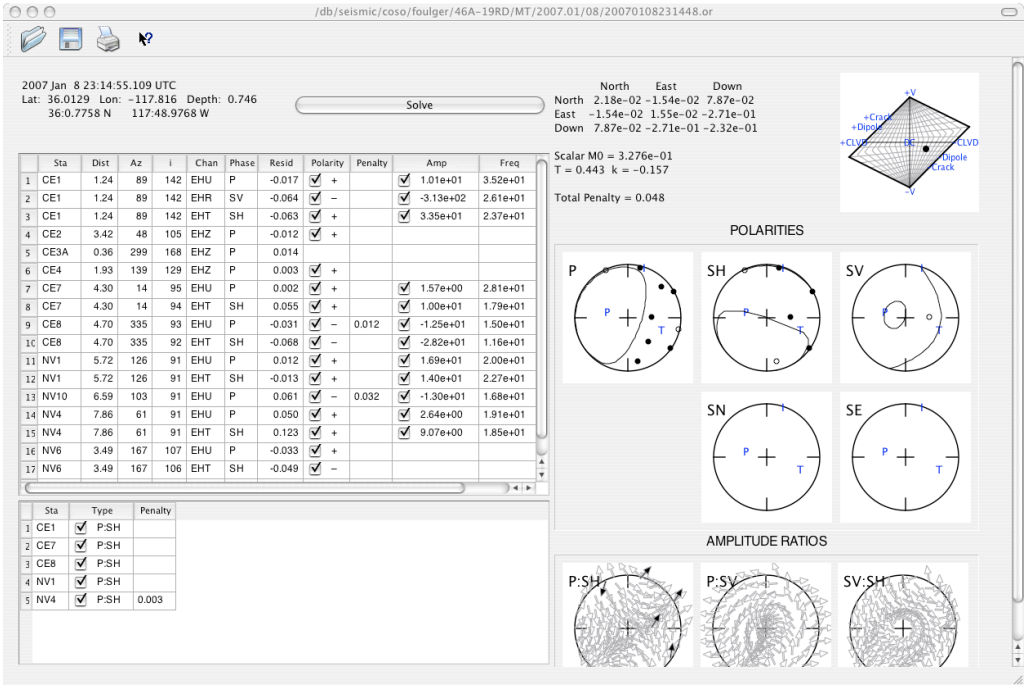

	Sta	Dist	Az	i	Chan	Phase	Resid	Polarity	Penalty	Amp	Freq
1	CE1	1.24	89	142	EHU	P	-0.017	+		1.01e+01	3.52e+01
2	CE1	1.24	89	142	EHR	SV	-0.064	–		-3.13e+02	2.61e+01
3	CE1	1.24	89	142	EHT	SH	-0.063	+		3.35e+01	2.37e+01
4	CE2	3.42	48	105	EHZ	P	-0.012	+			
5	CE3A	0.36	299	168	EHZ	P	0.014				
6	CE4	1.93	139	129	EHZ	P	0.003	+			
7	CE7	4.30	14	95	EHU	P	0.002	+		1.57e+00	2.81e+01
8	CE7	4.30	14	94	EHT	SH	0.055	+		1.00e+01	1.79e+01
9	CE8	4.70	335	93	EHU	P	-0.031	–	0.012	-1.25e+01	1.50e+01
10	CE8	4.70	335	92	EHT	SH	-0.068	–		-2.82e+01	1.16e+01
11	NV1	5.72	126	91	EHU	P	0.012	+		1.69e+01	2.00e+01
12	NV1	5.72	126	91	EHT	SH	-0.013	+		1.40e+01	2.27e+01
13	NV10	6.59	103	91	EHU	P	0.061	–	0.032	-1.30e+01	1.68e+01
14	NV4	7.86	61	91	EHU	P	0.050	+		2.64e+00	1.91e+01
15	NV4	7.86	61	91	EHT	SH	0.123	+		9.07e+00	1.85e+01
16	NV6	3.49	167	107	EHU	P	-0.033	+			
17	NV6	3.49	167	106	EHT	SH	-0.049	–			

	Sta	Type	Penalty
1	CE1	P:SH	
2	CE7	P:SH	
3	CE8	P:SH	
4	NV1	P:SH	
5	NV4	P:SH	0.003

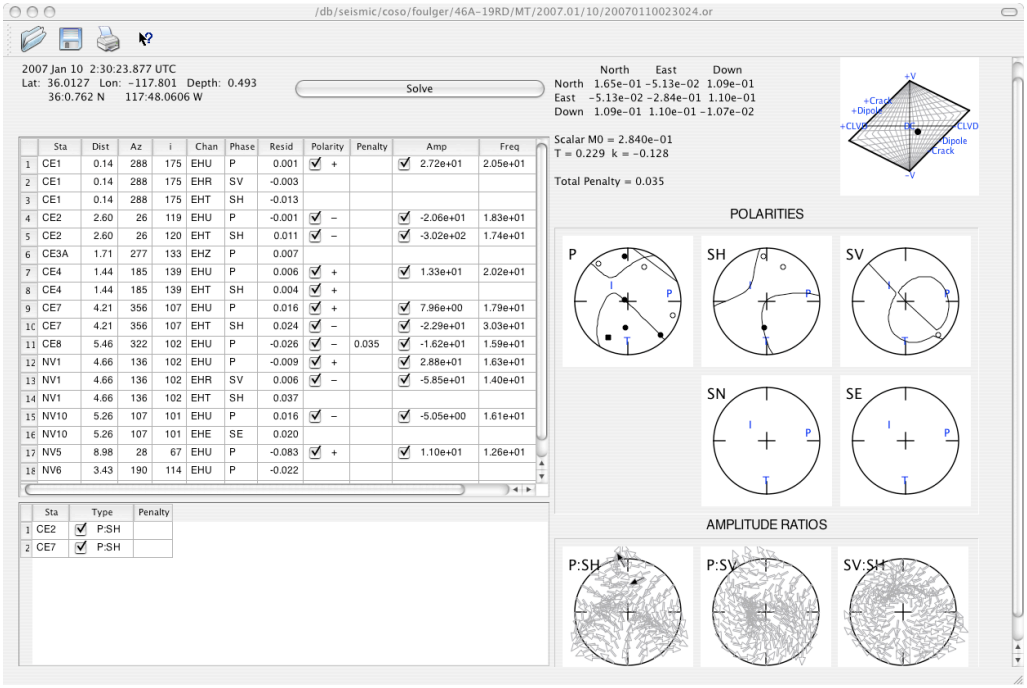

	Sta	Dist	Az	i	Chan	Phase	Resid	Polarity	Penalty	Amp	Freq
1	CE1	0.14	288	175	EHU	P	0.001	+		2.72e+01	2.05e+01
2	CE1	0.14	288	175	EHR	SV	-0.003				
3	CE1	0.14	288	175	EHT	SH	-0.013				
4	CE2	2.60	26	119	EHU	P	-0.001	–		-2.06e+01	1.83e+01
5	CE2	2.60	26	120	EHT	SH	0.011	–		-3.02e+02	1.74e+01
6	CE3A	1.71	277	133	EHZ	P	0.007				
7	CE4	1.44	185	139	EHU	P	0.006	+		1.33e+01	2.02e+01
8	CE4	1.44	185	139	EHT	SH	0.004	+			
9	CE7	4.21	356	107	EHU	P	0.016	+		7.96e+00	1.79e+01
10	CE7	4.21	356	107	EHT	SH	0.024	–		-2.29e+01	3.03e+01
11	CE8	5.46	322	102	EHU	P	-0.026	–	0.035	-1.62e+01	1.59e+01
12	NV1	4.66	136	102	EHU	P	-0.009	+		2.88e+01	1.63e+01
13	NV1	4.66	136	102	EHR	SV	0.006	–		-5.85e+01	1.40e+01
14	NV1	4.66	136	102	EHT	SH	0.037				
15	NV10	5.26	107	101	EHU	P	0.016	–		-5.05e+00	1.61e+01
16	NV10	5.26	107	101	EHE	SE	0.020				
17	NV5	8.98	28	67	EHU	P	-0.083	+		1.10e+01	1.26e+01
18	NV6	3.43	190	114	EHU	P	-0.022				

	Sta	Type	Penalty
1	CE2	P:SH	
2	CE7	P:SH	

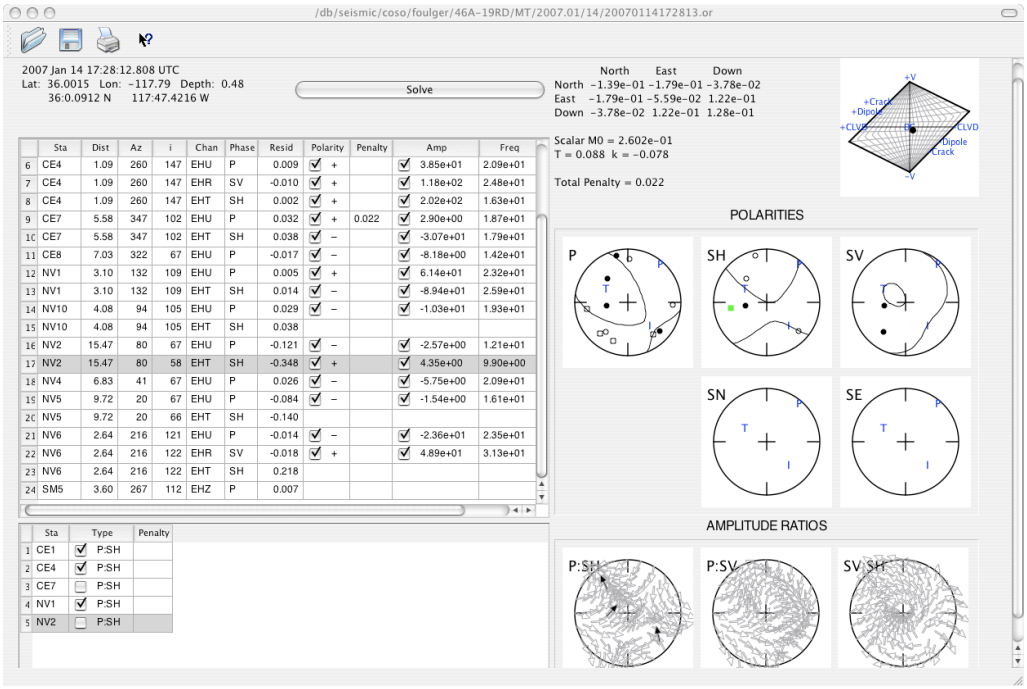

	Sta	Dist	Az	i	Chan	Phase	Resid	Polarity	Penalty	Amp	Freq
6	CE4	1.09	260	147	EHU	P	0.009	+		3.85e+01	2.09e+01
7	CE4	1.09	260	147	EHR	SV	-0.010	+		1.18e+02	2.48e+01
8	CE4	1.09	260	147	EHT	SH	0.002	+		2.02e+02	1.63e+01
9	CE7	5.58	347	102	EHU	P	0.032	+	0.022	2.90e+00	1.87e+01
10	CE7	5.58	347	102	EHT	SH	0.038	–		-3.07e+01	1.79e+01
11	CE8	7.03	322	67	EHU	P	-0.017	–		-8.18e+00	1.42e+01
12	NV1	3.10	132	109	EHU	P	0.005	+		6.14e+01	2.32e+01
13	NV1	3.10	132	109	EHT	SH	0.014	–		-8.94e+01	2.59e+01
14	NV10	4.08	94	105	EHU	P	0.029	–		-1.03e+01	1.93e+01
15	NV10	4.08	94	105	EHT	SH	0.038				
16	NV2	15.47	80	67	EHU	P	-0.121	–		-2.57e+00	1.21e+01
17	NV2	15.47	80	58	EHT	SH	-0.348	+		4.35e+00	9.90e+00
18	NV4	6.83	41	67	EHU	P	0.026	–		-5.75e+00	2.09e+01
19	NV5	9.72	20	67	EHU	P	-0.084	–		-1.54e+00	1.61e+01
20	NV5	9.72	20	66	EHT	SH	-0.140				
21	NV6	2.64	216	121	EHU	P	-0.014	–		-2.36e+01	2.35e+01
22	NV6	2.64	216	122	EHR	SV	-0.018	+		4.89e+01	3.13e+01
23	NV6	2.64	216	122	EHT	SH	0.218				
24	SM5	3.60	267	112	EHZ	P	0.007				

	Sta	Type	Penalty
1	CE1	P:SH	
2	CE4	P:SH	
3	CE7	P:SH	
4	NV1	P:SH	
5	NV2	P:SH	

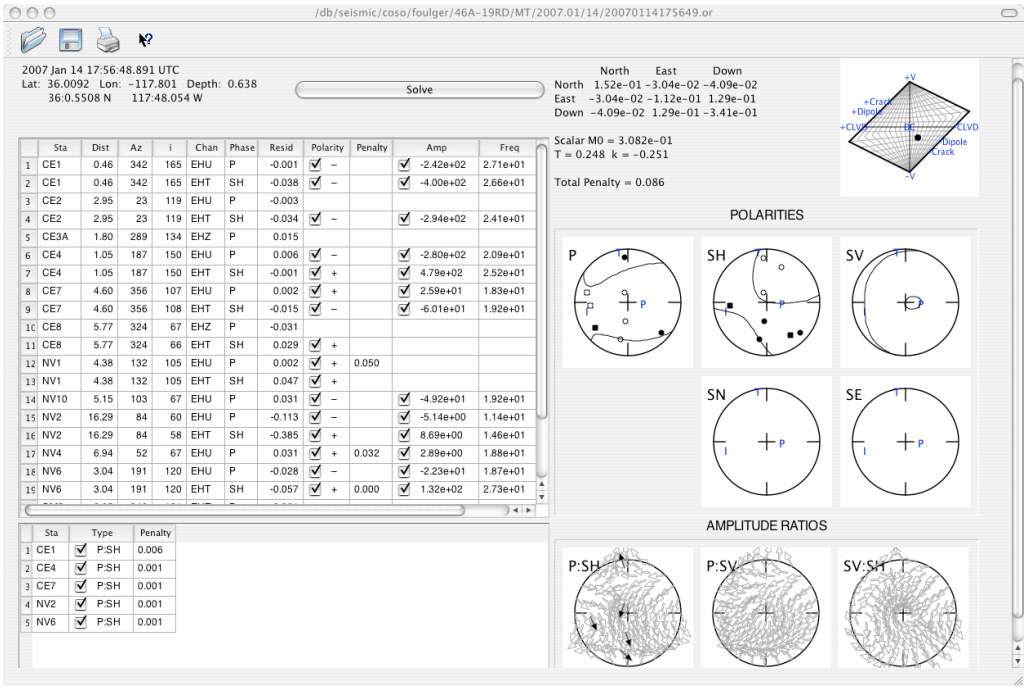

	Sta	Dist	Az	i	Chan	Phase	Resid	Polarity	Penalty	Amp	Freq
1	CE1	0.46	342	165	EHU	P	-0.001	–		-2.42e+02	2.71e+01
2	CE1	0.46	342	165	EHT	SH	-0.038	–		-4.00e+02	2.66e+01
3	CE2	2.95	23	119	EHU	P	-0.003				
4	CE2	2.95	23	119	EHT	SH	-0.034	–		-2.94e+02	2.41e+01
5	CE3A	1.80	289	134	EHZ	P	0.015				
6	CE4	1.05	187	150	EHU	P	0.006	–		-2.80e+02	2.09e+01
7	CE4	1.05	187	150	EHT	SH	-0.001	+		4.79e+02	2.52e+01
8	CE7	4.60	356	107	EHU	P	0.002	+		2.59e+01	1.83e+01
9	CE7	4.60	356	108	EHT	SH	-0.015	–		-6.01e+01	1.92e+01
10	CE8	5.77	324	67	EHZ	P	-0.031				
11	CE8	5.77	324	66	EHT	SH	0.029	+			
12	NV1	4.38	132	105	EHU	P	0.002	+	0.050		
13	NV1	4.38	132	105	EHT	SH	0.047	+			
14	NV10	5.15	103	67	EHU	P	0.031	–		-4.92e+01	1.92e+01
15	NV2	16.29	84	60	EHU	P	-0.113	–		-5.14e+00	1.14e+01
16	NV2	16.29	84	58	EHT	SH	-0.385	+		8.69e+00	1.46e+01
17	NV4	6.94	52	67	EHU	P	0.031	+	0.032	2.89e+00	1.88e+01
18	NV6	3.04	191	120	EHU	P	-0.028	–		-2.23e+01	1.87e+01
19	NV6	3.04	191	120	EHT	SH	-0.057	+	0.000	1.32e+02	2.73e+01

	Sta	Type	Penalty
1	CE1	P:SH	0.006
2	CE4	P:SH	0.001
3	CE7	P:SH	0.001
4	NV2	P:SH	0.001
5	NV6	P:SH	0.001

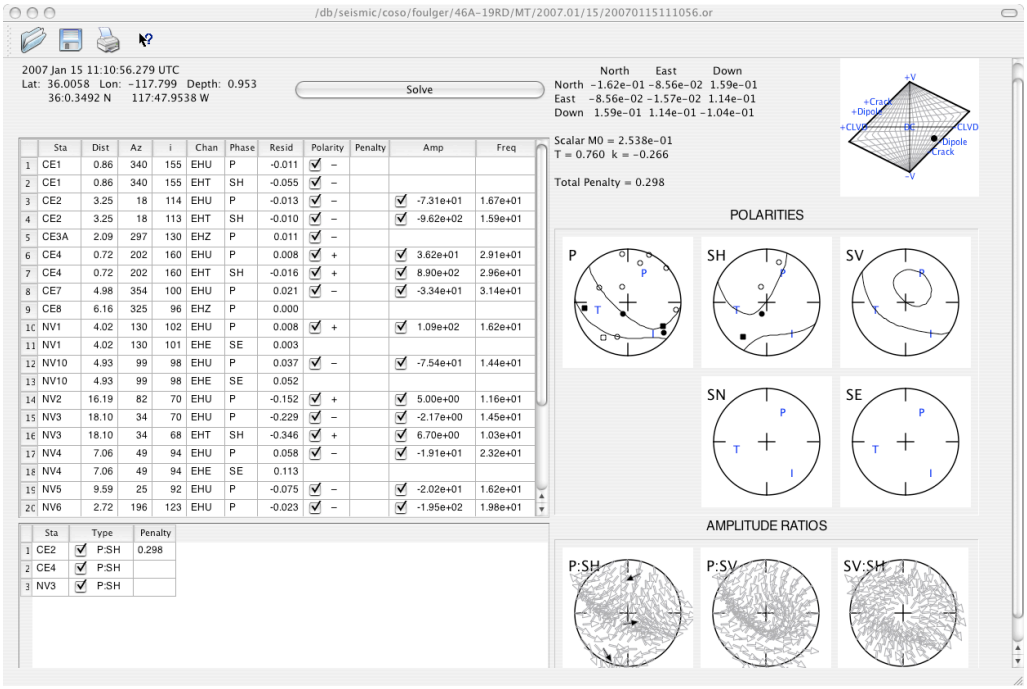

	Sta	Dist	Az	i	Chan	Phase	Resid	Polarity	Penalty	Amp	Freq
1	CE1	0.86	340	155	EHU	P	-0.011	☑ –			
2	CE1	0.86	340	155	EHT	SH	-0.055	☑ –			
3	CE2	3.25	18	114	EHU	P	-0.013	☑ –		☑ -7.31e+01	1.67e+01
4	CE2	3.25	18	113	EHT	SH	-0.010	☑ –		☑ -9.62e+02	1.59e+01
5	CE3A	2.09	297	130	EHZ	P	0.011	☑ –			
6	CE4	0.72	202	160	EHU	P	0.008	☑ +		☑ 3.62e+01	2.91e+01
7	CE4	0.72	202	160	EHT	SH	-0.016	☑ +		☑ 8.90e+02	2.96e+01
8	CE7	4.98	354	100	EHU	P	0.021	☑ –		☑ -3.34e+01	3.14e+01
9	CE8	6.16	325	96	EHZ	P	0.000				
10	NV1	4.02	130	102	EHU	P	0.008	☑ +		☑ 1.09e+02	1.62e+01
11	NV1	4.02	130	101	EHE	SE	0.003				
12	NV10	4.93	99	98	EHU	P	0.037	☑ –		☑ -7.54e+01	1.44e+01
13	NV10	4.93	99	98	EHE	SE	0.052				
14	NV2	16.19	82	70	EHU	P	-0.152	☑ +		☑ 5.00e+00	1.16e+01
15	NV3	18.10	34	70	EHU	P	-0.229	☑ –		☑ -2.17e+00	1.45e+01
16	NV3	18.10	34	68	EHT	SH	-0.346	☑ +		☑ 6.70e+00	1.03e+01
17	NV4	7.06	49	94	EHU	P	0.058	☑ –		☑ -1.91e+01	2.32e+01
18	NV4	7.06	49	94	EHE	SE	0.113				
19	NV5	9.59	25	92	EHU	P	-0.075	☑ –		☑ -2.02e+01	1.62e+01
20	NV6	2.72	196	123	EHU	P	-0.023	☑ –		☑ -1.95e+02	1.98e+01

	Sta	Type	Penalty
1	CE2	☑ P:SH	0.298
2	CE4	☑ P:SH	
3	NV3	☑ P:SH	

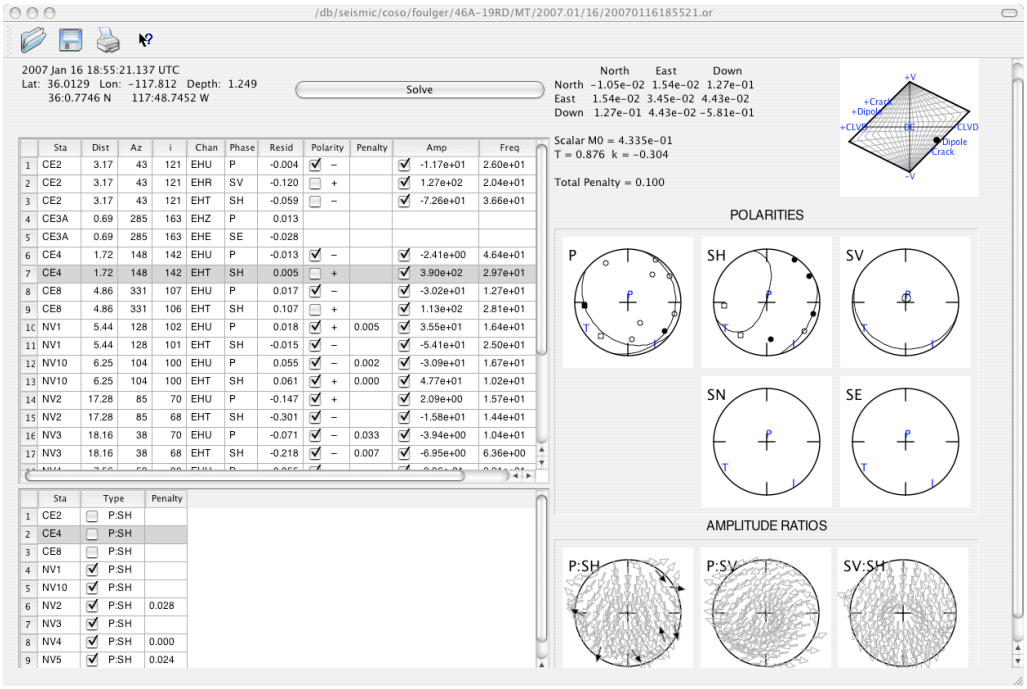

	Sta	Dist	Az	i	Chan	Phase	Resid	Polarity	Penalty	Amp	Freq
1	CE2	3.17	43	121	EHU	P	-0.004	☑ –		☑ -1.17e+01	2.60e+01
2	CE2	3.17	43	121	EHR	SV	-0.120	☐ +		☑ 1.27e+02	2.04e+01
3	CE2	3.17	43	121	EHT	SH	-0.059	☐ –		☑ -7.26e+01	3.66e+01
4	CE3A	0.69	285	163	EHZ	P	0.013				
5	CE3A	0.69	285	163	EHE	SE	-0.028				
6	CE4	1.72	148	142	EHU	P	-0.013	☑ –		☑ -2.41e+00	4.64e+01
7	CE4	1.72	148	142	EHT	SH	0.005	☐ +		☑ 3.90e+02	2.97e+01
8	CE8	4.86	331	107	EHU	P	0.017	☑ –		☑ -3.02e+01	1.27e+01
9	CE8	4.86	331	106	EHT	SH	0.107	☐ +		☑ 1.13e+02	2.81e+01
10	NV1	5.44	128	102	EHU	P	0.018	☑ +	0.005	☑ 3.55e+01	1.64e+01
11	NV1	5.44	128	101	EHT	SH	-0.015	☑ –		☑ -5.41e+01	2.50e+01
12	NV10	6.25	104	100	EHU	P	0.055	☑ –	0.002	☑ -3.09e+01	1.67e+01
13	NV10	6.25	104	100	EHT	SH	0.061	☑ +	0.000	☑ 4.77e+01	1.02e+01
14	NV2	17.28	85	70	EHU	P	-0.147	☑ +		☑ 2.09e+00	1.57e+01
15	NV2	17.28	85	68	EHT	SH	-0.301	☑ –		☑ -1.58e+01	1.44e+01
16	NV3	18.16	38	70	EHU	P	-0.071	☑ –	0.033	☑ -3.94e+00	1.04e+01
17	NV3	18.16	38	68	EHT	SH	-0.218	☑ –	0.007	☑ -6.95e+00	6.36e+00

	Sta	Type	Penalty
1	CE2	☐ P:SH	
2	CE4	☐ P:SH	
3	CE8	☐ P:SH	
4	NV1	☑ P:SH	
5	NV10	☑ P:SH	
6	NV2	☑ P:SH	0.028
7	NV3	☑ P:SH	
8	NV4	☑ P:SH	0.000
9	NV5	☑ P:SH	0.024

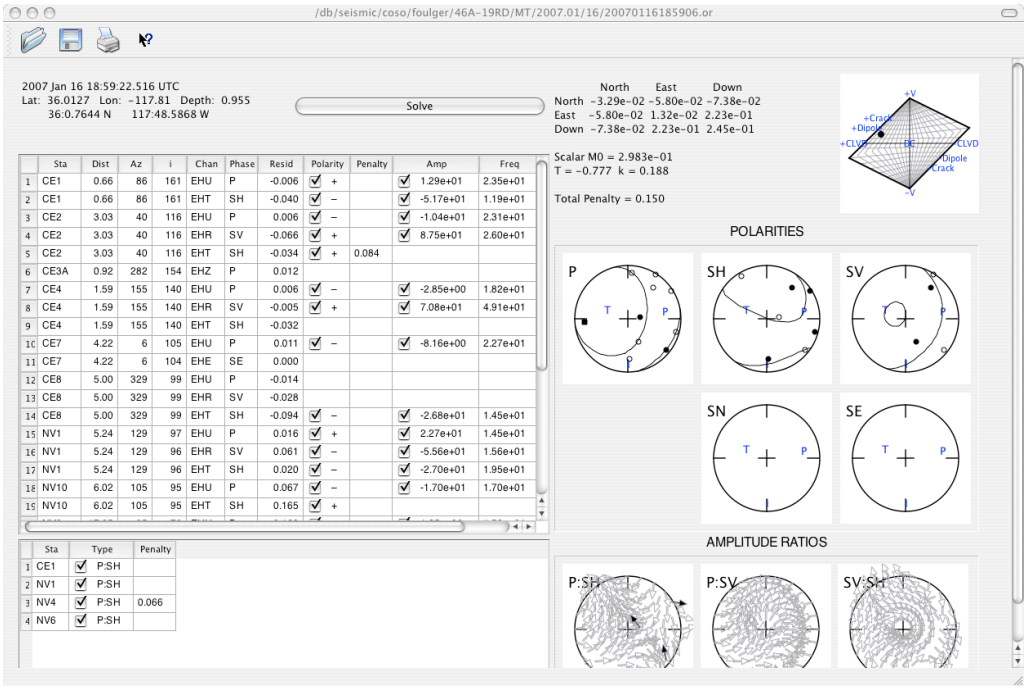

	Sta	Dist	Az	i	Chan	Phase	Resid	Polarity	Penalty	Amp	Freq
1	CE1	0.66	86	161	EHU	P	-0.006	+		1.29e+01	2.35e+01
2	CE1	0.66	86	161	EHT	SH	-0.040	–		-5.17e+01	1.19e+01
3	CE2	3.03	40	116	EHU	P	0.006	–		-1.04e+01	2.31e+01
4	CE2	3.03	40	116	EHR	SV	-0.066	+		8.75e+01	2.60e+01
5	CE2	3.03	40	116	EHT	SH	-0.034	+	0.084		
6	CE3A	0.92	282	154	EHZ	P	0.012				
7	CE4	1.59	155	140	EHU	P	0.006	–		-2.85e+00	1.82e+01
8	CE4	1.59	155	140	EHR	SV	-0.005	+		7.08e+01	4.91e+01
9	CE4	1.59	155	140	EHT	SH	-0.032				
10	CE7	4.22	6	105	EHU	P	0.011	–		-8.16e+00	2.27e+01
11	CE7	4.22	6	104	EHE	SE	0.000				
12	CE8	5.00	329	99	EHU	P	-0.014				
13	CE8	5.00	329	99	EHR	SV	-0.028				
14	CE8	5.00	329	99	EHT	SH	-0.094	–		-2.68e+01	1.45e+01
15	NV1	5.24	129	97	EHU	P	0.016	+		2.27e+01	1.45e+01
16	NV1	5.24	129	96	EHR	SV	0.061	–		-5.56e+01	1.56e+01
17	NV1	5.24	129	96	EHT	SH	0.020	–		-2.70e+01	1.95e+01
18	NV10	6.02	105	95	EHU	P	0.067	–		-1.70e+01	1.70e+01
19	NV10	6.02	105	95	EHT	SH	0.165	+			

	Sta	Type	Penalty
1	CE1	P:SH	
2	NV1	P:SH	
3	NV4	P:SH	0.066
4	NV6	P:SH	

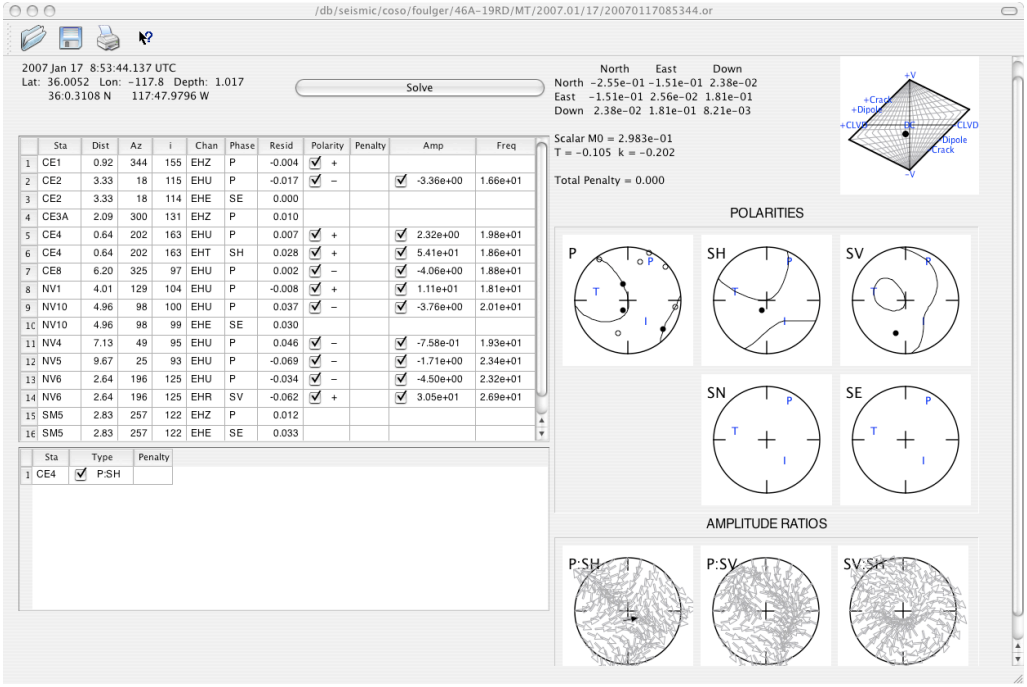

	Sta	Dist	Az	i	Chan	Phase	Resid	Polarity	Penalty	Amp	Freq
1	CE1	0.92	344	155	EHZ	P	-0.004	+			
2	CE2	3.33	18	115	EHU	P	-0.017	–		-3.36e+00	1.66e+01
3	CE2	3.33	18	114	EHE	SE	0.000				
4	CE3A	2.09	300	131	EHZ	P	0.010				
5	CE4	0.64	202	163	EHU	P	0.007	+		2.32e+00	1.98e+01
6	CE4	0.64	202	163	EHT	SH	0.028	+		5.41e+01	1.86e+01
7	CE8	6.20	325	97	EHU	P	0.002	–		-4.06e+00	1.88e+01
8	NV1	4.01	129	104	EHU	P	-0.008	+		1.11e+01	1.81e+01
9	NV10	4.96	98	100	EHU	P	0.037	–		-3.76e+00	2.01e+01
10	NV10	4.96	98	99	EHE	SE	0.030				
11	NV4	7.13	49	95	EHU	P	0.046	–		-7.58e-01	1.93e+01
12	NV5	9.67	25	93	EHU	P	-0.069	–		-1.71e+00	2.34e+01
13	NV6	2.64	196	125	EHU	P	-0.034	–		-4.50e+00	2.32e+01
14	NV6	2.64	196	125	EHR	SV	-0.062	+		3.05e+01	2.69e+01
15	SM5	2.83	257	122	EHZ	P	0.012				
16	SM5	2.83	257	122	EHE	SE	0.033				

	Sta	Type	Penalty
1	CE4	P:SH	

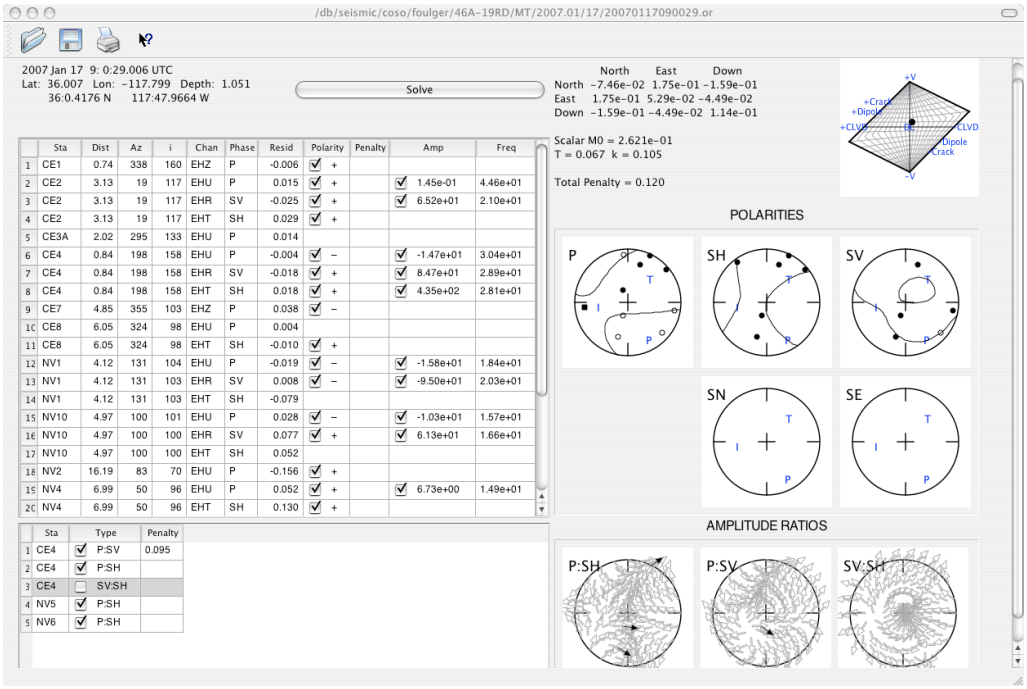

	Sta	Dist	Az	i	Chan	Phase	Resid	Polarity	Penalty	Amp	Freq
1	CE1	0.74	338	160	EHZ	P	-0.006	+			
2	CE2	3.13	19	117	EHU	P	0.015	+		1.45e-01	4.46e+01
3	CE2	3.13	19	117	EHR	SV	-0.025	+		6.52e+01	2.10e+01
4	CE2	3.13	19	117	EHT	SH	0.029	+			
5	CE3A	2.02	295	133	EHU	P	0.014				
6	CE4	0.84	198	158	EHU	P	-0.004	–		-1.47e+01	3.04e+01
7	CE4	0.84	198	158	EHR	SV	-0.018	+		8.47e+01	2.89e+01
8	CE4	0.84	198	158	EHT	SH	0.018	+		4.35e+02	2.81e+01
9	CE7	4.85	355	103	EHZ	P	0.038	–			
10	CE8	6.05	324	98	EHU	P	0.004				
11	CE8	6.05	324	98	EHT	SH	-0.010	+			
12	NV1	4.12	131	104	EHU	P	-0.019	–		-1.58e+01	1.84e+01
13	NV1	4.12	131	103	EHR	SV	0.008	–		-9.50e+01	2.03e+01
14	NV1	4.12	131	103	EHT	SH	-0.079				
15	NV10	4.97	100	101	EHU	P	0.028	–		-1.03e+01	1.57e+01
16	NV10	4.97	100	100	EHR	SV	0.077	+		6.13e+01	1.66e+01
17	NV10	4.97	100	100	EHT	SH	0.052				
18	NV2	16.19	83	70	EHU	P	-0.156	+			
19	NV4	6.99	50	96	EHU	P	0.052	+		6.73e+00	1.49e+01
20	NV4	6.99	50	96	EHT	SH	0.130	+			

	Sta	Type	Penalty
1	CE4	P:SV	0.095
2	CE4	P:SH	
3	CE4	SV:SH	
4	NV5	P:SH	
5	NV6	P:SH	

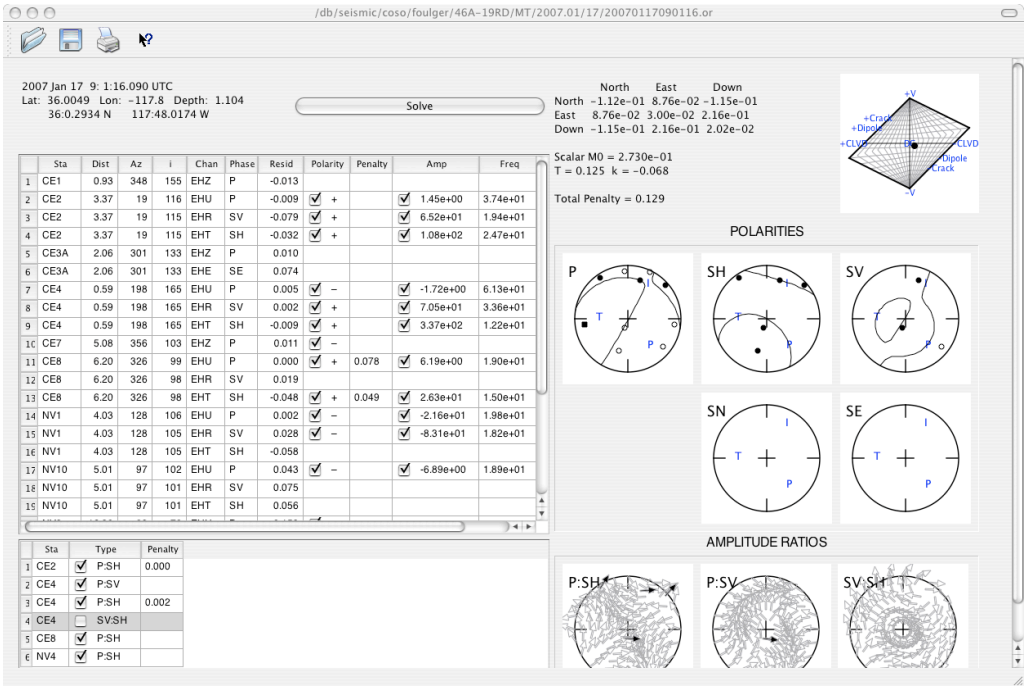

	Sta	Dist	Az	i	Chan	Phase	Resid	Polarity	Penalty	Amp	Freq
1	CE1	0.93	348	155	EHZ	P	-0.013				
2	CE2	3.37	19	116	EHU	P	-0.009	+		1.45e+00	3.74e+01
3	CE2	3.37	19	115	EHR	SV	-0.079	+		6.52e+01	1.94e+01
4	CE2	3.37	19	115	EHT	SH	-0.032	+		1.08e+02	2.47e+01
5	CE3A	2.06	301	133	EHZ	P	0.010				
6	CE3A	2.06	301	133	EHE	SE	0.074				
7	CE4	0.59	198	165	EHU	P	0.005	–		-1.72e+00	6.13e+01
8	CE4	0.59	198	165	EHR	SV	0.002	+		7.05e+01	3.36e+01
9	CE4	0.59	198	165	EHT	SH	-0.009	+		3.37e+02	1.22e+01
10	CE7	5.08	356	103	EHZ	P	0.011	–			
11	CE8	6.20	326	99	EHU	P	0.000	+	0.078	6.19e+00	1.90e+01
12	CE8	6.20	326	98	EHR	SV	0.019				
13	CE8	6.20	326	98	EHT	SH	-0.048	+	0.049	2.63e+01	1.50e+01
14	NV1	4.03	128	106	EHU	P	0.002	–		-2.16e+01	1.98e+01
15	NV1	4.03	128	105	EHR	SV	0.028	–		-8.31e+01	1.82e+01
16	NV1	4.03	128	105	EHT	SH	-0.058				
17	NV10	5.01	97	102	EHU	P	0.043	–		-6.89e+00	1.89e+01
18	NV10	5.01	97	101	EHR	SV	0.075				
19	NV10	5.01	97	101	EHT	SH	0.056				

	Sta	Type	Penalty
1	CE2	P:SH	0.000
2	CE4	P:SV	
3	CE4	P:SH	0.002
4	CE4	SV:SH	
5	CE8	P:SH	
6	NV4	P:SH	

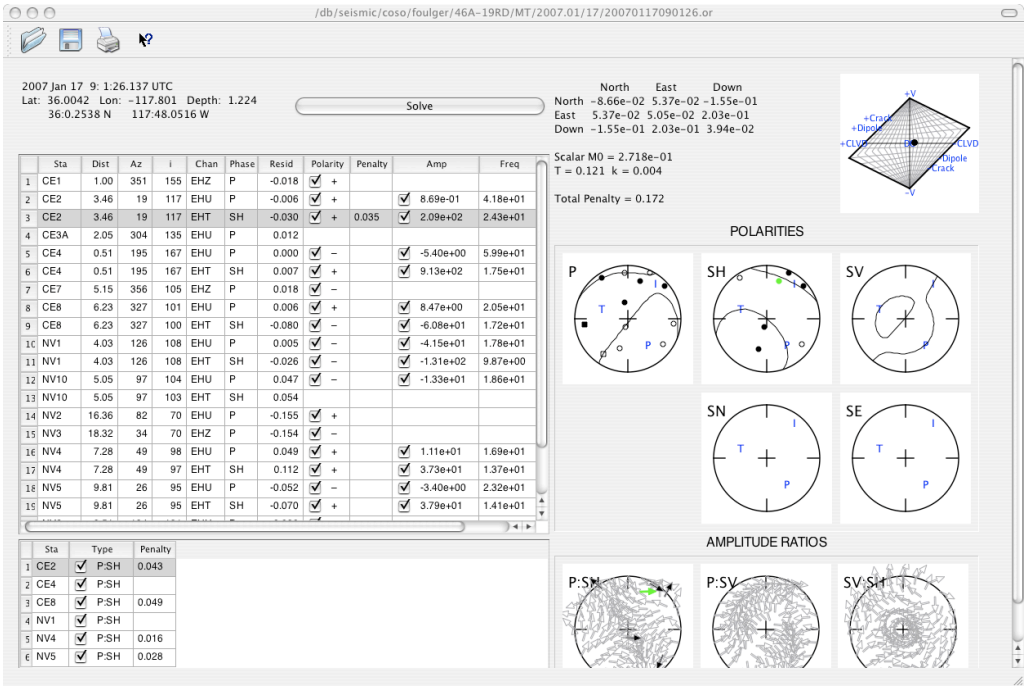

	Sta	Dist	Az	i	Chan	Phase	Resid	Polarity	Penalty	Amp	Freq
1	CE1	1.00	351	155	EHZ	P	-0.018	+			
2	CE2	3.46	19	117	EHU	P	-0.006	+		8.69e-01	4.18e+01
3	CE2	3.46	19	117	EHT	SH	-0.030	+	0.035	2.09e+02	2.43e+01
4	CE3A	2.05	304	135	EHU	P	0.012				
5	CE4	0.51	195	167	EHU	P	0.000	−		-5.40e+00	5.99e+01
6	CE4	0.51	195	167	EHT	SH	0.007	+		9.13e+02	1.75e+01
7	CE7	5.15	356	105	EHZ	P	0.018	−			
8	CE8	6.23	327	101	EHU	P	0.006	+		8.47e+00	2.05e+01
9	CE8	6.23	327	100	EHT	SH	-0.080	−		-6.08e+01	1.72e+01
10	NV1	4.03	126	108	EHU	P	0.005	−		-4.15e+01	1.78e+01
11	NV1	4.03	126	108	EHT	SH	-0.026	−		-1.31e+02	9.87e+00
12	NV10	5.05	97	104	EHU	P	0.047	−		-1.33e+01	1.86e+01
13	NV10	5.05	97	103	EHT	SH	0.054				
14	NV2	16.36	82	70	EHU	P	-0.155	+			
15	NV3	18.32	34	70	EHZ	P	-0.154	−			
16	NV4	7.28	49	98	EHU	P	0.049	+		1.11e+01	1.69e+01
17	NV4	7.28	49	97	EHT	SH	0.112	+		3.73e+01	1.37e+01
18	NV5	9.81	26	95	EHU	P	-0.052	−		-3.40e+00	2.32e+01
19	NV5	9.81	26	95	EHT	SH	-0.070	+		3.79e+01	1.41e+01

	Sta	Type	Penalty
1	CE2	P:SH	0.043
2	CE4	P:SH	
3	CE8	P:SH	0.049
4	NV1	P:SH	
5	NV4	P:SH	0.016
6	NV5	P:SH	0.028

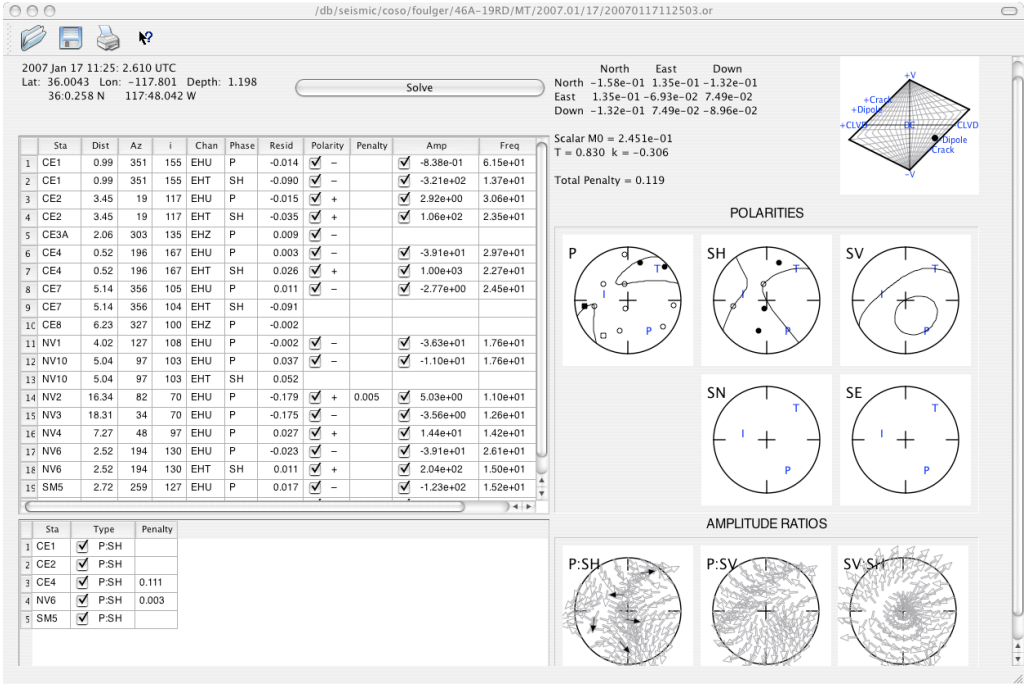

	Sta	Dist	Az	i	Chan	Phase	Resid	Polarity	Penalty	Amp	Freq
1	CE1	0.99	351	155	EHU	P	-0.014	−		-8.38e-01	6.15e+01
2	CE1	0.99	351	155	EHT	SH	-0.090	−		-3.21e+02	1.37e+01
3	CE2	3.45	19	117	EHU	P	-0.015	+		2.92e+00	3.06e+01
4	CE2	3.45	19	117	EHT	SH	-0.035	+		1.06e+02	2.35e+01
5	CE3A	2.06	303	135	EHZ	P	0.009	−			
6	CE4	0.52	196	167	EHU	P	0.003	−		-3.91e+01	2.97e+01
7	CE4	0.52	196	167	EHT	SH	0.026	+		1.00e+03	2.27e+01
8	CE7	5.14	356	105	EHU	P	0.011	−		-2.77e+00	2.45e+01
9	CE7	5.14	356	104	EHT	SH	-0.091				
10	CE8	6.23	327	100	EHZ	P	-0.002				
11	NV1	4.02	127	108	EHU	P	-0.002	−		-3.63e+01	1.76e+01
12	NV10	5.04	97	103	EHU	P	0.037	−		-1.10e+01	1.76e+01
13	NV10	5.04	97	103	EHT	SH	0.052				
14	NV2	16.34	82	70	EHU	P	-0.179	+	0.005	5.03e+00	1.10e+01
15	NV3	18.31	34	70	EHU	P	-0.175	−		-3.56e+00	1.26e+01
16	NV4	7.27	48	97	EHU	P	0.027	+		1.44e+01	1.42e+01
17	NV6	2.52	194	130	EHU	P	-0.023	−		-3.91e+01	2.61e+01
18	NV6	2.52	194	130	EHT	SH	0.011	+		2.04e+02	1.50e+01
19	SM5	2.72	259	127	EHU	P	0.017	−		-1.23e+02	1.52e+01

	Sta	Type	Penalty
1	CE1	P:SH	
2	CE2	P:SH	
3	CE4	P:SH	0.111
4	NV6	P:SH	0.003
5	SM5	P:SH	

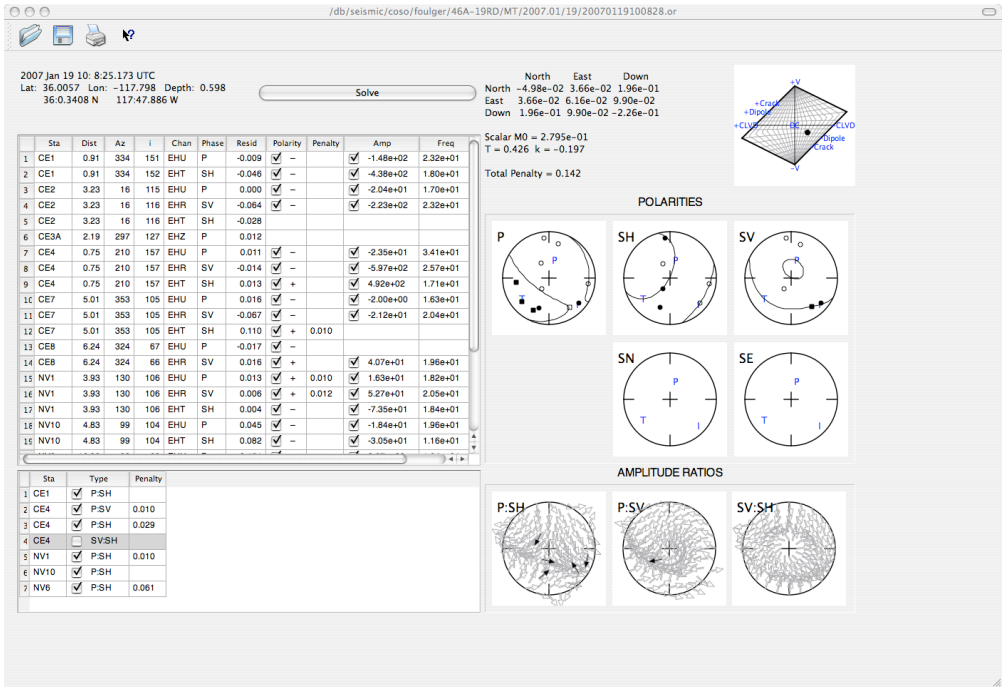

	Sta	Dist	Az	i	Chan	Phase	Resid	Polarity	Penalty	Amp	Freq
1	CE1	0.91	334	151	EHU	P	-0.009	–		-1.48e+02	2.32e+01
2	CE1	0.91	334	152	EHT	SH	-0.046	–		-4.38e+02	1.80e+01
3	CE2	3.23	16	115	EHU	P	0.000	–		-2.04e+01	1.70e+01
4	CE2	3.23	16	116	EHR	SV	-0.064	–		-2.23e+02	2.32e+01
5	CE2	3.23	16	116	EHT	SH	-0.028				
6	CE3A	2.19	297	127	EHZ	P	0.012				
7	CE4	0.75	210	157	EHU	P	0.011	–		-2.35e+01	3.41e+01
8	CE4	0.75	210	157	EHR	SV	-0.014	–		-5.97e+02	2.57e+01
9	CE4	0.75	210	157	EHT	SH	0.013	+		4.92e+02	1.71e+01
10	CE7	5.01	353	105	EHU	P	0.016	–		-2.00e+00	1.63e+01
11	CE7	5.01	353	105	EHR	SV	-0.067	–		-2.12e+01	2.04e+01
12	CE7	5.01	353	105	EHT	SH	0.110	+	0.010		
13	CE8	6.24	324	67	EHU	P	-0.017	–			
14	CE8	6.24	324	66	EHR	SV	0.016	+		4.07e+01	1.96e+01
15	NV1	3.93	130	106	EHU	P	0.013	+	0.010	1.63e+01	1.82e+01
16	NV1	3.93	130	106	EHR	SV	0.006	+	0.012	5.27e+01	2.05e+01
17	NV1	3.93	130	106	EHT	SH	0.004	–		-7.35e+01	1.84e+01
18	NV10	4.83	99	104	EHU	P	0.045	–		-1.84e+01	1.96e+01
19	NV10	4.83	99	104	EHT	SH	0.082	–		-3.05e+01	1.16e+01

	Sta	Type	Penalty
1	CE1	P:SH	
2	CE4	P:SV	0.010
3	CE4	P:SH	0.029
4	CE4	SV:SH	
5	NV1	P:SH	0.010
6	NV10	P:SH	
7	NV6	P:SH	0.061

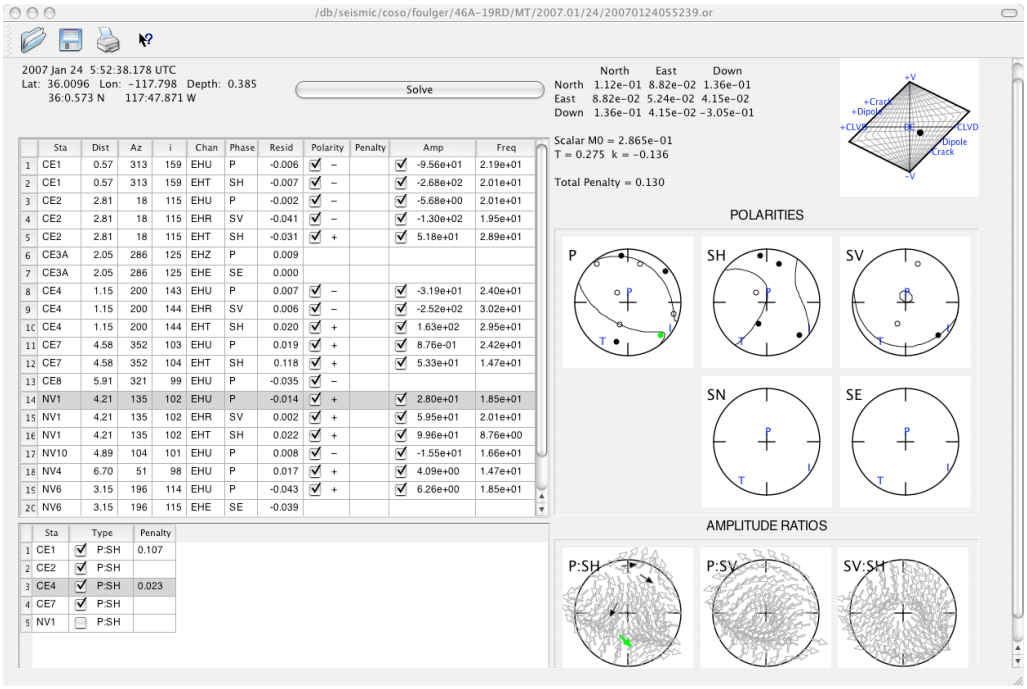

	Sta	Dist	Az	i	Chan	Phase	Resid	Polarity	Penalty	Amp	Freq
1	CE1	0.57	313	159	EHU	P	-0.006	–		-9.56e+01	2.19e+01
2	CE1	0.57	313	159	EHT	SH	-0.007	–		-2.68e+02	2.01e+01
3	CE2	2.81	18	115	EHU	P	-0.002	–		-5.68e+00	2.01e+01
4	CE2	2.81	18	115	EHR	SV	-0.041	–		-1.30e+02	1.95e+01
5	CE2	2.81	18	115	EHT	SH	-0.031	+		5.18e+01	2.89e+01
6	CE3A	2.05	286	125	EHZ	P	0.009				
7	CE3A	2.05	286	125	EHE	SE	0.000				
8	CE4	1.15	200	143	EHU	P	0.007	–		-3.19e+01	2.40e+01
9	CE4	1.15	200	144	EHR	SV	0.006	–		-2.52e+02	3.02e+01
10	CE4	1.15	200	144	EHT	SH	0.020	+		1.63e+02	2.95e+01
11	CE7	4.58	352	103	EHU	P	0.019	+		8.76e-01	2.42e+01
12	CE7	4.58	352	104	EHT	SH	0.118	+		5.33e+01	1.47e+01
13	CE8	5.91	321	99	EHU	P	-0.035	–			
14	NV1	4.21	135	102	EHU	P	-0.014	+		2.80e+01	1.85e+01
15	NV1	4.21	135	102	EHR	SV	0.002	+		5.95e+01	2.01e+01
16	NV1	4.21	135	102	EHT	SH	0.022	+		9.96e+01	8.76e+00
17	NV10	4.89	104	101	EHU	P	0.008	–		-1.55e+01	1.66e+01
18	NV4	6.70	51	98	EHU	P	0.017	+		4.09e+00	1.47e+01
19	NV6	3.15	196	114	EHU	P	-0.043	+		6.26e+00	1.85e+01
20	NV6	3.15	196	115	EHE	SE	-0.039				

	Sta	Type	Penalty
1	CE1	P:SH	0.107
2	CE2	P:SH	
3	CE4	P:SH	0.023
4	CE7	P:SH	
5	NV1	P:SH	

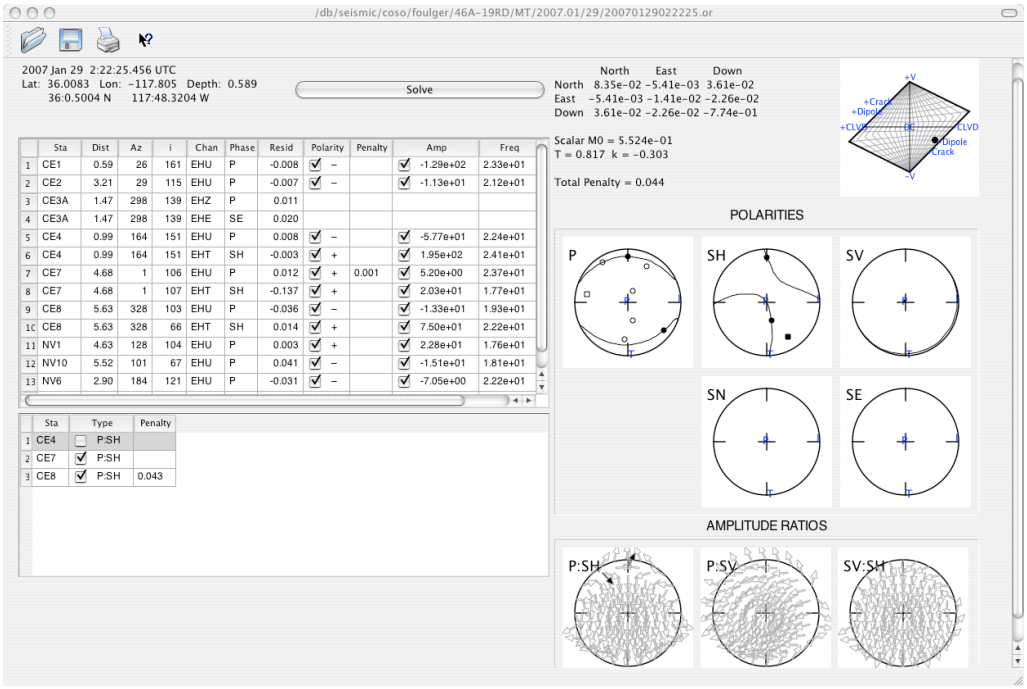

	Sta	Dist	Az	i	Chan	Phase	Resid	Polarity	Penalty	Amp	Freq
1	CE1	0.59	26	161	EHU	P	-0.008	–		-1.29e+02	2.33e+01
2	CE2	3.21	29	115	EHU	P	-0.007	–		-1.13e+01	2.12e+01
3	CE3A	1.47	298	139	EHZ	P	0.011				
4	CE3A	1.47	298	139	EHE	SE	0.020				
5	CE4	0.99	164	151	EHU	P	0.008	–		-5.77e+01	2.24e+01
6	CE4	0.99	164	151	EHT	SH	-0.003	+		1.95e+02	2.41e+01
7	CE7	4.68	1	106	EHU	P	0.012	+	0.001	5.20e+00	2.37e+01
8	CE7	4.68	1	107	EHT	SH	-0.137	+		2.03e+01	1.77e+01
9	CE8	5.63	328	103	EHU	P	-0.036	–		-1.33e+01	1.93e+01
10	CE8	5.63	328	66	EHT	SH	0.014	+		7.50e+01	2.22e+01
11	NV1	4.63	128	104	EHU	P	0.003	+		2.28e+01	1.76e+01
12	NV10	5.52	101	67	EHU	P	0.041	–		-1.51e+01	1.81e+01
13	NV6	2.90	184	121	EHU	P	-0.031	–		-7.05e+00	2.22e+01

	Sta	Type	Penalty
1	CE4	P:SH	
2	CE7	P:SH	
3	CE8	P:SH	0.043

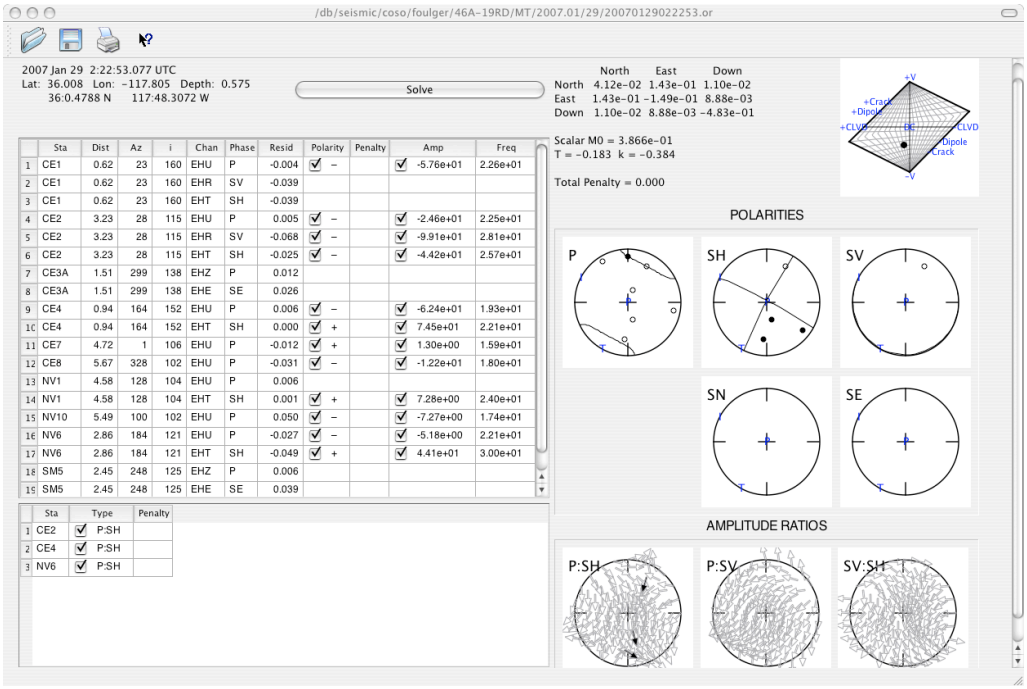

	Sta	Dist	Az	i	Chan	Phase	Resid	Polarity	Penalty	Amp	Freq
1	CE1	0.62	23	160	EHU	P	-0.004	–		-5.76e+01	2.26e+01
2	CE1	0.62	23	160	EHR	SV	-0.039				
3	CE1	0.62	23	160	EHT	SH	-0.039				
4	CE2	3.23	28	115	EHU	P	0.005	–		-2.46e+01	2.25e+01
5	CE2	3.23	28	115	EHR	SV	-0.068	–		-9.91e+01	2.81e+01
6	CE2	3.23	28	115	EHT	SH	-0.025	–		-4.42e+01	2.57e+01
7	CE3A	1.51	299	138	EHZ	P	0.012				
8	CE3A	1.51	299	138	EHE	SE	0.026				
9	CE4	0.94	164	152	EHU	P	0.006	–		-6.24e+01	1.93e+01
10	CE4	0.94	164	152	EHT	SH	0.000	+		7.45e+01	2.21e+01
11	CE7	4.72	1	106	EHU	P	-0.012	+		1.30e+00	1.59e+01
12	CE8	5.67	328	102	EHU	P	-0.031	–		-1.22e+01	1.80e+01
13	NV1	4.58	128	104	EHU	P	0.006				
14	NV1	4.58	128	104	EHT	SH	0.001	+		7.28e+00	2.40e+01
15	NV10	5.49	100	102	EHU	P	0.050	–		-7.27e+00	1.74e+01
16	NV6	2.86	184	121	EHU	P	-0.027	–		-5.18e+00	2.21e+01
17	NV6	2.86	184	121	EHT	SH	-0.049	+		4.41e+01	3.00e+01
18	SM5	2.45	248	125	EHZ	P	0.006				
19	SM5	2.45	248	125	EHE	SE	0.039				

	Sta	Type	Penalty
1	CE2	P:SH	
2	CE4	P:SH	
3	NV6	P:SH	

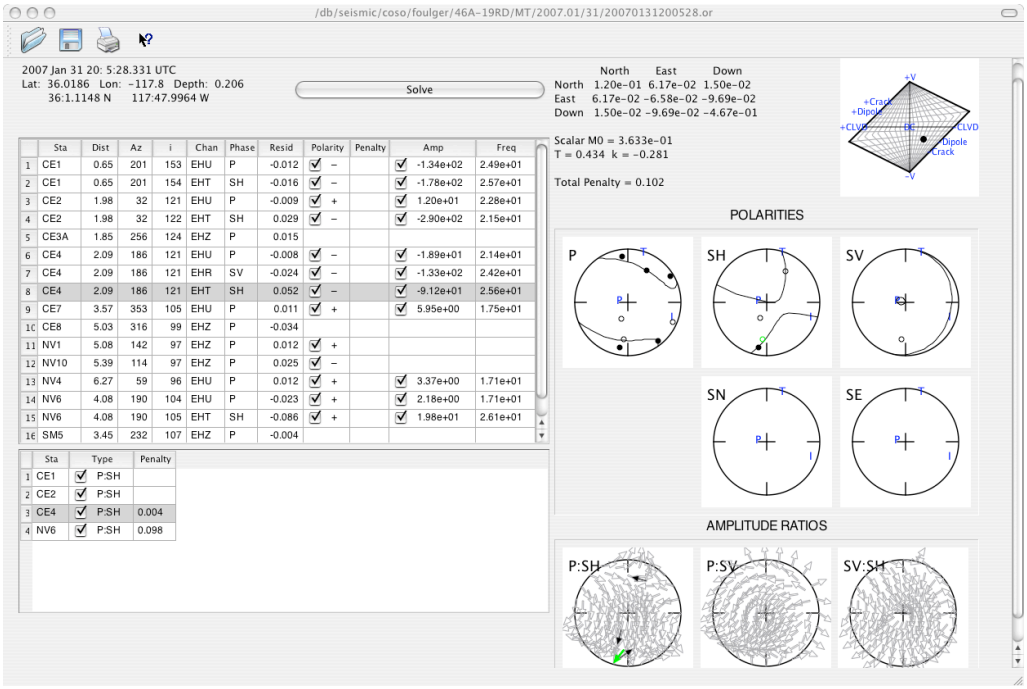
/db/seismic/coso/foulger/46A-19RD/MT/2007.01/31/20070131200528.or
2007 Jan 31 20: 5:28.331 UTC
Lat: 36.0186 Lon: -117.8 Depth: 0.206
36:1.1148 N 117:47.9964 W
Solve
North East Down
North 1.20e-01 6.17e-02 1.50e-02
East 6.17e-02 -6.58e-02 -9.69e-02
Down 1.50e-02 -9.69e-02 -4.67e-01
Scalar M0 = 3.633e-01
T = 0.434 k = -0.281
Total Penalty = 0.102
+V
+Crack
+Dipole
+CLVD
DC
CLVD
-Dipole
-Crack
-V
Sta Dist Az i Chan Phase Resid Polarity Penalty Amp Freq
1 CE1 0.65 201 153 EHU P -0.012 – -1.34e+02 2.49e+01
2 CE1 0.65 201 154 EHT SH -0.016 – -1.78e+02 2.57e+01
3 CE2 1.98 32 121 EHU P -0.009 + 1.20e+01 2.28e+01
4 CE2 1.98 32 122 EHT SH 0.029 – -2.90e+02 2.15e+01
5 CE3A 1.85 256 124 EHZ P 0.015
6 CE4 2.09 186 121 EHU P -0.008 – -1.89e+01 2.14e+01
7 CE4 2.09 186 121 EHR SV -0.024 – -1.33e+02 2.42e+01
8 CE4 2.09 186 121 EHT SH 0.052 – -9.12e+01 2.56e+01
9 CE7 3.57 353 105 EHU P 0.011 + 5.95e+00 1.75e+01
10 CE8 5.03 316 99 EHZ P -0.034
11 NV1 5.08 142 97 EHZ P 0.012 + –
12 NV10 5.39 114 97 EHZ P 0.025 – –
13 NV4 6.27 59 96 EHU P 0.012 + 3.37e+00 1.71e+01
14 NV6 4.08 190 104 EHU P -0.023 + 2.18e+00 1.71e+01
15 NV6 4.08 190 105 EHT SH -0.086 + 1.98e+01 2.61e+01
16 SM5 3.45 232 107 EHZ P -0.004
Sta Type Penalty
1 CE1 P:SH
2 CE2 P:SH
3 CE4 P:SH 0.004
4 NV6 P:SH 0.098
POLARITIES
P
SH
SV
SN
SE
AMPLITUDE RATIOS
P:SH
P:SV
SV:SH